The Measurement of the TL' Asymmetry in π^0 Electroproduction Near Threshold

Mitra H. Shabestari
Charlottesville, Virginia

M.S. Physics, University of Toledo, 2002
B.S. Physics, University of Tehran, 1995

A Dissertation presented to the Graduate Faculty of the University of Virginia in Candidacy for the Degree of Doctor of Philosophy

Department of Physics

University of Virginia
December 2010

_____

_____

_____

_____

Abstract

The experimental data on π^0 electroproduction over the past few years have indicated troublesome discrepancies with the predictions of chiral perturbation theory. The differences have been observed in low Q^2 and near threshold (low ΔW) for unpolarized cross section $\sigma_0 = \sigma_T + \epsilon_L \sigma_L$ and asymmetry $A_{TL'}$. That is, while phenomenological models show better agreement with σ_0 data in this region, the inconsistency of chiral perturbation theory with experimental data in this region is particularly serious. The failure seems to come from a combination of multipoles that is already fixed by π^0 photoproduction, so that, it cannot be varied. The current experimental data, however, are not spanned over a fine grid of Q^2 and ΔW and have somewhat large statistical and systematic errors. To confirm or refute these discrepancies, experiment E04-007 at Hall A of Jefferson Lab was intended to provide data on π^0 electroproduction, $H\left(e, e'p\right)\pi^0$, that extend the data in Q^2 and ΔW. The use of Hall A BigBite spectrometer, with its large solid angle and momentum acceptance, allows the collection of data with higher precision. Systematic error is minimized since the BigBite spectrometer can measure the entire proton's angular distribution within three kinematic settings.

The data were collected in near threshold: the region that is specified by $0.056\ (\mathrm{GeV}/c)^2 \leqslant Q^2 \leqslant 0.45\ (\mathrm{GeV}/c)^2$, and $0\ \mathrm{MeV} \leqslant \Delta W \leqslant 45\ \mathrm{MeV}$. Polarized electrons at energies of 1193 MeV and 2322 MeV were scattered off a cryogenic hydrogen target. The pion was identified by detecting the scattered electron in the left high-resolution spectrometer in coincidence with the recoiled proton, detected in BigBite spectrometer. In this work, the data on TL' asymmetry function is presented.

To my husband and best friend, ***Mehrdad.***

Acknowledgements

There are many people who have provided me valuable advice and assistance during the course of this long journey.

First, I would like to express gratitude to my thesis advisor, Nilanga Liyanage for his guidance and support throughout my graduate study.

I would like to thank my committee members Donald Crabb, Douglas Higinbotham, and Simonetta Liuti for taking time out of their busy schedule to serve on my committee. A special thank you to Douglas Higinbotham, my supervisor at Jefferson Lab for his support, encouragement, and valuable advices.

My especial thanks to Brad Sawatzky for his confidence in my work and continued encouragement and support. Brad was always extremely generous with his time and I appreciate the many discussions and conversations we had.

I would like to thank the fellow graduate students Ray Chan and Brandon Craver for their help with construction of multi wire drift chambers, Khem Chirapatpimol and Miha Mihovilovic for their help on data analysis. I am thankful to Vladimir Nelyubin for his advice and help during the construction of multi wire drift chambers.

Appreciations also go to John R. Annand, Richard Lidgren, Bryan Moffit, Simon Širca, Nikos Sparveris, and Vince Sulkosky for helpful discussions.

I would like to thank Cole Smith for providing the theoretical values. I am also thankful to Oscar Rondon for always being willing to offer his help. Thanks also go to Lothar Tiator for helpful discussions on MAID model.

I extend a note of gratitude to Hall A scientific, engineering and technical staff, and everyone who offered their assistance by taking shifts during E04-007 experiment. This experiment would not have been successful without their hard work and dedication.

Thanks go to staffs in physics department at UVA, especially Vicky Ingram. Besides her kindness, Vicky was always willing to help whenever I needed the library and its services.

Finally, my utmost appreciation goes to my husband Mehrdad for challenging me, by his own example, to keep growing, learning and pushing myself. No words can express the love I have for him, nor the gratitude I feel for all he has done over these years. All I can say is that without Mehrdad's love and support, I would have never made it this far.

Contents

Introduction

Over the past several years, experimental data on π^0 electroproduction have shown disagreements with the predictions of Chiral Perturbation Theory (ChPT). The origin of these differences, which occur at low four-momentum transfer squared Q^2 and near the π^0 threshold, can potentially be problematic for ChPT. The extent of these problems could go as far as the symmetries of Quantum Chromodynamics (QCD).

As the fundamental theory of strong interaction, QCD has proven itself in many areas. The most notable is its integration with other gauge theories of weak and electromagnetic forces into a renormalizable theory, what we know as the Standard Model. The application of QCD to low energy events, however, is not without difficulty. The low-energy QCD is one of the two phases of the theory where conventional perturbation expansion in coupling constant and diagrammatic approach is inapplicable, due to the large value of the coupling constant at large distances.

As ordinary hadrons are made of light quarks, a light-quark QCD can be considered in isolation. Such a theory, in the massless limit, exhibits a global symmetry called chiral symmetry. The spontaneous breaking of chiral symmetry yields massive Nambu-Goldstone bosons which are assumed to be pseudoscalar mesons: pions, eta, kaons. These Nambu-Goldstone bosons, unlike those in electroweak theory, cannot be absorbed by gauge fields and therefore they remain in the Lagrangian. Treating the quark masses as perturbation and including baryonic fields into the theory provide a powerful tool to study the strong interaction at low energy. In this form, ChPT can describe the meson-baryon interactions in terms of expansions around the masses of quarks and another small parameter q (normally an external momentum, or a mass scale). Data on pion production due to an external field or pion scatterings off nucleons can test the very fundaments of ChPT, since they are the Nambu-Goldstone bosons of chiral symmetry breaking.

Electroproduction of π^0 particularly provides a good test on ChPT. This is due to the fact

that the phase of a certain amplitude of π^0 production involves the masses of up and down quarks and therefore becomes explicitly sensitive to chiral symmetry breaking. To effectively test ChPT, the measurements ought to be made where Q^2 and ΔW (the deviation from threshold energy) are small, so that the factors administering the ChPT expansions are small.

On a less fundamental level, near threshold is also appealing since it is dominated by the so-called "non-resonant" part of the pion production. As we get away from threshold, a "resonant part" stemming from nucleon's internal excitations followed by decays into nucleon and pion will dominate the pion production process.

The experimental data at low Q^2 and near threshold region, however, shows discrepancies with ChPT predictions in cross section and asymmetry function, $A_{TL'}$, along the ΔW axis [1]. If these differences, which are inconsistent with the predictions of other phenomenological models, are not resolved the viability of ChPT as a calculable low-energy segment of QCD can be in question.

Unfortunately, the body of experimental data on near threshold π^0 electroproduction is coarse in both Q^2 and ΔW variables. Additionally, there are serious discrepancies amongst old and new experimental data sets when it comes to some amplitudes of π^0 electroproduction. Recent measurements also bear relatively large statistical and systematic errors. New measurements of cross sections and asymmetry function with high statistical precision and small systematic error bars that can extend the data at the same time seem necessary to effectively test the ChPT and resolve the aforementioned discrepancies.

The experiment E04-007 at Hall A of Thomas Jefferson National Accelerator Facility (Jefferson Lab) is intended to take on this task. The experiment provides high precision data at additional low Q^2 and ΔW values, which puts the existing experimental data on a finer grid of Q^2 and ΔW. The use of polarized beam and unpolarized target allows asymmetry measurements, which extends the current $A_{TL'}$ data and raises the precision at the same time.

In this thesis, we provide asymmetry values for π^0 electroproduction measured by experiment E04-007 and compare the results to those of ChPT, and other phenomenological models.

[1] We will discuss all these discrepancies in section 1.2, but if you cannot wait see Fig. 1.7 for the time being.

Chapter 1

The Physics of Neutral Pion Electroproduction

Historically, pions were postulated by Yukawa [1], as massive mediators, to explain the short-range nature of the nuclear forces. A few years later, Kemmer [2] formulated a theory of strong interactions according to isospin SU(2) invariance. In this model, pions were elements of an isospin triplet, i.e., $\left(\pi^+, \pi^0, \pi^-\right)$, which mediated the strong interaction within the isospin doublet (p, n)[1]. Even though the theoretical prediction of pions were in 1930's, pions as "the carriers of nuclear forces" were identified experimentally in late 1940's: charged pions by Lattes et al. [3] and the neutral pion by Panofsky et al. [4]. The classification of hadrons in non-relativistic quark model [5–7] shed more light on the place of pions amongst the strongly interacting particles. In this picture, one distinguishes *baryons* (baryon number $B = \pm 1$), which are fermions and carry spin 1/2, 3/2, and *mesons* (baryon number $B = 0$), which have integer spin. The lightest hadrons, with equal spin and equal parity, can be arranged in simple multiplets, where two further quantum numbers (i.e., other than baryon number) serve as order criteria: the isospin I and its third component I_3 , and the strangeness S or alternatively the so-called strong hypercharge $Y = B + S$. These quantum numbers are characterized by the fact that they are exactly conserved under strong interaction[2]. Of these hadron multiplets, pions are amongst *pseudoscalar mesons* with spin zero and odd parity. Since they posses odd parity they are not scalars but pseudoscalars, implying that their wavefunctions change sign

[1] That is, in spirit, similar to W bosons of weak interactions (charged and neutral) except that pions in this paradigm were not gauge fields.

[2] Conservation of strangeness is broken by weak interactions, which leads to decays.

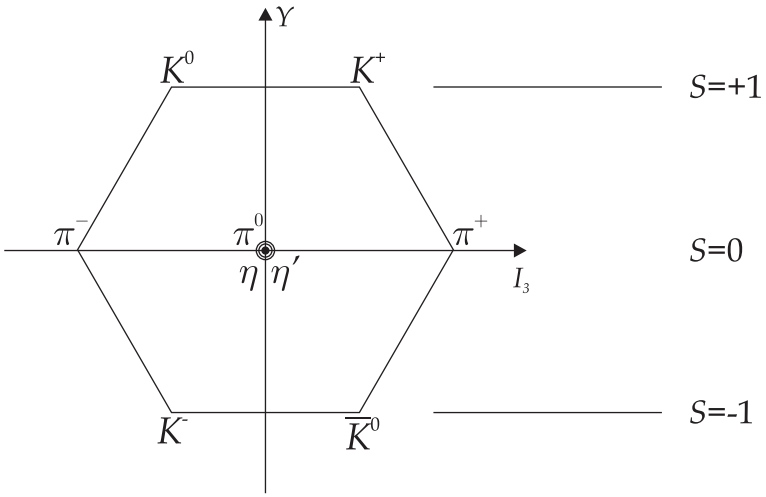

Figure 1.1: Psuedoscalar mesons nonet in non-relativistic quark model.

under space inversion $\mathbf{x} \to -\mathbf{x}$. Since they have no spin, their magnetic moments vanish ($\mu = 0$). The pseudoscalar mesons in non-relativistic quark model (i.e., an SU(3) flavor model) are comprised of a quark and an antiquark, leading to $[3] \otimes [\bar{3}] = [8] \oplus [1]$. Such a pseudoscalar *nonet* can be put in geometrical representation of Fig. 1.1, where η' is the singlet of the nonet $[8] \oplus [1]$.

The pions, as seen in Fig. 1.1, form a triplet in isospin space $I_3 = 0, \pm 1$, with no strangeness or hypercharge. Basic properties of pions are listed in table 1.1, of which some are exclusively known from experiment [8].

Clearly, all pion masses (energies) are nearly equal. In analogy to the mass difference between proton and neutron, this near-equality may be interpreted as meaning that the strong interaction (which determines the dominant part of the mass) is invariant in isospin space, and that the small mass difference of a few MeVs is caused by electromagnetic or other interactions [3].

On the other hand, the spatial extension of pions is an important indicator of its internal structure. Pion's form factor follows a simple monopole form of [9]

$$F_\pi = \left(1 + b^2 Q^2\right)^{-1},$$

which can be used to calculate the root mean square radius of pions (b is imperical parameter). For small momentum transfers, pion's charge radius [10] is curiously close to that of proton [11,

[3] In fact, it can be shown that the Coulomb energy of a homogeneously charged sphere with radius of pion's Compton wave length is of order of the mass difference between charged and neutral pions, i.e., ~ 5 Mev.

Table 1.1: A summary of basic properties of pions.

	I	I_3	Mass (Mev)	Lifetime (s)	Main decay mode	Main decay (%)
π^+	1	+1	139.57	2.6×10^{-8}	$\mu^+ \nu_\mu$	99.98
π^0	1	0	134.97	8.4×10^{-17}	$\gamma\gamma$	98.79
π^-	1	-1	139.57	2.6×10^{-8}	$\mu^- \bar{\nu}_\mu$	99.98

12], i.e.,

$$R_p = \sqrt{\langle r^2 \rangle_p} = 0.895 \pm 0.018 \text{ fm},$$

$$R_\pi = \sqrt{\langle r^2 \rangle_\pi} = 0.657 \pm 0.012 \text{ fm},$$

which makes point-like particle approximation a very rough one for pions.

Despite the success of non-relativistic quark model in classifying hadrons (pions for our case), no further fundamental insight on pions or psuedosacalr mesons per se can be obtained from the model alone, e.g., connections to other symmetries, internal structure, ... Quantum Chromodynamics which is used to explain the strong force, phenomenological models, and experimental investigations of deep inelastic scattering involving pions are the current tools to gain deeper understanding of the underlying physics.

For example, within chiral QCD, which is at most a three-flavor (or three-quark) theory of strong interactions, the psuedoscalar octet (i.e., the aforementioned nonet minus η') are assumed to be the Nambu-Goldstone bosons arising from the spontaneous breaking of its chiral symmetry (which does not exist, and therefore broken). This is different from the non-relativistic quark model in the sense that we now link the existence of pions to the spontaneous QCD chiral symmetry breaking. In the perturbative arrangement of this framework (ChPT), one can predict values for certain hadronic functions which can be measured, leading to the possibility that the validity of such a hypothesis may be tested.

We leave these subjects to the upcoming sections of this chapter, where we go over the theoretical formalism of carrying out π^0 electroproduction calculations in the threshold region and the relevant experimental works.

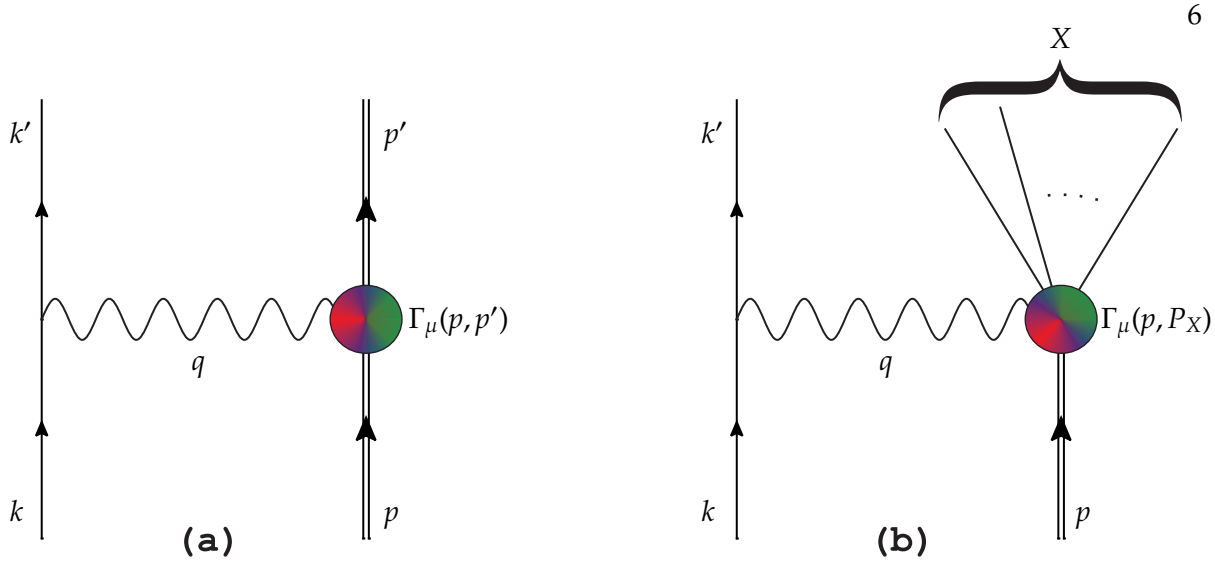

Figure 1.2: Elastic (a) and inelastic (b) electron-proton scattering diagrams to the leading order.

1.1 Theoretical Ground and Methods

The theoretical formalism for pion electroproduction, similar to any inelastic scattering process, is rather lengthy and packed with cumbersome algebraic derivations. The method and concept, however, are not. Since one can safely disregard the Z^0 boson exchange contribution at low energies, for the theoretical treatment of the reaction one can employ (at least to arrive at the cross section formula) the same fundamental methods applied to a generic lepton-nucleon inelastic scattering through the exchange of a photon. For that reason and to put the emphasis on the concept rather than derivations, we shall briefly discuss the scattering of an electron off a nucleon. We will, therefore, be able to understand the underlying theoretical approach to the π^0 electroproduction problem, even if we omit the laborious parts.

1.1.1 Preliminaries: Electron-Proton Scattering

The electron-proton scattering, with leading order diagram of Fig. 1.2(a) for elastic scattering, is often discussed in text books (e.g., Refs. [13, 14]) in detail, leading to Rosenbluth formula. Therefore, we will emphasize the method and only shortly repeat the discussion.

The scattering of highly energetic electrons off nucleons is to learn about the internal structure of nucleons [4]. For our problem, once the proton is assumed not to be a point particle,

[4] To have a comprehensive image of the internal structure of nucleons, the data from neutrino-nucleon scattering must be considered as well. That is because electrons mainly interact through photon exchange, probing the electromagnetic charge distribution, while neutrinos react through weak interactions and sense the nucleon's distribution of "weak charges."

the internal structure of it is taken into account by a generalized vertex function $-ie_p\Gamma_\mu$ instead of the point-like-particle QED vertex $-ie_p\gamma_\mu$. The determination of this generalized vertex is through considering the symmetries of the theory, the particles involved and the kinematical variables of the process of interest. Since QED is Lorentz-covariant, the vertex function Γ_μ (or more precisely the matrix elements of the hadronic current $\sim \bar{u}\Gamma_\mu u$) must be a Lorentz vector (a four-vector). The most general structure of Γ_μ for electron-proton scattering [5] is thus

$$\Gamma_\mu = A\left(q^2\right)\gamma_\mu + B\left(q^2\right)p'_\mu + C\left(q^2\right)p_\mu + iD\left(q^2\right)p'^\nu\sigma_{\mu\nu} + iE\left(q^2\right)p^\nu\sigma_{\mu\nu}, \tag{1.1}$$

where $A\left(q^2\right)$, $B\left(q^2\right)$, ..., $E\left(q^2\right)$ are undetermined Lorentz invariant quantities of variable q^2 and $\sigma_{\mu\nu} = i/2\left[\gamma_\mu, \gamma_\nu\right]_-$ is the bi-spinor representation of the generators of Lorentz algebra. The reason undetermined coefficients A, B, ... are functions of q^2 is that they ought to depend on a scalar made out of the hadronic kinematical variables. Any scalar made in this fashion, such as $p \cdot p'$, $p \cdot p$, $p \cdot q$, etc., can be expressed in terms of q^2 and M^2 (M is the mass of proton), so the only real variable is q^2. Since QED is gauge invariant [6], the hadronic transition current $J^\mu = \bar{u}^{s'}\left(p'\right)\Gamma^\mu u^s\left(p\right)$ is conserved, i.e., $\partial_\mu J^\mu = 0$ or in momentum space $q_\mu J^\mu = 0$. This leads to $C = B$ and $D = -E$. On the other hand, the transition current ought to be Hermitian, which makes all coefficients real. At last, due to Gordon decomposition

$$\bar{u}\gamma_\mu u = \frac{1}{2M}\left(p_\mu + p'_\mu\right)\bar{u}u + \frac{i}{2M}q^\nu\bar{u}\sigma_{\mu\nu}u,$$

the terms proportional to p_μ and p'_μ can be expressed in terms of γ_μ and $\sigma_{\mu\nu}$, which leads to a current in the form

$$\bar{u}^{s'}\left(p'\right)\Gamma^\mu u^s\left(p\right) = \bar{u}^{s'}\left(p'\right)\left(F_1\left(q^2\right)\gamma_\mu + \frac{i}{2M}F_2\left(q^2\right)q^\nu\sigma_{\mu\nu}\right)u^s\left(p\right), \tag{1.2}$$

where F_1 and F_2 are "form factors." The absolute square of this expression enters in the cross section in the form of hadronic tensor $W_{\mu\nu}$; because the unpolarized averaged squared amplitude of the process to leading order reads

$$\overline{|\mathcal{M}|^2} = \frac{e^2e_p^2}{\left(q^2\right)^2}L^{\mu\nu}W_{\mu\nu}, \tag{1.3}$$

where

$$\begin{aligned} L^{\mu\nu} &= \frac{1}{2}tr\left[\gamma^\mu\left(k+m\right)\gamma^\nu\left(k'+m\right)\right], \\ &= 2\left(k^\mu k'^\nu + k^\nu k'^\mu - \eta^{\mu\nu}k\cdot k' + \eta^{\mu\nu}m^2\right), \end{aligned} \tag{1.4}$$

[5] Note that for neutrino-proton scattering this form for Γ_μ is not correct, due to parity violation of weak interactions.

[6] That is to say it is invariant under symmetry transformations of electromagnetism group $\mathrm{U}(1)_{EM}$ and therefore has a conserved current according to Noether theorem.

is the leptonic tensor (here for electron with mass m), and

$$W_{\mu\nu} = \frac{1}{2}\sum_{\text{spins}}\left[\bar{u}^{s'}\left(p'\right)\Gamma^{\mu}u^{s}\left(p\right)\right]^{*}\left[\bar{u}^{s'}\left(p'\right)\Gamma^{\mu}u^{s}\left(p\right)\right], \tag{1.5}$$

is, as promised, the hadronic tensor, involving the squared of the hadronic transition current. The hadronic tensor is the quantity of interest in a typical electron-proton scattering, either elastic or inelastic, and the starting point for the theoretical treatment of the π^0 electroproduction problem. Of course, the evaluation of $W_{\mu\nu}$, which involves trace techniques, depends on the complexity of Γ_{μ} and whether the process is elastic or inelastic. For example, for elastic scattering

$$W_{\mu\nu}^{\text{el.}} = \left(-\eta_{\mu\nu} + \frac{q_{\mu}q_{\nu}}{q^2}\right)W_1\left(Q^2\right) + \left(p_{\mu} - q_{\mu}\frac{p\cdot q}{q^2}\right)\left(p_{\nu} - q_{\nu}\frac{p\cdot q}{q^2}\right)\frac{W_2\left(Q^2\right)}{M^2},$$

where $Q^2 = -q^2$ and $W_{1,2}$ are expressed in terms of F_1 and F_2. In case of an *inclusive* inelastic scattering, Fig. 1.2(b), a simple expression for $W_{\mu\nu}$ can be obtained, because we can sum over all possible final hadronic states. We get

$$W_{\mu\nu}^{\text{incl.}} = \left(-\eta_{\mu\nu} + \frac{q_{\mu}q_{\nu}}{q^2}\right)W_1\left(Q^2,\nu\right) + \left(p_{\mu} - q_{\mu}\frac{p\cdot q}{q^2}\right)\left(p_{\nu} - q_{\nu}\frac{p\cdot q}{q^2}\right)\frac{W_2\left(Q^2,\nu\right)}{M^2},$$

with the new parameter inelasticity $\nu = p\cdot q/M$, also the Ws are now called *structure functions*. The inelasticity parameter is a continuous parameter and should not be confused with the discrete Lorentz index ν in the above equation. The differential cross section in the lab frame is then given by (neglecting electron mass)

$$\frac{d^2\sigma}{dE'd\Omega} = \frac{\alpha^2 E'}{EQ^4}L^{\mu\nu}W_{\mu\nu},$$

where E and E' are the electron energies before and after the scattering, respectively. The above cross section obviously depends on the structure functions $W_1\left(Q^2,\nu\right)$ and $W_2\left(Q^2,\nu\right)$, which can be measured experimentally for definite electron energies E, E' and scattering angle θ if one sums the total reaction cross section for each (θ, E') bin. However the importance of structure functions is that they can be calculated from the microscopic properties of the quark model, which in turn involves quark interactions (i.e., QCD) and that in conjunction with experimental observations will provide a test for QCD predictions. We will encounter structure functions in π^0 electroproduction calculations as well. That is where ChPT will come into play and that is where it can indeed be tested just like the above case.

Up to now we have gone over the standard framework of studying a typical electron-proton scattering, which will be followed, in principle, for our problem. One piece of machinery that we have not provided is a technique suitable to evaluate the hadronic tensor $W_{\mu\nu}$ for our case. The $W_{\mu\nu}$ expression in Eq. 1.5 can be generalized to an inelastic scattering where the final hadron state is a multi-particle state, X (see Fig. 1.2(b)). In that case the hadronic current matrix elements (which in momentum space used to be $J^{\mu} = \bar{u}^{s'}(p')\,\Gamma^{\mu}u^{s}(p)$) between the initial nucleon state with momentum p_{μ} and an arbitrary hadronic final state X with total momentum $P_{X,\mu}$ is

$$\langle X(P_X)|\,\hat{J}_{\mu}(x)\,\big|N(p)\rangle = \langle X(P_X)|\,\hat{J}_{\mu}(0)\,\big|N(p)\rangle\, e^{-i(p-P_X)\cdot x},$$

The hadronic tensor comes about as a result of squaring, summing and averaging over initial and final degrees of freedom when one calculates $\overline{|\mathcal{M}|^2}$. That means the generalized hadronic tensor for an inclusive process in momentum space will be

$$\begin{aligned} W_{\mu\nu} &= \frac{1}{2}\sum_{\text{spins}}\sum_{X}\langle X(P_X)|\,\hat{J}_{\mu}(0)\,\big|N(p)\rangle^{*}\,\langle X(P_X)|\,\hat{J}_{\nu}(0)\,\big|N(p)\rangle \\ &= \frac{1}{2}\sum_{\text{spins}}\sum_{X}\langle N(p)\big|\,\hat{J}_{\mu}(0)\,|X(P_X)\rangle\,\langle X(P_X)|\,\hat{J}_{\nu}(0)\,\big|N(p)\rangle, \end{aligned} \tag{1.6}$$

where the sum over all X states is due to inclusiveness of the calculation. In that sense, since we are summing over all possible final hadronic states we have

$$\sum_{X}|X(P_X)\rangle\,\langle X(P_X)| = 1,$$

which yields

$$W_{\mu\nu} = \frac{1}{2}\sum_{\text{spins}}\langle N(p)\big|\,\hat{J}_{\mu}(0)\,\hat{J}_{\nu}(0)\,\big|N(p)\rangle\,. \tag{1.7}$$

The threshold π^0 electroproduction can, in principle, be considered as an inclusive process since the only possible final state is that with a proton and a π^0. Now that we know the general roadmap (i.e., how to calculate the hadronic transition current, tensor etc.) we can discuss the QED procedure for the differential cross section for the π^0 electroproduction reaction.

1.1.2 Neutral Pion Electroproduction: The QED Formalism

The first work on the theory of pion photoproduction (which later in literature normally included both virtual and real photons) was due to Kroll and Ruderman [15] who demanded gauge and Lorentz invariance and obtained model independent predictions for threshold

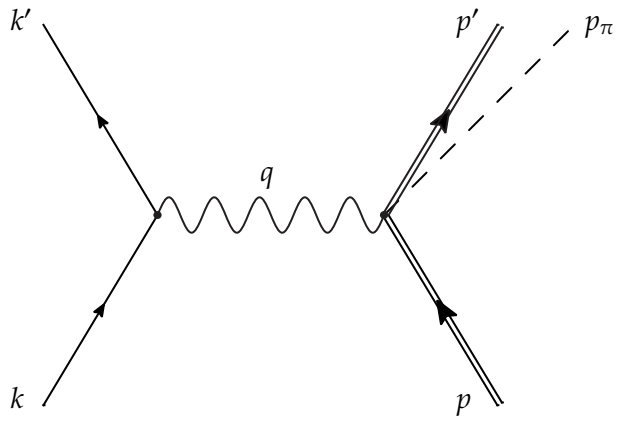

Figure 1.3: The leading order diagram of π^0 electroproduction process.

region, the so-called low-energy theorems (LET). Later, Chew et al. [16] obtained cross section through a similar formalism of the previous section where the hadronic current was expressed in terms of amplitudes which later on were referred to in texts as "CGLN amplitudes" (acronym after the authors). The CGLN amplitudes, denoted by F_i, depend on angle and energy (As structure functions Ws did in previous section), and are typically expanded in terms of the derivatives of Legendre polynomials, the so-called *multipole decomposition*. The coefficients of those expansions are the main quantities of interest, both experimentally and theoretically.

The LETs have been extended to electroproduction [17–21] to compute the amplitude, specially at threshold. A typical LET is an ab intio calculation of S matrix, which yields the invariant amplitude $\mathcal{M}$ of the pion production at low energy limit, considering partially-conserved-axial-current (PCAC) hypothesis to describe the pion field, and gauge invariance of electromagnetism. These theorems are exact for photo-production, but they are applied to electroproduction through expansion about massless pions: a power series in $\mu = m_\pi/M$. The LETs can provide the multipoles of CGLN amplitude for near threshold region up to a desired power of μ.

To begin with, we note that the π^0 electroproduction cross section can be computed with about 1% accuracy through the one-photon exchange diagram of Fig. 1.3. Let us first go through the kinematical variables necessary to describe the problem.

The four-momentum transfer of the virtual photon $q = k - k'$ is fixed by the four-momenta of the incoming, k, and outgoing, k', electrons. As usual, $Q^2 = -q^2$ is the positive quantity used to describe structure functions. Due to Energy-momentum conservation, there are three

independent four-momenta at the hadronic vertex, i.e., p, p_π, and q. Since the final hadrons are on-shell particles, i.e., $p^2 = M^2$, $p_\pi^2 = m_\pi^2$, one can form three independent scalars out of these momenta. They can be chosen to be (i) Q^2, (ii) the total momentum-energy squared of proton-pion system $W^2 = (p+q)^2 = (p'+p_\pi)^2$, and (iii) one of the two scalars $(q-p_\pi)^2$, $(p-p_\pi)^2$. Other kinematical quantities which can be of use are

$$q_{0,\text{Lab}}^{\text{Thr.}} = \frac{W_0^2 - M^2 + Q^2}{2M}, \tag{1.8a}$$

$$E_\pi = \frac{W^2 - M^2 + m_\pi^2}{2W}, \tag{1.8b}$$

$$\Delta W = W - W_0, \tag{1.8c}$$

where $q_{0,\text{Lab}}^{\text{Thr.}}$ is the virtual photon energy in lab frame at threshold, E_π is pion's energy in pion-nucleon CM frame [7], and ΔW measures the deviation from the threshold value $W_0 = M + m_\pi$. Following the previous section's discussion, we need to form the hadronic current. Due to negative parity of the pion (remember that pion is a pseudoscalar), the most general form of hadronic current for pion production must involve the γ_5 matrix [8]. Therefore, the general hadronic current (more precisely the "hadronic vertex") for our transition current is given by [19]

$$J^\mu = \left(A\tilde{\gamma}^\mu + B\tilde{P}^\mu + Cp_\pi^\mu\right)\gamma^5 + \left(D\tilde{\gamma}^\mu + E\tilde{P}^\mu + Fp_\pi^\mu\right)\gamma^5 \not{q},$$

where $P = (p+p')/2$ and what the tilde on 4-vectors represents comes from gauge invariance requirement, e.g., for γ matrix, $\tilde{\gamma}^\mu = \gamma^\mu - q^\mu \not{q}/q^2$. The hadronic transition matrix, evaluated between the initial and final spinors, yields an equivalent expression for J^μ that can be given in terms of 3-Pauli matrix [9] and unit vectors of pion and virtual photon's 3-momenta in hadronic CM frame: $\hat{\mathbf{p}}_\pi = \hat{\mathbf{p}}_{\pi,\text{CM}}$ and $\hat{\mathbf{q}} = \hat{\mathbf{q}}_{\text{CM}}$. In this form of J^μ, the CGLN amplitudes F_i come into sight [16]. The hadronic current $J^\mu = (\rho, \boldsymbol{J})$ is given by

$$\begin{aligned}\mathbf{J} = \frac{4\pi W}{M}\big[&iF_1\tilde{\boldsymbol{\sigma}} + F_2\left(\boldsymbol{\sigma}\cdot\hat{\mathbf{p}}_\pi\right)\left(\boldsymbol{\sigma}\times\hat{\mathbf{q}}\right) + iF_3\left(\boldsymbol{\sigma}\cdot\hat{\mathbf{q}}\right)\tilde{\mathbf{p}}_\pi + iF_4\left(\boldsymbol{\sigma}\cdot\hat{\mathbf{p}}_\pi\right)\tilde{\mathbf{p}}_\pi \\ &+iF_5\left(\boldsymbol{\sigma}\cdot\hat{\mathbf{q}}\right)\hat{\mathbf{q}} + iF_6\left(\boldsymbol{\sigma}\cdot\hat{\mathbf{p}}_\pi\right)\hat{\mathbf{q}}\big],\end{aligned} \tag{1.9a}$$

$$\rho = \frac{4\pi W}{M}\left(iF_7\boldsymbol{\sigma}\cdot\hat{\mathbf{p}}_\pi + iF_8\boldsymbol{\sigma}\cdot\hat{\mathbf{q}}\right), \tag{1.9b}$$

[7] We explain later what pion-nucleon or hadronic CM frame means, see Fig. 1.4 for the time being.

[8] That is because γ_5 anticommutes with the parity operator, which gives away a negative sign when parity is applied on terms with γ_5, e.g., $\bar{\psi}\gamma_5\psi \xrightarrow{\text{Parity}} \bar{\psi}'P\gamma_5P^{-1}\psi' = -\bar{\psi}'\gamma_5 PP^{-1}\psi' = -\bar{\psi}'\gamma_5\psi'$.

[9] That is a 3-vector made out of the three Pauli matrices, i.e., $\boldsymbol{\sigma} = \left(\sigma^1, \sigma^2, \sigma^3\right)$.

where $\tilde{\boldsymbol{\sigma}} = \boldsymbol{\sigma} - (\boldsymbol{\sigma} \cdot \hat{\mathbf{q}})\,\hat{\mathbf{q}}$ and alike. The amplitudes (or structure functions) F_1, F_2, F_3, F_4 describe the transverse current, while the longitudinal component of the current is expressed through F_5 and F_6. They ought to depend on the three scalar variables of the process.

Additionally, the structure functions F_i are complex due to their dependence on isospin invariants originating from J^μ being sandwiched between two isospin states: the initial proton state and the pion-proton final state [10]. It is worth mentioning here that even though the situation in the threshold region is much less complicated, when calculating cross section at arbitrary W^2 (including resonances, etc.) all six amplitudes are contributing in electroproduction while four are required for photoproduction.

As mentioned earlier, the CGLN amplitudes can be expanded in terms of the derivatives of Legendre polynomials for which the method is called multipole decomposition. We do not go through the details of the decomposition here, but the decomposition begins when one wants to identify the initial and final hadronic states by expanding them in terms of total angular momentum and isospin states. In that realm, which is basically the familiar partial wave analysis discussed for simpler cases in textbooks, the amplitudes depend on the contributions of different angular momentum partial waves of the hadronic states in a series expansion. The amplitudes decomposed into a multipole series are given by [23]

$$F_1 = \sum_{l\geqslant 0} \Big\{ (lM_{l+} + E_{l+})\, P'_{l+1}(x) + [(l+1)\, M_{l-} + E_{l-}]\, P'_{l-1}(x) \Big\}, \tag{1.10a}$$

$$F_2 = \sum_{l\geqslant 1} [(l+1)\, M_{l+} + lM_{l-}]\, P'_l(x), \tag{1.10b}$$

$$F_3 = \sum_{l\geqslant 1} \Big[(E_{l+} - M_{l+})\, P''_{l+1}(x) + (E_{l-} + M_{l-})\, P''_{l-1}(x) \Big], \tag{1.10c}$$

$$F_4 = \sum_{l\geqslant 2} (M_{l+} - E_{l+} - M_{l-} - E_{l-})\, P''_l(x), \tag{1.10d}$$

$$F_5 = \sum_{l\geqslant 0} \Big[(l+1)\, L_{l+} P'_{l+1}(x) - lL_{l-} P'_{l-1}(x) \Big], \tag{1.10e}$$

$$F_6 = \sum_{l\geqslant 1} [lL_{l-} - (l+1)\, L_{l+}]\, P'_l(x), \tag{1.10f}$$

where x is the cosine of the angle of emission of pion in hadronic CM frame $x = \cos\theta_{\pi,\mathrm{CM}}$. The energy dependent (more precisely, W^2 and Q^2 dependent) multipoles $E_{l\pm}$ and $M_{l\pm}$ refer to transitions initiated by electric and magnetic radiation, respectively, leading to final states of orbital angular momentum l and total angular momentum $l \pm 1/2$. The same convention stands

[10] The isospin analysis of pion-nucleon system is discussed in Ref. [22].

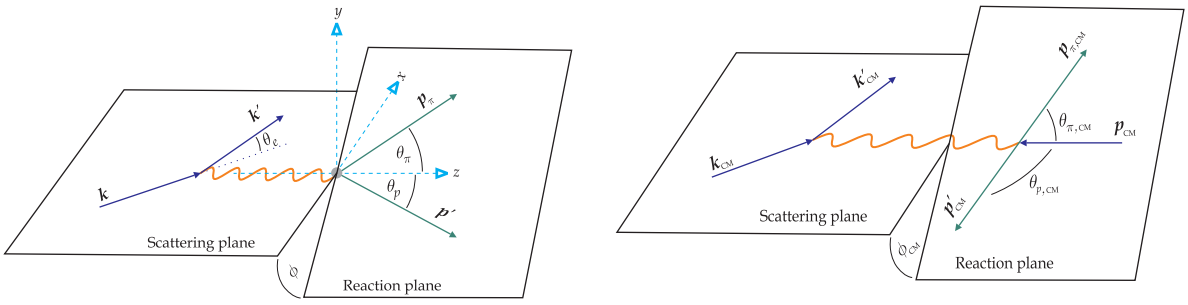

Lab frame π-N CM frame

Figure 1.4: The schematic depiction of the kinematics for a π^0 electroproduction: in Lab frame (typical coincidence experiment); and in pion-nucleon center-of-momentum frame. Note that the momemta are all three-vectors and the scattering plane is defined by the momenta of incoming and outgoing electrons, which is the $x-z$ plane in the lab frame.

for longitudinal multipoles $L_{l\pm}$. Superscripts $(\pm, 0)$ may be added to amplitudes to designate the isospin character of the transition.

The multipole expansion of amplitudes F_i, provides practical means using which the hadronic transition current J_μ and therefore the hadronic tensor $W_{\mu\nu}$ can be calculated. The cross section then can be obtained in terms of multipoles. Let us remind ourselves that the cross section for the scattering of a beam of particles $\mathcal{A}$ off a target of particles $\mathcal{B}$ resulting final particles f has a compact form of [24]

$$d\sigma = \frac{1}{2E_{\mathcal{A}}E_{\mathcal{B}}\left|v_{\mathcal{A}} - v_{\mathcal{B}}\right|}\left(\prod_f \frac{d^3p_f}{(2\pi)^3}\frac{1}{2E_f}\right)\left|\mathcal{M}\left(p_{\mathcal{A}}, p_{\mathcal{B}} \to \{p_f\}\right)\right|^2 (2\pi)^4\,\delta^4\left(p_{\mathcal{A}} + p_{\mathcal{B}} - \sum_f p_f\right). \quad (1.11)$$

The invariant amplitude squared $|\mathcal{M}|^2$, as already seen in Eq. 1.3 is the product of leptonic and hadronic tensors, regardless of the sum or averaging mechanism for the spin degrees of freedom. The hadronic tensor for an unpolarized target, according to Eqs. 1.6 and 1.9, is defined by

$$W_{\mu\nu} = \left(\frac{M}{4\pi W}\right)^2 \frac{1}{2}\sum_{\text{spins}}\sum_X \langle X(P_X)|\,\hat{J}_\mu(0)\,|N(p)\rangle^*\,\langle X(P_X)|\,\hat{J}_\nu(0)\,|N(p)\rangle, \quad (1.12)$$

where the factor $M/4\pi W$ is there due to the definition of the hadronic current J_μ in Eq. 1.9. We must remind ourselves, nonetheless, that for polarized targets or experiments which measure the polarization of the recoiled nucleon, the averaging and summing over spins in Eq. 1.12 is meaningless. As we already know, due to gauge invariance the hadronic current is conserved,

$q^\mu W_{\mu\nu} = q^\nu W_{\mu\nu} = 0$, for that reason all time-like components of $W_{\mu\nu}$ can be replaced by space-like components in the direction of $\hat{\mathbf{q}} = \hat{\mathbf{z}}$. This corresponds to interactions with partially polarized virtual photons which lead to defining two "polarization degrees" for these virtual photons. First, the *degree of transverse polarization* [9]

$$\epsilon = \frac{1}{1 + 2\frac{|\mathbf{q}|^2 \tan^2 \theta_e/2}{Q^2}}\,, \tag{1.13}$$

where the three vector $\mathbf{q}$ and scattering angle θ_e are in lab frame. And second, the *degree of longitudinal polarization* [9]

$$\epsilon_L = \frac{Q^2}{q^2_{0,\mathrm{CM}}}\epsilon\,, \tag{1.14}$$

with virtual photon energy in CM frame

$$q_{0,\mathrm{CM}} = \frac{W^2 - M^2 - Q^2}{2W}\,. \tag{1.15}$$

The leptonic tensor for an unpolarized beam is simply given by Eq. 1.4, but for polarized electrons with longitudinal helicity polarization (i.e., $\boldsymbol{\sigma} \cdot \mathbf{k} = \pm\mathbf{1}$), the leptonic tensor is given by

$$L^{\mu\nu} = \frac{e^2}{2m^2}\left(2K^\mu K^\nu + \frac{1}{2}q^2\eta^{\mu\nu} - \frac{1}{2}q^\mu q^\nu + ih\varepsilon^{\mu\nu\alpha\beta}q_\alpha K_\beta\right), \tag{1.16}$$

where $K = (k + k')/2$, h is the helicity of the beam (i.e., $h = \pm 1$) and $\varepsilon^{\mu\nu\alpha\beta}$ is the totally antisymmetric tensor of rank four, i.e., the well known Levi-Civita tensor. Obviously, if we set $h = 0$ in Eq. 1.16 the unpolarized tensor of Eq. 1.4 is recovered. Knowing the leptonic tensor and hadronic tensor at least at structural level , we can compute the invariant amplitude and once the reference frame is fixed the cross section can be obtained (after phase space integrations) through its definition of Eq. 1.11.

The coordinate systems that are of use are lab and the so-called $\pi - N$ center-of-momentum frames. The kinematics in both frames are shown in Fig. 1.4. A typical coincidence pion production experiment follows the schematic of lab frame in Fig. 1.4, where the electron stays on one plane, the *scattering plane*, and pion runs off into a different plane, the *reaction plane*. The lab coordinate system is set so that $\hat{\mathbf{z}} = \hat{\mathbf{x}} \times \hat{\mathbf{y}}$, $\hat{\mathbf{y}} = \hat{\mathbf{k}} \times \hat{\mathbf{k}}' \big/ \sin\theta_e$, and $\hat{\mathbf{q}} = \hat{\mathbf{z}}$, where θ_e is the electron's scattering angle. The angle between the two planes is called the *out of plane angle* and is denoted by ϕ in both frames (i.e., ϕ for lab frame and ϕ_{CM} for the $\pi - N$ center-of-momentum frame, see Appendix A and Fig. 1.4).

The $\pi - N$ center-of-momentum frame (or hadronic CM frame), which we call CM from now on, is the frame where the reaction plane is the center-of-momentum plane of the recoiled

proton and the pion. The initial proton in the CM frame (the target in lab) is moving in the opposite direction of the 3-momentum transfer $\mathbf{q}$. As expected, physical quantities take simpler forms in CM frame. For example, the scalars of the process are the same in every frame including W which at the threshold takes the convenient form of $W_0 = M + m_\pi$ in the CM frame. Appendixes A and B give analytical descriptions for the geometry of the scattering and reaction planes and the definitions of CM and lab frames.

Considering all this, the electroproduction differential cross section has been cast in the form [23, 25]

$$\frac{d\sigma}{dE' d\Omega_{e'} d\Omega_{\pi,\mathrm{CM}}} = \Gamma \frac{d\sigma}{d\Omega_{\pi,\mathrm{CM}}} , \tag{1.17}$$

where Γ is the flux of the virtual photon field

$$\Gamma = \frac{\alpha E'}{4\pi^2 M E Q^2} \frac{W^2 - M^2}{1-\epsilon} , \tag{1.18}$$

and

$$\begin{aligned} \frac{d\sigma}{d\Omega_{\pi,\mathrm{CM}}} = \frac{2\left|\mathbf{p}_{\pi,\mathrm{CM}}\right| W}{W^2 - M^2} \Big[& R_T + \epsilon_L R_L + \sqrt{2\epsilon_L (1+\epsilon)} \cos\phi_{\mathrm{CM}} R_{TL} + \epsilon \cos 2\phi_{\mathrm{CM}} R_{TT} \\ & + h \sqrt{2\epsilon_L (1-\epsilon)} \sin\phi_{\mathrm{CM}} R_{TL'} + h \sqrt{1-\epsilon^2} R_{TT'} \Big] , \end{aligned} \tag{1.19}$$

where R_i are called structure (or response) functions, which are expressed in terms of the components of the hadronic tensor (see Ref. [9]) and h is the helicity of the electron beam. Equally so instead of R_i, one uses virtual photon cross sections

$$\frac{d\sigma_i}{d\Omega_{\pi,\mathrm{CM}}} = \frac{2\left|\mathbf{p}_{\pi,\mathrm{CM}}\right| W}{W^2 - M^2} R_i , \tag{1.20}$$

with $i = T, L, TT, TL, TL', TT'$. These virtual photon cross sections are also denoted by a simplified notation of σ_i, with $i = T, L, TT, TL, TL', TT'$, and even called "structure functions" as well. The last term in Eq. 1.19 (TT') is only relevant for polarized target or when the polarization of the recoiled nucleon is observed. The fifth term (TL') can be ignored if the beam is not polarized. For our experiment, which employed a polarized beam on unpolarized target, the last term is inapplicable while all other terms should be kept.

A note here is necessary regarding the indexes of the structure functions R. As we already explained, due to current conservation the hadronic tensor $W_{\mu\nu}$ is coupled to the virtual photon through spacelike components , i.e., $\mu, \nu = x, y, z$. Since z is in the direction of virtual photon's propagation (longitudinal polarization degrees of freedom for γ^*) and x, y are perpendicular to the latter (transverse polarization degree of freedom for γ^*) the indexes of the structure

functions R are named according to the appearance of various combinations of hadronic tensor components with x, y, and z indexes in them. For example, R_T involves W_{xx} and W_{yy}, i.e., $R_T = \left(W_{xx} + W_{yy}\right)/2$, and R_L involves W_{zz}. For Full expressions of structure functions in terms of hadronic tensor components and their CGLN expansions see Ref. [9]. With a polarized beam an asymmetry function $A_{TL'}\left(\theta_{\pi,\mathrm{CM}}\right)$ can be defined, i.e.,

$$A_{TL'}\left(\theta_{\pi,\mathrm{CM}}\right) = \frac{\sigma^{+}\left(\theta_{\pi,\mathrm{CM}}\right) - \sigma^{-}\left(\theta_{\pi,\mathrm{CM}}\right)}{\sigma^{+}\left(\theta_{\pi,\mathrm{CM}}\right) + \sigma^{-}\left(\theta_{\pi,\mathrm{CM}}\right)} = \frac{\sqrt{2\epsilon_L\left(1-\epsilon\right)}R_{TL'}}{R_T + \epsilon_L R_L - \epsilon R_{TT}}\ , \tag{1.21}$$

where $\sigma^{\pm}$ are *differential* cross sections at $\phi_{\mathrm{CM}} = 90^{\circ}$ with beam polarization parallel (+) and antiparallel (-). At a fixed $\theta_{\pi,\mathrm{CM}}$, the asymmetry $A_{TL'}$ depends only on Q^2 and ΔW through Rs.

At threshold, the cross section is obviously zero since the generated pion is not moving [11]. A non-vanishing cross section, then, exists above threshold. Near threshold is where the theoretical calculations for hadronic tensor are the simplest. One reason is the limited extent of the multipole decomposition, which for near threshold can be narrowed down to s and p waves limiting the number of multipoles needed.

To comprehend this, we should go through some practical procedures. If we replace structure functions R_i with their equivalents in terms of CGLN amplitudes F_i and then replace those with their multipole expansion series, Eqs. 1.10, the cross section will become an complicated-looking expression involving series of multipoles. Through the multipole decomposition of F_i, the dependence on hadronic momenta is passed onto the multipoles (partial waves) $E_{l\pm}$, $M_{l\pm}$, $L_{l\pm}$, which depend on pion's three-momentum $\sim \left|\mathbf{p}_{\pi,\mathrm{CM}}\right|^{l}$. Near threshold where $\left|\mathbf{p}_{\pi,\mathrm{CM}}\right| \to 0$, we would like to keep terms no more than $l = 0, 1$ (s and p waves) resulting in a cross section dominated by terms involving E_{0+} and L_{0+} [12].

Up to this point, we have obtained the cross section in terms of unidentified hadronic functions, which reflects our not-so-perfect knowledge of hadrons. In the following section, we go over the theoretical tools of evaluating these hadronic functions.

1.1.3 Neutral Pion Electroproduction: Multipole Functions

As discussed in previous section the structure functions R_i are in terms of CGLN amplitudes F_i, which in turn have been expanded into multipole expansion series of Eqs. 1.10. These multipoles are obtained through both theoretical calculations and experimental observations,

[11] This can be checked for by setting $\left|\mathbf{p}_{\pi,\mathrm{CM}}\right| = 0$ in Eq. 1.19.

[12] Multipoles with $l = 1$ contribute as well, even though they appear at higher powers of $\left|\mathbf{p}_{\pi,\mathrm{CM}}\right|$.

which provide a test for theoretical frameworks. The theoretical approaches can be sorted into three classes:

- LETs
- ChPT
- Models based on phenomenological effective $\pi - N$ interactions

We explain only the principles and methodology of LETs, and ChPT in dealing with neutral pion electroproduction near threshold. In doing so, we avoid addressing the lengthy calculations of identifying multipoles, which can be found in references given for each method. In addition, we briefly discuss two phenomenological models, whose predictions are in good agreement with recent experimental data.

1.1.3.1 Electroproduction Multipoles from Low Energy Theorems

Low energy theorems have been developed to determine the S matrix and, therefore, amplitudes for reactions involving photons and pions. In deriving the S matrix, Lorentz and electromagnetic gauge invariance plus partial conservation of axial current are demanded. Then the corresponding amplitudes in the low-energy limit are expressed in terms of low-energy hadronic constants such as mass, magnetic moments and relevant coupling constants.

The LETs are exact in case of photons but lead to vanishing matrix elements for pions on mass shell. To compensate this, the amplitudes are evaluated in the limit of "soft pions" (massless pions) by expansion into power series of $\mu = m_\pi/M$ (M being the mass of nucleon).

There are two methods of derivations for LETs: one through current algebra due to Adler and Gillman [26] and Weisenberger [27] and the other through the consideration of chiral symmetry and group theoretical tools by Furlan et al. [28, 29]. The work of Kroll and Ruderman [15] is a prelude to the more involved LETs of the abovementioned works.

The LETs are derived by demanding symmetries on the hadronic current of the process. In that sense, they are model independent. However when PCAC is considered, the S matrix contains terms that can be calculated through specific theory of the strong interaction, such as QCD or phenomenological models. For example, and for π^0 electroproduction, the vector and axial currents of the pion-nucleon system and their interaction current, which appear in an LET-derived S matrix, can be expressed in terms of the quark degrees of freedom of QCD.

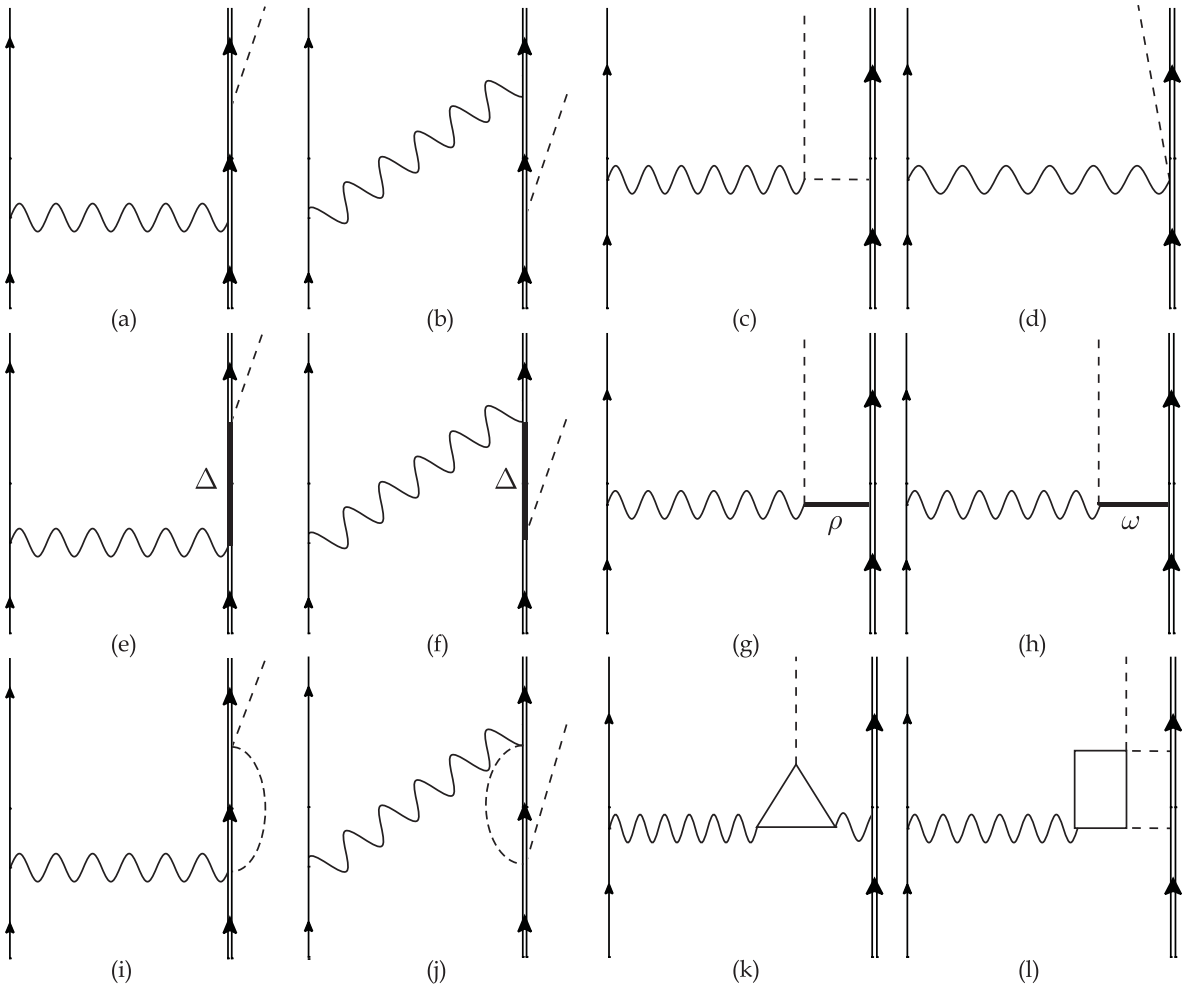

Figure 1.5: Diagrams contributing to π^0 electroproduction: (a) direct, (b) crossed nucleon pole, (c) pion pole, (d) Kroll-Ruderman, (e) and (f) isobar excitation, (g) ρ pole, (h) ω pole, (i) and (j) rescattering, (k) triangle anomoly, (l) square anomoly.

Conceptually speaking, once the covariant scattering amplitude $\mathcal{M}$ is obtained through LET considerations and expanded about $\mu = m_\pi/M$, the multipoles can be identified by comparison with the multipole-decomposed $\mathcal{M}$ of the last section.

To determine the hadronic current, many processes can be identified and included in its evaluation. For example, the diagrams of Fig. 1.5 show some of the possibilities for pion electroprduction (both charged and neutral). The LET, nonetheless, emphasizes that the threshold behavior is governed by the Born approximation terms, i.e., those in Figs. 1.5 (a-d).

In case of exact chiral symmetry, pion mass would be zero, which means $\mu = 0$. The expansion in μ is dominated by $\mu^0 = 1$ term for charged pion, while it starts with $O(\mu)$ term for π^0 production. For this reason, neutral pion production is preferred as it provides chiral symmetry breaking evidence at leading order of μ.

Whether or not the LET-extracted multipoles conform to the experimental results is what we will discuss in section 1.2, when we go over experimental works. Another method of calculating multipoles is through the $\pi - N$ interactions framed in ChPT Lagrangian. We will give a short reminder of QCD and its two phases and then review the low energy phase in the context of ChPT.

1.1.3.2 Electroproduction Multipoles from Chiral QCD

Quantum Chromodynamics, the gauge theory based on the color group $SU(3)_c$, is particularly complicated because it is not perturbative except at very high energies. Its description, nonetheless, is misleadingly simple: eight massless vector bosons (gluons) interacting with one another and with colored fermions (quarks) through vector currents. The masslessness of gluons means that the color group is intact (i.e., not broken by the Higgs boson's vacuum) and the gluon self-interactions come from the fact that $SU(3)_c$ is non-abelian. The gluons carry no electroweak quantum numbers; however they affect electroweak interactions through their couplings to quarks which carry both color and electroweak quantum numbers.

The gluon self-interactions cause the QCD coupling constant to grow at large distances (infrared slavery) and decline at short distances (asymptotic freedom). The experimental data on low energy strong interaction suggest that only color-neutral states (hadrons) which are immune to QCD forces can exist (the confinement hypothesis). In that sense, QCD seems to have two phases. At short distances or high energies, where the quark-gluon coupling is weak, quarks are quasi-free and QCD is the theory of quarks and gluons. This is the area of

perturbative QCD, capable of carrying out calculations for high energy events, for example in collider experiments. At large distances or low energies, the quark and gluon picture is to be replaced with an alternate description of strong interaction, one that is in terms of colorless states: baryons and mesons. We currently cannot obtain the baryon-meson phase of the QCD from first principles but we can study if and how the symmetries of QCD are realized in that phase.

The QCD scale Λ_{QCD}, provides a means by which we can differentiate between these two states of the theory of strong interaction. The quarks can be segregated into two groups depending on their masses compared to this scale. There are two quarks u, d, with masses much smaller than Λ_{QCD}, and another quark s, with a mass comparable to Λ_{QCD}. These three quarks can be thought of as the building blocks of the baryon-meson phase of QCD. The other three quarks c, b, t, have masses larger than Λ_{QCD} and are not expected to play a role in the low-energy description of QCD.

All this leads to the chiral picture of QCD at low energies. Here by "chiral" we simply mean massless quarks. The terminology comes from the helicity of massless fermions, which is referred to as chirality. For a massless fermion, which is the solution to massless Dirac equation in Weyl or "chiral" representation of γ matrices, the particle (positive energy state) has only positive helicity and vice versa for antiparticle [13]. This explains the term chirality "the sense of screw" as massless fermions can only have one state of chairality (helicity) which is identical to their energy: positive or negative depending on their energy. It turns out that the Lagrangian for a massless fermion can be divided into two parts: a purely left-handed and a purely right-handed, which implies an additional symmetry, the so-called chiral symmetry.

To start, let us turn the electroweak interaction off (considering QCD alone) and set the masses of the three light quarks to zero. In this limit (chiral limit) the *light quark* QCD Lagrangian consists of the vector boson part plus the gauged kinetic energy term of the light quarks (no mass terms), that is

$$\mathcal{L}_{\text{QCD}}^{\text{chiral}} = -\frac{1}{2}\text{Tr}\left(\tilde{G}^{\mu\nu}\tilde{G}_{\mu\nu}\right) + i\sum_{j=1}^{3}\bar{q}_j \not{D} q_j.$$

In the above equation $\tilde{G}^{\mu\nu} = \sum_{a=1}^{8} \hat{T}_a G_a^{\mu\nu}$, with $\hat{T}_a = \hat{\lambda}_a \big/ 2$ being the generators of SU(3)$_c$, and q_j is the color triplet quark field, where the sum over the colors is implicit. Since there is no mass

[13] Antiparticle is a particle which identifies with the negative energy solution of Dirac equation, in the context of Hole theory.

term to mix the left- and right-handed quarks, the kinetic energy term of the quark fields can be split into left- and right-handed terms (that is because one can write $q = q_L + q_R$)

$$\mathcal{L}_{\text{QCD}}^{\text{chiral}} = -\frac{1}{2}\text{Tr}\left(\tilde{G}^{\mu\nu}\tilde{G}_{\mu\nu}\right) + i\sum_{j=1}^{3}\bar{q}_{Lj}\not{D}q_{Lj} + i\sum_{j=1}^{3}\bar{q}_{Rj}\not{D}q_{Rj}.$$

Note that terms with mixed chiralities like $\bar{q}_{Rj}\not{D}q_{Lj}$ vanish. The above Lagrangian exhibits a very large global symmetry $\text{SU}(3)_L \otimes \text{SU}(3)_R \otimes \text{U}(1)_B$ on the three light quarks. To stay focused on the chiral symmetry, we can ignore the Baryon number symmetry $\text{U}(1)_B$. Obviously if we had only considered two flavors of quarks u and d, as "light", the chiral symmetry would have diminished to $\text{SU}(2)_L \otimes \text{SU}(2)_R$. The chiral symmetries of massless QCD are broken (because the light quarks are not massless), therefore the $\text{SU}(3)_L \otimes \text{SU}(3)_R$ is reduced to its maximal vectorial subgroup $\text{SU}(3)_L \otimes \text{SU}(3)_R \to \text{SU}(3)_{L+R}$. It is believed that the symmetry breaking takes place through the condensation of quark pairs in the vacuum (in analogy to the BCS theory of superconductivity [30]). That means the QCD force between quarks and antiquark forces quark-antiquark condensates to form in the vacuum or in the language of Nambu-Goldstone theorem $\left\langle q_{Lj}^{\dagger}q_{Rk}\right\rangle \neq 0$. In the spontaneous breaking of $\text{SU}(3)_L \otimes \text{SU}(3)_R \to \text{SU}(3)_{L+R}$, there are eight Nambu-Goldstone bosons (eight generators are "broken"), an octet field under the $\text{SU}(3)_{L+R}$, which turn out to be the psuedoscalar meson octet of Fig. 1.1. On the other hand, If we chose a two-flavor chiral QCD consisting of u and d, then the spontaneous symmetry breaking of $\text{SU}(2)_L \otimes \text{SU}(2)_R \to \text{SU}(2)_{L+R}$ would yield three Nambu-Goldstone bosons (three generators are "broken"). That is a triplet field under the $\text{SU}(2)_{L+R}$, which is identified as pion triplet.

There is also another way of breaking the chiral symmetry of light-quark QCD and that is by adding mass terms to the Lagrangian. That is called explicit chiral symmetry breaking. In such a case, the consequences of spontaneous symmetry breaking still can be considered because the masses are small, treating the masses as perturbation. That is in particular applicable in a two-flavor chiral QCD. One of the consequences of considering a perturbed chiral QCD theory is its effect on the masses of the Nambu-Goldstone bosons, which turn out to be much lighter than ordinary hadrons [14].

In this framework, the chiral effective Lagrangian of QCD can be written [31], which includes the pseudoscalar mesons and their interaction with light quarks and external field. Extension to this Lagrangian has been made to include nucleon fields, providing a platform to

[14] That is the case more for pions than other mesons of the octet, e.g., kaons.

study the reactions involving pseudoscalalr mesons and nucleons. In that case, there will be a new mass scale established by the presence of hadronic fields. There are several treatments to this issue [32], but all in all when in work such platform is called heavy baryon chiral perturbation theory (HBChPT).

ChPT, as an effective theory, deals with two types of expansion. One in terms of small quark mass and one in terms of small (~ 1 GeV) external momenta or mesonic mass, denoted by q. Each element of Lagrangian is assigned a so-called chiral dimension, corresponding to the number of derivatives or the power of q, say $O(1), O(2), \ldots$. The Lagrangian then becomes the sum of Lagrangians, which are terms that have been gathered according to their chiral dimension by power counting, that is $\mathcal{L}^{(1)}$, $\mathcal{L}^{(2)}$, etc..

The Nambu-Goldstone boson scattering and production are of great importance in ChPT. The production of pions (either photo- or electroproduction) falls in the category. Of the three pions, π^0 production is peculiarly interesting. First of all, the phase of the amplitudes for pion production is sensitive to the inclusion of the up and down quarks masses through unitarity of the final states. In addition, for π^0 production the s-wave multipole E_{0+} vanishes in chiral limit, which makes the π^0 production the most sensitive of all pions to chiral symmetry breaking. For that reason, new experiments are mainly on π^0 production.

Between photo- and electroproduction of π^0, there is a preference toward electroproduction. In case of electrons being the projectiles of choice, the energy and momentum transfered to the target can be varied independently. This is simply due to the kinematical difference between an on-shell $q^2 = 0$ (real) and off-shell $q^2 \neq 0$ (virtual) photon.

Let us mention here that in the framework of HBChPT, and to one-loop approximation there is a great success for ChPT in predicting cross sections and asymmetry functions for pion photoproduction. That, as we will see in the next section, is not the case for electroproduction. In fact, earlier ChPT calculations of photoproduction showed that the LETs near threshold needed modification and p-wave LETs were derived [33]. Additionally, it was shown that s-wave multipoles converge slowly [34], emphasizing the need for p-wave calculations.

To calculate π^0 electroproduction multipoles and ultimately cross section in HBChPT, the effective Lagrangian to the desired power of q is identified first. Then all possible diagrams contributing to the process that can be obtained in the framework of the effective Lagrangian are computed. The diagrams in current calculations include tree level (equivalent to the Born terms of LETs) and one-loop diagrams. All this leads to the determination of hadronic current.

The extraction of multipoles to certain orders of q is then what follows. In HBChPT paradigm, the s-wave multipoles alone are not sufficient. The p-wave multipoles are also considered and evaluated [15]. Several low energy constants, however, are needed to carry out the calculations. These constants are obtained from various sources, e.g., nucleon electromagnetic form factors or even fits to experimental data.

Multipoles provide cross section and asymmetry function for π^0 electroproduction, but as mentioned above, the agreement with experimental data near threshold has been poor, unlike the photoproduction case. We will discuss this disagreement in the next section when we go over the experimental investigation of π^0 electroproduction.

1.1.3.3 Phenomenological Models

There is a range of pion-production phenomenological models for photon (both real and virtual) energies from threshold and above (e.g., see Ref. [9] and references therein). The data from two of these models, namely MAID[16] [38] and DMT[17] [39], are presented in this work along with those of ChPT. These phenomenological models have shown better consistency with π^0 electroproduction experimental data at both cross section and asymmetry levels, near threshold, compared to ChPT. We only describe the frameworks of these two models here since the details are rather involved, for which one can refer to the corresponding references.

The MAID Model: The MAID model utilizes CGLN amplitudes which are expressed in terms of isospin amplitudes [40], as a consequence of considering isospin conservation. It includes resonance contributions in multipoles (when applicable) in Breit-Wigner form[18], whose Q^2 dependence are determined through helicity amplitudes or quark multipole moments [41]. Non-resonant terms or Born terms with an energy-dependent mixed pseudovector-pseudoscalar πNN coupling and vector meson exchange describe the non-resonant contributions to multipoles. The model demands unitarity when deriving the relevant amplitudes.

The DMT Model: The DMT employs a meson-exchange model to compute transition or T matrix. The model gets potentials for Born and heavy meson exchanges from MAID and

[15] The latest HBChPT calculations determine s-wave multipoles up to q^4 and q^5 order and p-wave multipoles up to q^3 order [35–37].

[16] According to Lothar Tiator, MAID was chosen for the model as it provides services to science as a maid does.

[17] Acronym for Dubna-Mainz Taipei.

[18] The Breit-Wigner distribution, which is most often used to model resonances, is a probability distribution in the form $\sim \left[(E^2 - M^2)^2 + M^2\Gamma^2\right]^{-1}$, where E is the CM energy that produces the resonance, M is the mass of the resonance, and Γ is the resonance's width.

other portentials from ChPT. The resonances are included in Breit-Wigner form. Final state interactions are applied through scatterings of off-shell pion from the nucleon [42, 43]. The importance of final state interactions for π^0 production near threshold has been shown in several dynamical model studies of the subject (e.g., see Ref. [44]).

Phenomenological models in general employ effective field theories for making theoretical predictions, for which experimental data are used as a guide. MAID and DMT provide data for π^0 electroproduction, which are in better agreement with experiment compared to ChPT. The DMT model, in particular, achieves an interestingly good agreement with experimental π^0 electroproduction asymmetry data.

1.2 Experimental Investigations

Similar to the theoretical treatment of neutral pion production, the photo- and electroproduction of π^0 are correlated in the experimental handling of the phenomena. The LETs were first applied to photoproduction and the first experimental works were on photoproduction as well. Over the last two decades, the experimental focus has mostly shifted toward π^0 electroproduction at threshold, as a testing tool for ChPT.

The first experimental works on photoproduction were carried out at Saclay [45] and Mainz [46] to examine the LET results for the s-wave multipoles at threshold. Experimentally extracted value of E_{0+} multipole at threshold from these two experiments was not in agreement with that of LETs'. Even though the disagreement created a lot of debate within the community on what may have gone unnoticed in the LETs' calculations, the reanalysis of data [9, 47, 48] showed a good agreement between LETs' prediction of E_{0+} value at threshold and experimental values.

Experiments on photoproduction at SAL[19] [49] and MAMI[20] [50] gave smaller value for E_{0+} at threshold in agreement with ChPT results [51]. Further analysis of MAMI experiment [52] revealed the predicted "unitary cusp" for the s-wave multipole E_{0+}, which is due to the two step $\gamma p \to \pi^+ n \to \pi^0 p$ reaction, as another close agreement with one-loop ChPT calculations.

The first near threshold π^0 electroproduction experiment was carried out at NIKHEF[21] [53, 54]. The quantity $a_0 = |E_{0+}|^2 + \epsilon_L |L_{0+}|^2$, which is deterministic of total cross section, was

[19] Acronym for Saskatchewan Accelerator Laboratory.
[20] Acronym for Mainz Microtron.
[21] Acronym for Nationaal Instituut voor Kernfysica en Hoge-EnergieFysica.

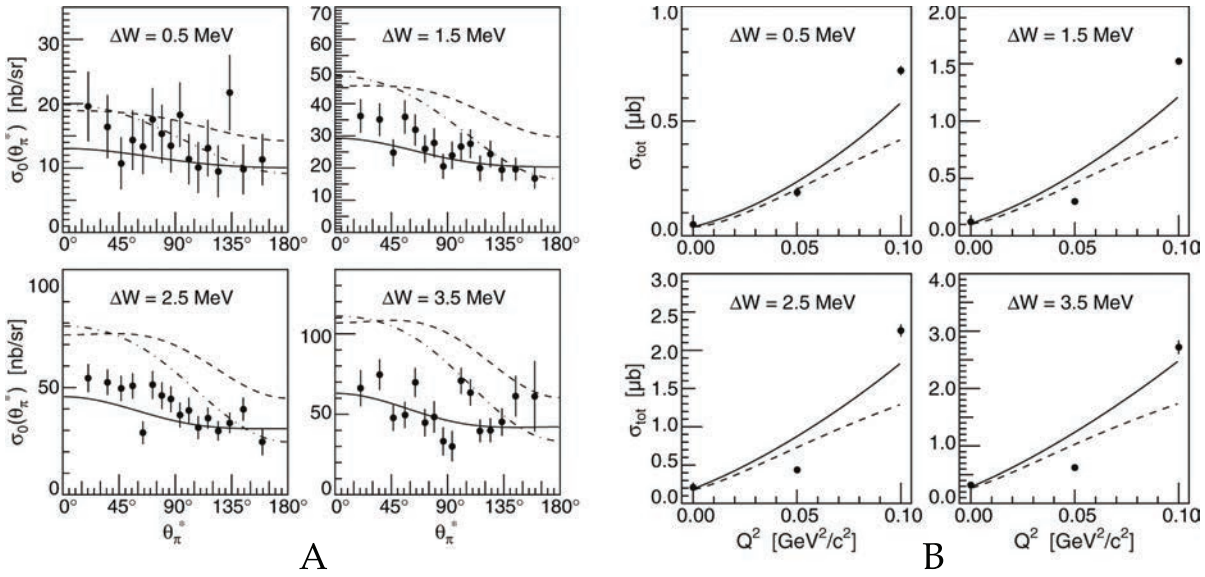

Figure 1.6: π^0 electroproduction virtual photon cross section $\sigma_0 = \sigma_T + \epsilon_L \sigma_L$ versus pion's angle in CM frame at $Q^2 = 0.05\,(\mathrm{GeV}/c)^2$ (**A**) and total cross section σ_{tot} versus Q^2 (**B**): circles are experimental data of Ref. [56]; in (**A**) solid line represents an *s*- and *p*-wave fit; HBChPT [36, 37] and MAID model [38] values are the dashed and dash-dotted lines in (**A**) and the solid and dashed lines in (**B**), respectively. σ_{tot} at $Q^2 = 0$ [57] and $Q^2 = 0.1\,(\mathrm{GeV}/c)^2$ [58] are external.

measured close to the threshold for $Q^2 = 0.05\,(\mathrm{GeV}/c)^2$. The *s*-wave multipoles were extracted through practical means and extrapolated down to $Q^2 = 0$. The Q^2 dependence of a_0 was in agreement with ChPT calculations [55].

Another near threshold electroproduction experiment [59, 60] was performed at NIKHEF a few years later, aiming at obtaining E_{0+} and L_{0+} with their energy dependence, separately. This experiment measured the angular distribution of π^0 for $1\,\mathrm{MeV} \leqslant \Delta W \leqslant 14\,\mathrm{MeV}$ at $Q^2 = 0.1\,(\mathrm{GeV}/c)^2$. This range of W includes the π^+ threshold and therefore allowed for a possible observation of the unitarity cusp, which was not observed. Instead, a variation in the value of L_{0+} around π^+ threshold was detected, contrary to theoretical predictions.

Following these two works, a series of near threshold electroproduction experiments were performed at MAMI with specific intent at testing ChPT over the span of a decade. The first experiment [58] of this series used unpolarized beam and target and measured virtual photon cross sections [22] (see Eq. 1.20) and differential cross sections for $0\,\mathrm{MeV} \leqslant \Delta W \leqslant 4\,\mathrm{MeV}$, at $Q^2 = 0.1\,(\mathrm{GeV}/c)^2$. Additionally, the real part of *s*-wave multipoles were provided.

[22] Virtual photon cross sections, Eq. 1.20, are also referred to as "structure functions", which should not be confused with the response or structure functions R_i of Eq. 1.19.

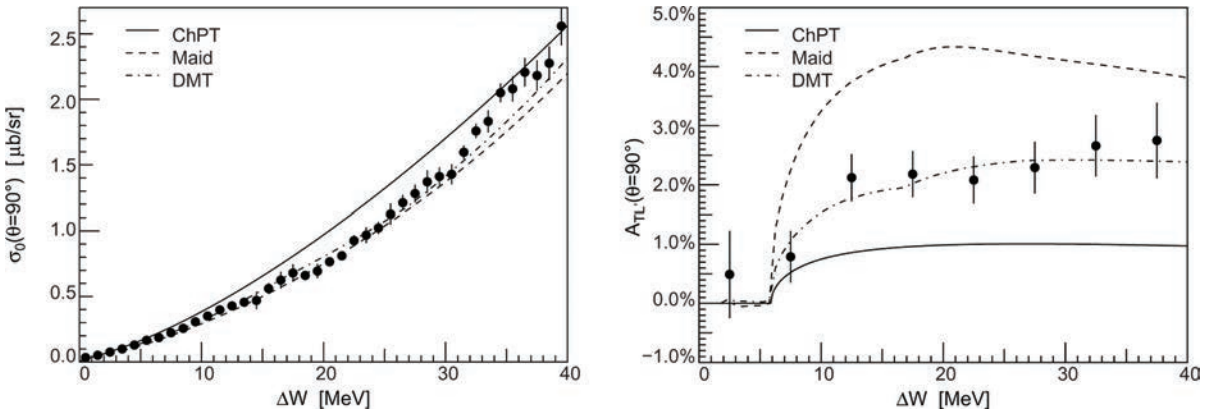

Figure 1.7: π^0 electroproduction unpolarized differential cross section $\sigma_0 = \sigma_T + \epsilon_l \sigma_L$ (left) and TL' asymmetry (right) at $Q^2 = 0.05\,(\mathrm{GeV}/c)^2$ versus ΔW. The experimental data, circles, are due to Ref. [61], ChPT [36, 37], DMT model [39] and MAID model [38] values are denoted on the graphs.

The agreement with ChPT (to be more precise with HBChPT) was marginal but since the theoretically undetermined parameters (low energy constants) had been fitted to the data, the agreement could not test ChPT vigorously. The conclusion at this point was that a new experiment was needed at $Q^2 < 0.1\,(\mathrm{GeV}/c)^2$, where higher order low energy constants would not be needed and so neither the fit to experimental data. Furthermore, a very low Q^2 data can make connection with photoproduction where ChPT is glorious. Let us remind ourselves that $Q^2 = 0$ means *real* photon, which corresponds to photoproduction.

Along this line of thinking, a new MAMI experiment at $Q^2 = 0.05\,(\mathrm{GeV}/c)^2$ was performed [56]. Like the first experiment, both beam and target were unpolarized. Separated virtual photon cross sections and total cross sections were measured in the same ΔW interval. The comparison with HBChPT results was surprisingly bad. Figure 1.6 show the comparisons of HBChPT [36, 37] and MAID model [38] values with experimental data. Two issues were noted: (i) there are serious disagreements between extracted multipole amplitudes from all experimental electroproduction data sets, (ii) The disagreement with electroproduction data is strongest at $Q^2 = 0.05\,(\mathrm{GeV}/c)^2$. This discrepancy is a serious problem for HBChPT, as it is due to the large p-wave multipole combination P_{23}^2, which is fixed by photoproduction data and cannot be meddled with.

A third MAMI experiment [61] with polarized beam, at the same Q^2 but for wider range of ΔW, i.e., $0\ \mathrm{MeV} \leqslant \Delta W \leqslant 40\ \mathrm{MeV}$ was carried out recently. The helicity-insensitive virtual

photon cross sections and asymmetry functions, for the first time, were measured at the angle of $\theta = 90°$. The results along with theoretical calculations from HBChPT, MAID model and DMT model [39] are shown in Fig. 1.7. The disagreement with HBChPT results is present, but interestingly the other two phenomenological models are in better agreement with experimental data at cross section level. The impressive agreement of DMT model with asymmetry data while HBChPT and MAID model take two very different paths is interesting. Another aspect of this experiment was to observe an imaginary part into the s-wave multipoles above the π^+ threshold through the asymmetry function, which is sensitive to such imaginary part. The experiment suffers from somewhat-large statistical error and in low energy bins from larger systematic errors.

The current experimental data on near threshold electroproduction is troubling for ChPT. Further precise experiments may determine the source of the problem. This takes us back to the motivation of E04-007 experiment in the introduction of this thesis. In the following chapter, we discuss the experiment and its instrumentation.

Chapter 2

Experiment E04-007 at Jefferson Lab

The noticeable discrepancy between ChPT predictions for both cross sections and asymmetries with current experimental data requires more extensive and precise measurements. To make sense of this discrepancy, new experimental data are needed for multipoles, cross sections, and TL' asymmetry.

The experiment E04-007 at Hall A of Jefferson Lab (JLab) was proposed to expand the data in quantity and precision. The experiment employed polarized electron beam with unpolarized target (which allows TL' asymmetry measurements) and covered momentum transfer of $0.056\,(\mathrm{GeV}/c)^2 \leqslant Q^2 \leqslant 0.45\,(\mathrm{GeV}/c)^2$ with invariant mass above threshold over the range of $0\,\mathrm{MeV} \leqslant \Delta W \leqslant 50\,\mathrm{MeV}$. In addition to Hall A standard equipment which will be explained in the following sections, experiment E04-007 employed the large acceptance BigBite spectrometer as the hadron arm to detect the recoiled protons. The BigBite spectrometer's 96 msr solid angle acceptance and 80% momentum acceptance allow new data with smaller systematic error. The large acceptance of the BigBite allowed us to measure the entire proton's angular distribution within just three settings. This feature improves the currently existing MAMI data [56, 61], where statistical error was larger. Furthermore, for MAMI experiments several spectrometer positions were needed to cover the necessary angular range, resulting in increased systematic errors.

The experiment will provide separated virtual photon cross sections $\sigma_0 = \sigma_T + \epsilon_L\sigma_L$, σ_{TL}, σ_{TT} and TL' asymmetry function in the span of its kinematical reach. We now discuss the components of the experimental setup.

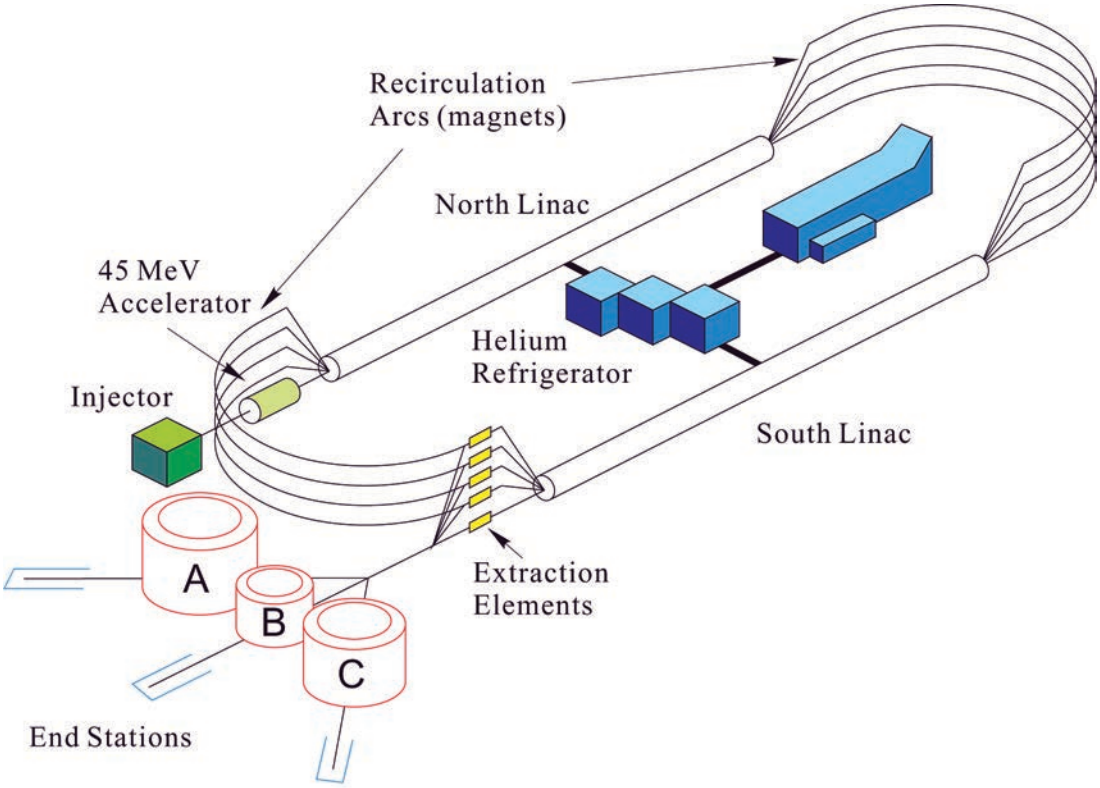

Figure 2.1: The Jefferson Lab accelerator layout.

2.1 CEBAF

The Continuous Electron Beam Accelerator Facility (CEBAF) is a medium energy electron accelerator capable of providing high quality continuous electron beams of energy up to 5.7 GeV and currents up to 200 μA.

The CEBAF has a configuration resembling a track-and-field race track consists of a polarized source, an injector, a pair of superconducting radio frequency (RF) linacs, extraction elements, and three experimental halls, A, B, and C (see Fig. 2.1).

The polarized electron beam is produced by illuminating a strained gallium arsenide (GaAs) photocathode in an injector with a 1497 MHz gain-switched diode laser, operated at 780 nm. Each hall receives a pulse of 499 MHz, or one pulse every 2 ns, and the current to three experimental halls can be controlled independently. A Mott polarimeter measures the polarization of the beam as it is produced in the injector, which is capable of producing polarization greater than 80%. The polarization angle of the electrons is set with a Wien filter so that the electrons are longitudinally polarized. The electrons acquire an energy of 56 MeV in the injector before entering the first linac.

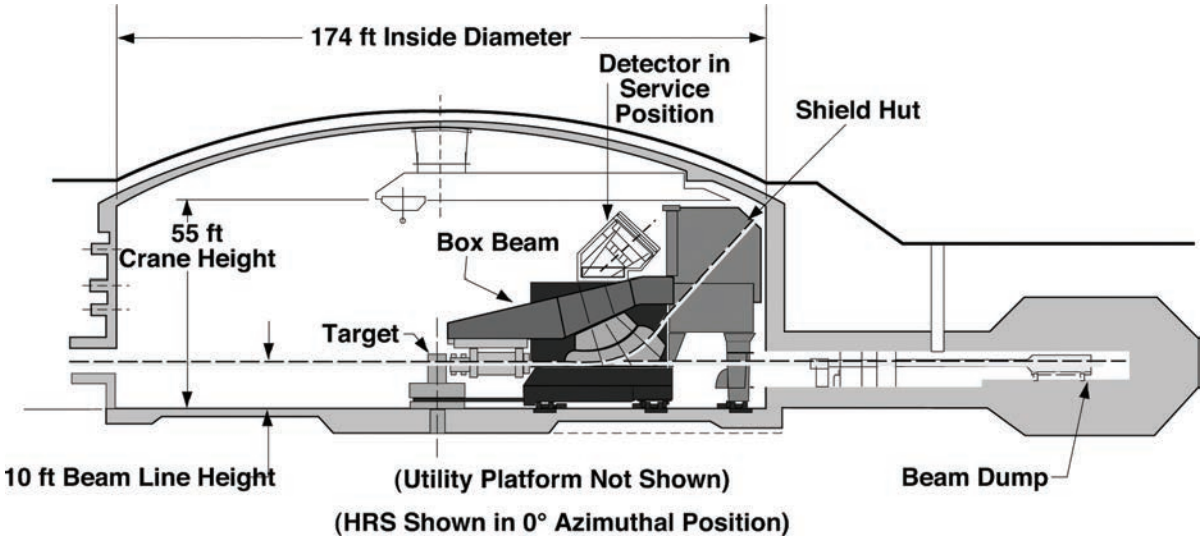

Figure 2.2: Schematic cross section of Hall A with one of the HRSs in the fictious 0° position.

Accelerated electrons are then sent into the north linear accelerator (North Linac), where they gain an additional 570 MeV before being bent in the East Arc and accelerated to 1150 MeV in the South Linac. At this point, in the lab language, the "one pass" beam can either be sent to the Extraction elements where it can be directed on the target of any of the experimental halls or recirculated through the accelerator loop to become a higher "pass" beam with the energy ramped up by 1150 MeV per pass. The beam can be recirculated up to a maximum of five passes before it is sent to any of the experimental halls. The beam pulses are separated after each linac pass by means of RF separators at the Extraction elements also known as the Beam Switch Yard.

Each linac consists of 20 superconducting cryomodules, each of which contains eight superconducting radiofrequency (RF) cavities. Liquid helium, produced at the Central Helium Liquifier (CHL), keeps the accelerating cavities at a temperature of 2 K, to maintain their superconductivity. The cavities produce field gradients of $\simeq$ 7 MeV/m [62].

2.2 Hall A

The experimental Hall A is the largest one amongst the three experimental halls at JLab. It has a circular geometry with a diameter of 53 m. A large fraction of the experimental hall is located underground and is well shielded with concrete and a thick layer of earth to contain radiation. The basic layout and geometry of Hall A is shown in Fig. 2.2 [62].

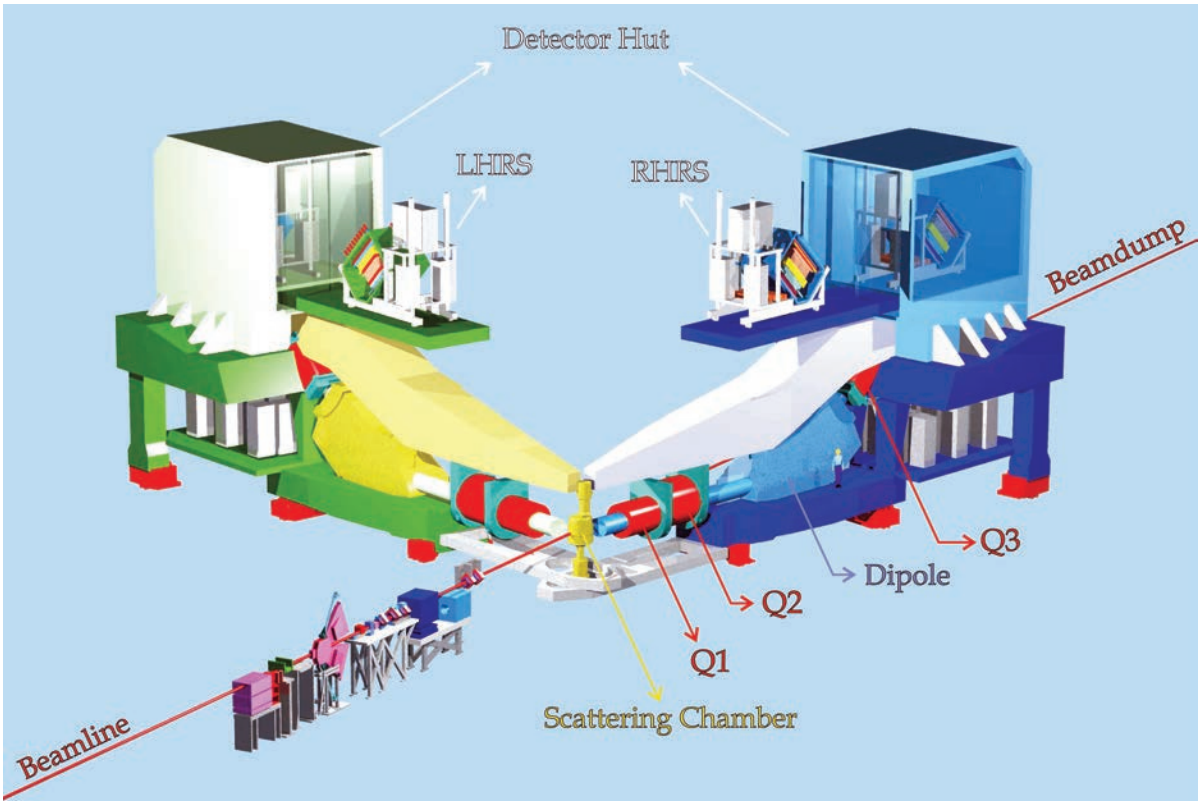

Figure 2.3: The standard apparatus in Hall A. Left and Right High Resolution Spectrometers (LHRS and RHRS) are housed inside the detector hut.

The standard Hall A apparatus consists of beamline equipment, target, and two High Resolution Spectrometers (HRSs).

At the pivot point of the two spectrometers sits the target. The electron beam is incident on the target through an evacuated beamline. There are elements along the beamline for measurements of the beam current, beam position, beam energy, and beam polarization. Those incident electrons, which do not interact with the target continue along the path of the beamline and are transported to a well shielded, isolated beam dump (see Fig. 2.3).

For the E04-007 experiment the large acceptance BigBite spectrometer was added to the standard set up. The BigBite spectrometer's capabilities (increasing the achievable count rate in the hall by a factor of 10 due to its increased angular and momentum acceptance over that of the existing pair of HRSs) complement the two HRSs in Hall A. BigBite has a solid angle acceptance of 96 msr when placed 1 m from the target. It has a horizontal acceptance of ±80 mrad (4.6°) and a vertical acceptance of ±300 mrad (17.2°).

The primary target for this experiment was a 6 cm liquid hydrogen target. Left HRS (LHRS)

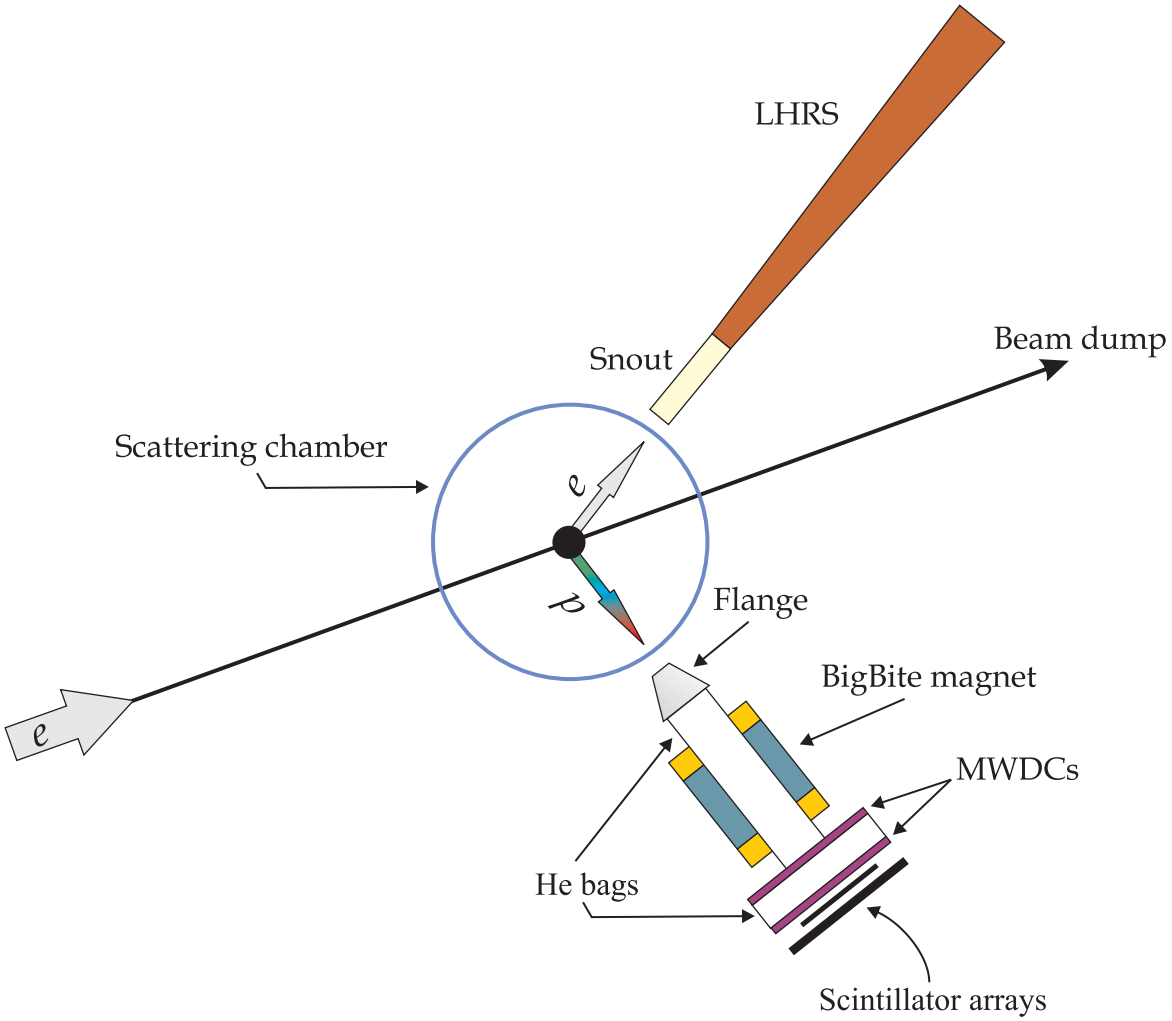

Figure 2.4: Schematic layout of the experiment E04-007.

was used as the electron arm to detect scattered electrons and BigBite spectrometer was the hadron arm to detect recoiled protons. The experiment layout is shown in Fig. 2.4. It should be mentioned that the Right HRS (RHRS) was used as luminosity monitor. The following sections detail the components of the experimental setup.

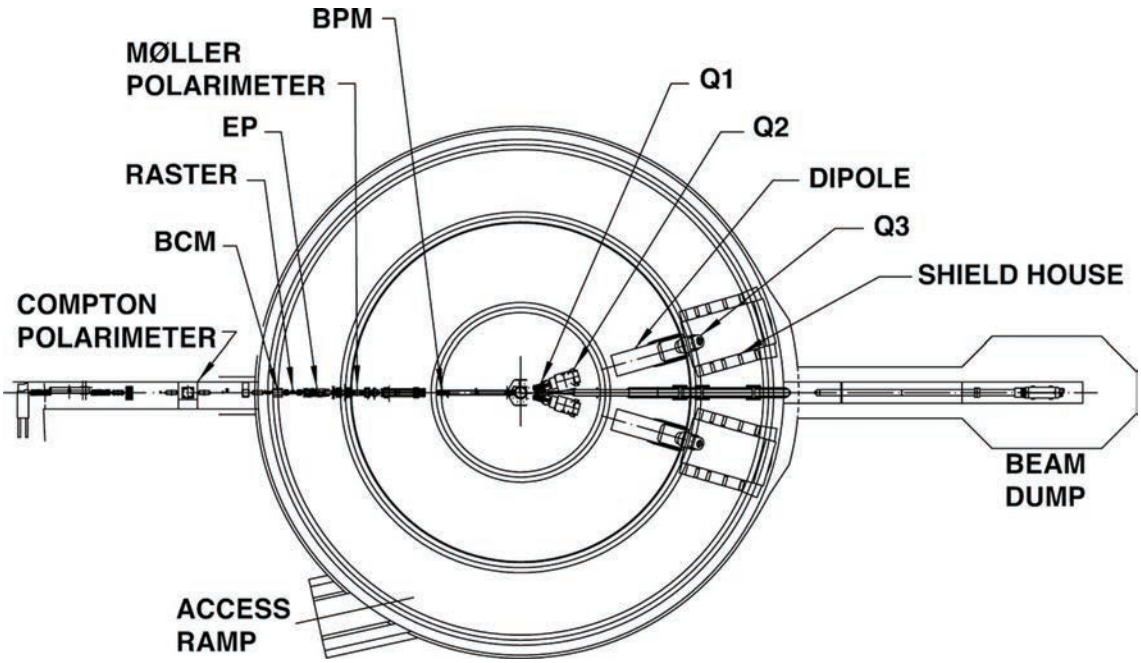

Figure 2.5: Schematic layout of the Hall A standard setup, indicating the location of the Compton and the Møller polarimeters, the raster, the ep energy measurement system, the beam current monitors (BCM) and the beam position monitors (BPM) upstream of the target. Also indicated are the locations of the components of one of the high-resolution spectrometers (Q1, Q2, dipole, Q3 and shield house) and of the beam dump and the truck access ramp. The BigBite spectrometer is not shown.

2.3 Beamline

The experiment depends on the knowledge of the beam's energy, current, and polarization to a reasonable accuracy. The hall A beamline carries the beam from the beam switch yard to the target and ends at the beam dump. Prior to the interaction at the target, the electron beam traverses several points of interest.These points correspond to the beam current and position monitoring, beam energy measurement and beam raster points (see Fig. 2.5). In the upcoming sections, we describe the components and methods needed to make these measurements along the beamline.

2.3.1 Beam Energy

The energy of the electron beam for Hall A is measured by two independent methods; the Arc method and the eP method. The Arc method is based on the beam deflection in a known

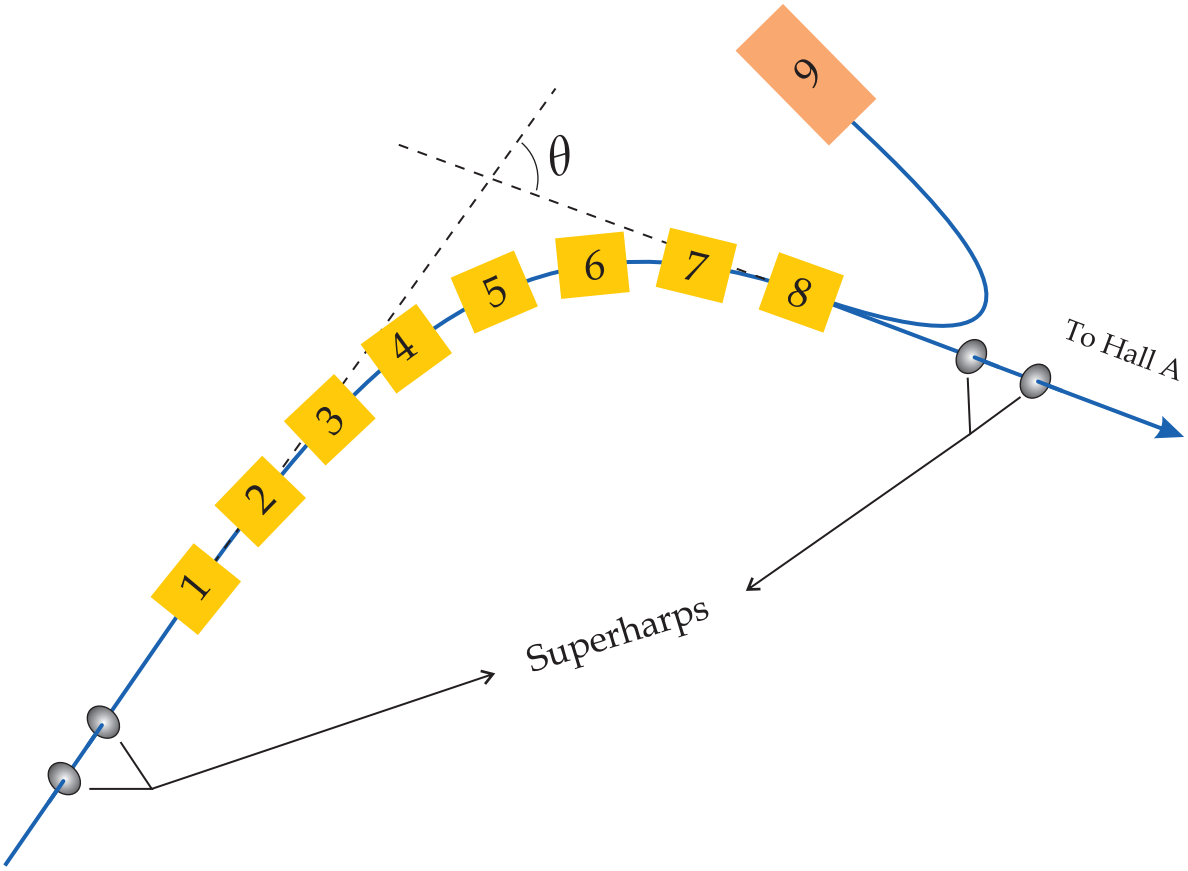

Figure 2.6: The Arc section in the Beamline.

magnetic field, and the ep method is based on elastic electron-proton scattering [62]. Both methods provide a precision of $\delta E_{\text{beam}}/E_{\text{beam}} \sim 2\times10^{-4}$. Beam energy also was supplied from the accelerator group using the *Tiefenbach* method. this method is a variation of the Arc method performed separately by the CEBAF accelerator group.

2.3.1.1 Arc Method

Through this method, the energy of the electron beam for Hall A is measured in a large arc bend just before the entrance to the experimental hall A. The arc contains eight magnets. The knowledge of the magnetic field strength of these magnets and beam's path through them allow extraction of the incident beam energy. In other words, this measurement is based on the fact that an electron takes on a circular trajectory in a constant magnetic field, where its radius depends on the magnitude of the magnetic field and the electron's momentum.

Sensitive beam position detectors (superharps) are used to monitor the position of the beam at two different locations of the bend. The information is then used to calculate the electron

energy entering the hall (see Fig. 2.6). The Arc method determines the energy of the beam by measuring the deflection of the beam in the arc section of the beamline. The nominal bend angle of the beam in the arc section is 34.3°. The measurement is made when the beam is tuned in the dispersive mode in the arc section. The momentum of the beam, p, is then related to the field integral of the eight dipoles and the net bend angle through the arc section, θ, by

$$p = k\frac{\int \mathbf{B}\cdot d\mathbf{l}}{\theta},$$

with p in GeV/c, θ in radians, $\mathbf{B}$ in Tesla, $k = 0.299792$ GeV rad (T m c)$^{-1}$. The method consists of two simultaneous measurements, the measurement of the actual bend angle of the arc and measurement of the field integral of the bending element (eight dipoles in the arc). The actual bend angle of the arc is measured by four wire scanners (superharps), two at the upstream entrance of the arc and two at the down stream exit of the arc, and the field integral in the eight bending dipoles in the arc is measured by a ninth reference magnet located in a separate building. The ninth magnet is identical to other magnets and is powered in series with them. The superharp is moved across the beam path. When the beam strikes a wire, the particles scattering off the wire are collected by a simple ion chamber, hence the current is generated and the beam's position is recorded.

2.3.1.2 eP Method

The eP method utilizes a stand-alone device along the beamline located about 17 m upstream of the target. In this method, the beam energy, E, is determined by measuring the scattered electron angle, θ_e, and the recoil proton angle, θ_p, in the $^1H(e,e'p)$ elastic reaction according to the kinematic formula:

$$E = M_p\frac{\cos\theta_e + \sin\theta_e\big/\tan\theta_p - 1}{1-\cos\theta_p} + O\left(m_e^2\big/E^2\right),$$

in which M_p and m_e denote the masses of the proton and electron, respectively. The schematic diagram of the eP system is shown in Fig. 2.7. A detailed description for the eP measurement can be found in Ref. [62]. Repeated measurements of the beam energy with both Arc and eP methods show good agreement with each other within their respective uncertainties $\left(\leqslant 3\times10^{-4}\right)$ except around 3 GeV. It is guessed that the discrepancy at 3 GeV originates from the systematic error related to the position misalignment of one particular microstrip detector in the eP setup [62].

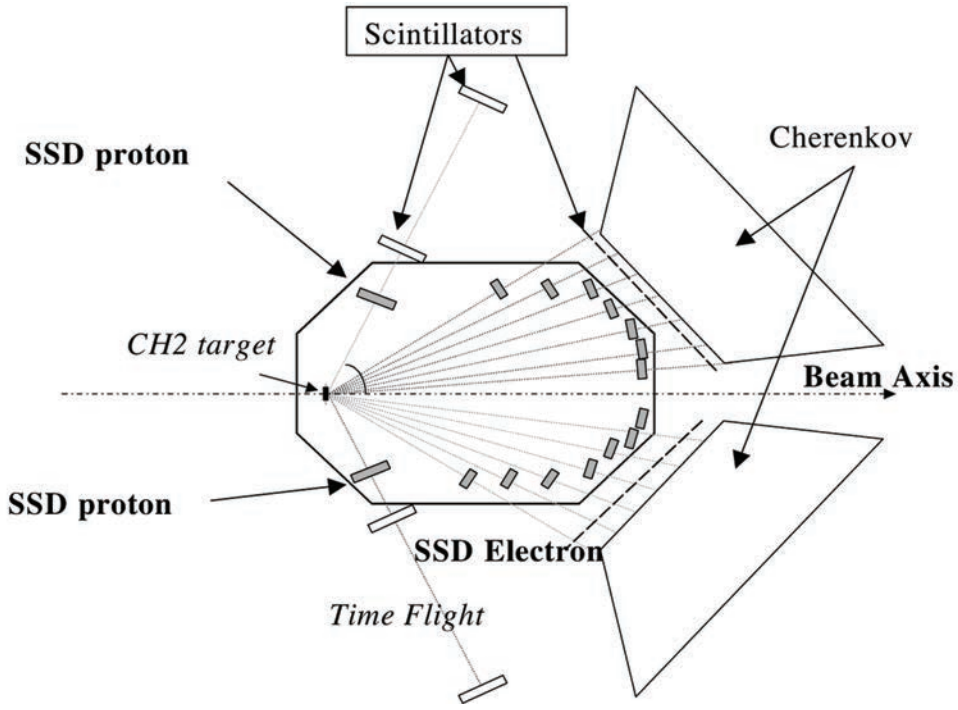

Figure 2.7: Schematic layout of the eP energy measurement system, showing the arrangement of its components, the polyethylene (CH2) target, the Cherenkov detector, the silicon-strip detectors (SSD) for protons and electrons and the scintillator detectors, used for time of flight measurements.

2.3.2 Beam Position Monitor

Two Beam Position Monitors (BPMs), called BPMA and BPMB, located 7.524 m and 1.286 m upstream of the target are employed to determine the position and direction of the beam at the target. The standard difference-over-sum technique is used to determine the relative position of the beam to within 100 μm for a current above 1 μA.

A BPM consists of four antennas surrounding the beamline in a diamond configuration. As it passes through the BPM system, the electron beam induces a signal in each antenna which can be measured and used to accurately reconstruct its position. The BPMs are complemented by the presence of a set of wire scanners known as superharps. The absolute position of the beam can be determined from BPMs by calibrating them with respect to wire scanners, which are located adjacent to each BPM (7.353 m and 1.122 m upstream of the target). The wire scanners are regularly surveyed absolutely with respect to the Hall A coordinates. At present, the results agree with respect to each other at the level of 200 μm. The position information from BPMs, which has to be calibrated separately to the scanner data, can be recorded in two

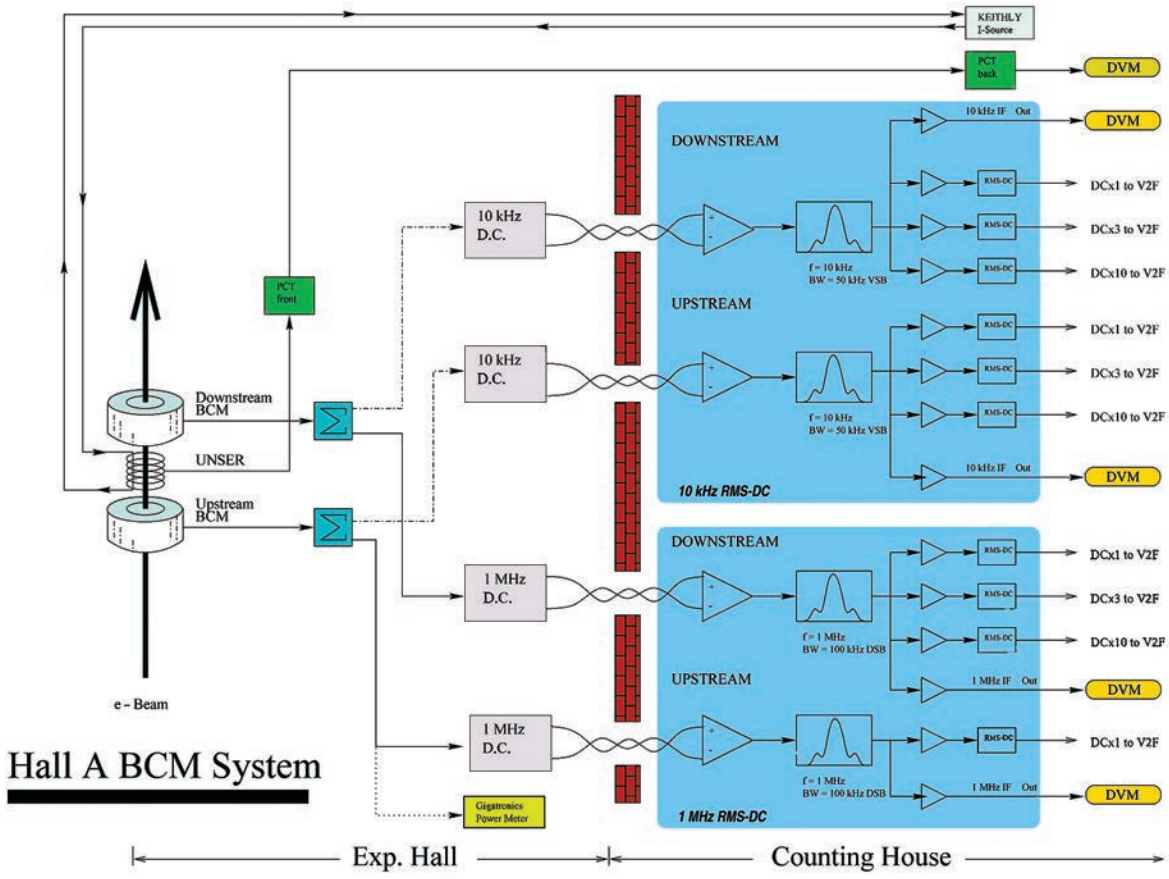

Figure 2.8: Schematic of the Hall A beam current measurement system.

different ways:

1. The average position recorded by the BPMs over 0.3 s is logged into EPICS (The Experimental Physics and Industrial Control System) database with 1 Hz updating frequency and injected asynchronously into the data stream every three to four seconds.

2. Event-by-event information from BPMs is recorded in the CODA data stream from each of the eight (2×4) BPM antennas.

2.3.3 Beam Current Monitors

The Beam Current Monitor (BCM) is designed for stable, low noise, non-intercepting beam current measurements. It consists of an Unser monitor, two RF cavities, the electronics, and a data acquisition system. The two cylindrically shaped RF beam cavity monitors (BCMs), which are 15.48 cm in diameter and 15.24 cm in length, and the Unser monitor are enclosed in

a box to improve magnetic shielding and temperature stabilization. The box is located 25 m upstream of the target. Inside Hall A, it can be recognized as a grey object on the stands, about 2 m downstream from where the beam enters the hall. The DC 200 down-converters and the Unser front end electronics are located in Hall A. The temperature controller, the Unser back end electronics and its calibration current source, cavity's RF unit (housing the RMS-to-DC converter board) and all multi-meters,VME crate and computers are located in Hall A control room.

The Unser monitor is a Parametric Current Transformer designed for non-destructive beam current measurement and provides an absolute reference. The monitor is calibrated by passing a known current through a wire inside the beam pipe and has a nominal output of 4 mV/μA. It requires extensive magnetic shielding and temperature stabilization to reduce noise and zero drift. The two resonant RF cavity monitors on either side of the Unser Monitor are stainless steel cylindrical high Q (~3000) waveguides which are tuned to the frequency of the beam (1497 Hz) [63].

When the cavities are tuned to the frequency of the beam, their output voltage levels are proportional to the beam current. The output signal is amplified and split into two parts. One part is sent to a high-precision digital AC voltmeter, which provides a measurement of the beam current averaged over 1 s periods, i.e., each second this device provides a digital output which represents the RMS average of the input signal during that second. The resulting number is proportional to the beam charge accumulated during the corresponding second (or, equivalently, the average beam current for that second). The other part of the signal is converted by an RMS-to-DC converter into an analog DC voltage level, which is then converted to a frequency signal by a Voltage-To-Frequency (VTOF) converter. This frequency signal is sent to scalers, gated by the start and the end of each run, providing a measurement of the beam charge accumulated during the runs. The schematic diagram of the BCM system is shown in Fig. 2.8.

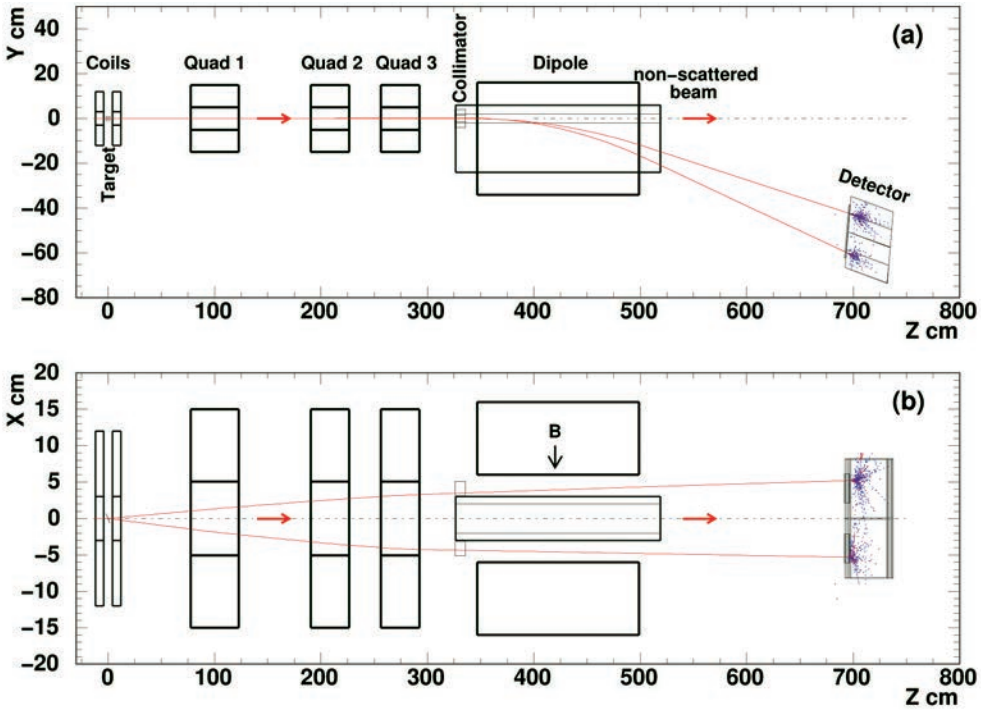

Figure 2.9: Schematic layout of the Møller polarimeter (a) and (b) present side view and top view respectively. The trajectories displayed belong to a simulated event of Møller scattering at $\theta_{CM} = 80°$ and $\phi_{CM} = 0°$, at a beam energy of 4 GeV.

2.3.4 Beam Polarization

Various experiments in Hall A use the polarized electron beam, with a typical beam polarization of 75-85%. In order to measure the polarization of the electron beam delivered to the hall, the beamline is equipped with two polarimeters, Møller polarimeter and Compton polarimeter, whose functions are partly overlapping and partly complimentary. During the E04-007 experiment Hall C experiment had the priority for most of the run period. For the one pass running Hall A received 67% polarization (this was determined by two Møller measurements which will be discussed in the following section). For the two pass running, Hall A received 87.5% polarized beam.

2.3.4.1 Møller polarimeter

A Møller polarimeter exploits the process of Møller scattering of polarized electrons off polarized atomic electrons in a magnetized foil $\vec{e} + \vec{e} \rightarrow e + e$. The reaction cross-section depends on

the beam polarization P^B, and target polarization P^T, as

$$\sigma_M \propto \left[1 + \sum_{i=X,Y,Z} A_{ii} P_i^B P_i^T\right],$$

where $i = \mathrm{X}, Y, Z$ defines the orthogonal projections of the polarizations. The analyzing power A_{ii} depend on the scattering angle in the CM frame, θ_{CM}. Assuming that the beam direction is along the Z-axis, Y-axis is normal to the scattering plane, so that the scattering happens in the ZX plane, then the analyzing powers are defined as:

$$\begin{aligned} A_{ZZ} &= -\frac{\sin^2\theta_{\mathrm{CM}}\left(7 + \cos^2\theta_{\mathrm{CM}}\right)}{\left(3 + \cos^2\theta_{\mathrm{CM}}\right)^2}, \\ A_{XX} &= -\frac{\sin^4\theta_{\mathrm{CM}}}{\left(3 + \cos^2\theta_{\mathrm{CM}}\right)^2}, \\ A_{YY} &= -A_{XX}. \end{aligned}$$

The analyzing power A_{ZZ} has its maximum value, $A_{ZZ,\mathrm{max}} = 7/9$, at $\theta_{\mathrm{CM}} = 90°$. A beam polarization transverse to the scattering plane also leads to an asymmetry, and a lower analyzing power, i.e., $A_{XX,\mathrm{max}} = A_{ZZ,\mathrm{max}}/7$. The main purpose of the polarimeter is to measure the longitudinal component of the beam polarization. The Møller scattering events are produced using a ferromagnetic foil target, where its electrons are polarized in a magnetic field of about 24 mT. The target foil can be tilted at various angles with respect to the beamline, providing a target polarization with both longitudinal and transverse components. The beam polarization may have a transverse component, which would couple to the transverse component of the target polarization. To cancel the contribution of the transverse component, the asymmetry is measured at two complimentary target angles, 20° and 160°, and the average is taken.

The Møller scattering events are detected using a magnetic spectrometer as shown in Fig. 2.9. The spectrometer consists of a series of three quadrupoles and a dipole. The detector system consists of scintillators and two lead- glass calorimeter modules that are split into two arms to detect the two scattered electrons in coincidence.

The polarization measurement with Møller polarimeter is invasive. It can be used at beam energies from 0.8 to 6 GeV. It has to use a low beam current of about 0.5 μA. One measurement typically takes an hour, providing a statistical accuracy of about 0.2%. The systematic error is dominated by the knowledge of the foil target polarization, which has a 3% relative uncertainty [62].

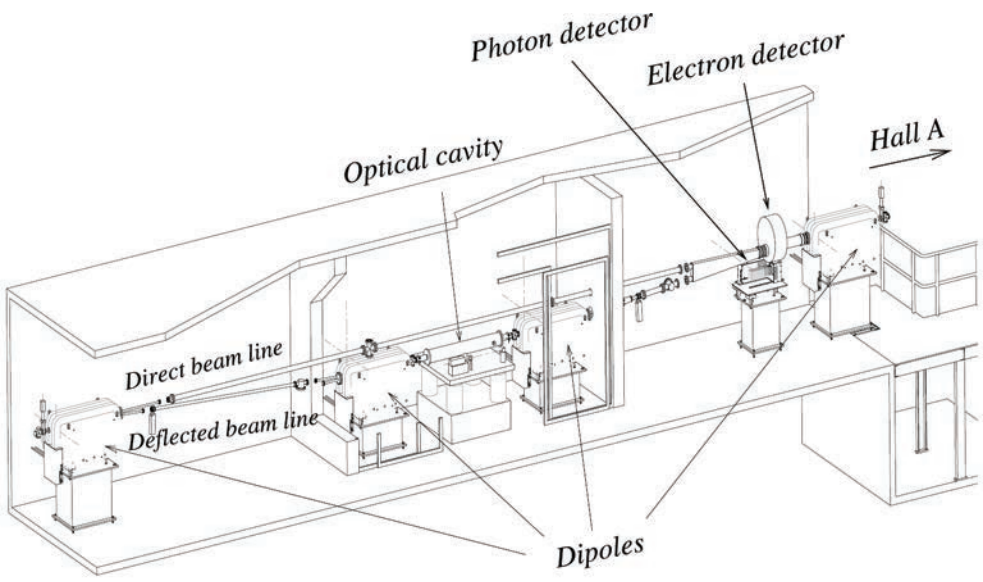

Figure 2.10: Schematic lay-out of the Compton polarimeter displaying the four dipoles of the chicane, the optical cavity and the photon and electron detector.

2.3.4.2 Compton polarimeter

The Compton polarimeter utilizes the process of Compton scattering. It is designed to measure the beam polarization concurrently with experiments running in the hall. The polarization is extracted from the measurement of the counting rate asymmetry for opposite beam helicities in the scattering of circularly polarized photons off the electron beam.

The Compton polarimeter is positioned at the entrance of hall A and consists of a magnetic chicane, polarized photon source, an electromagnetic calorimeter, and an electron detector (see Fig. 2.10). The electron beam is deflected vertically by the four dipoles magnets in the chicane so that the beam crosses the photon beam at the Compton interaction point. The interaction point is located at the center of the chicane. A 230 mW CW Nd:YAG laser beam (λ = 1064 mm) is the primary source of the photons, and a 85 cm long resonant Fabry-Pérot cavity is used to amplify the photon density. The circular polarization of the laser is greater than 99% for each of the right and left photon helicity states. The circular polarization of the photon beam can be reversed using a rotatable quarter-wave plate.

After Compton scattering, the scattered electrons are detected in the silicon strip detector, and the backscattered photons are detected in the calorimeter. Electrons that did not interact exit the polarimeter and reach the target in the hall. A fast front-end electronics and data-acquisition system is required to collect data at rates of up to 100 kHz. Compton events are

clearly detected by scanning the vertical position of the electron beam, varying the field in the dipoles, until both beams cross at the center of the cavity.

Once the position of the electron beam has been tuned to maximize the Compton interaction rate, data are recorded for both photon beam polarizations. Single electrons, single photons or coincidences can trigger the data acquisition. The background contribution is measured during periods of laser beam off. A background/signal ratio of 0.05 has been routinely obtained. The energy of the scattered particles is reconstructed from the position of the electrons in the micro-strip planes and the amount of light collected in the photon calorimeter. During the E04-007 experiment, the Compton polarimeter was out of commission due to upgrades. Therefore no Compton measurement was performed during the experiment.

2.3.5 Beam helicity

Knowing the helicity state of the beam pulse is crucial to any asymmetry experiment. For the E04-007 experiment, determining helicity state was achieved employing Hall A helicity electronics. The helicity circuitry in Hall A receives its input, i.e., a helicity-plus signal, from the injector. The helicity signal from injector has a pulse width of 33 ms. There are two modes, toggle and pseudorandom, which can be used for the pulse sequence. In the toggle mode, the helicity pulse lengths are fixed and the helicity alternates every 33 ms. The signal frequency is therefore 30 Hz for both helicity-plus (H+) and helicity-minus (H-). In the pseudorandom mode, the helicity alternates with a random probability for each 33 ms. This means one may get two successive pulses of the same helicity, generating a single double length pulse. The net effect of pseudorandom mode is to reduce the frequency by 25%, so the scaler measures 25 Hz for H+ and 25 Hz for H-.

The helicity circuitry in Hall A takes the input signal from injector, generates its complementary (negative) signal and sends both signals down to the detector stacks. Circuitry in each arm then generate a shortened pulse for each helicity, chops off the leading edge to allow the helicity to stabilize, and sends these stabilized pulses to the detector's DAQ system. The data from the detector DAQ and scalers are all gated by these helicity signals. There is a variable helicity assigned to all events in the detector data stream. Events gated by H+ pulses have helicity = +1 and those by H- pulses have helicity = −1.

During the experiment helicity gated scalers read BCM to record accumulated charge for each beam helicity. This allows us to correct for the false asymmetry arising from the beam

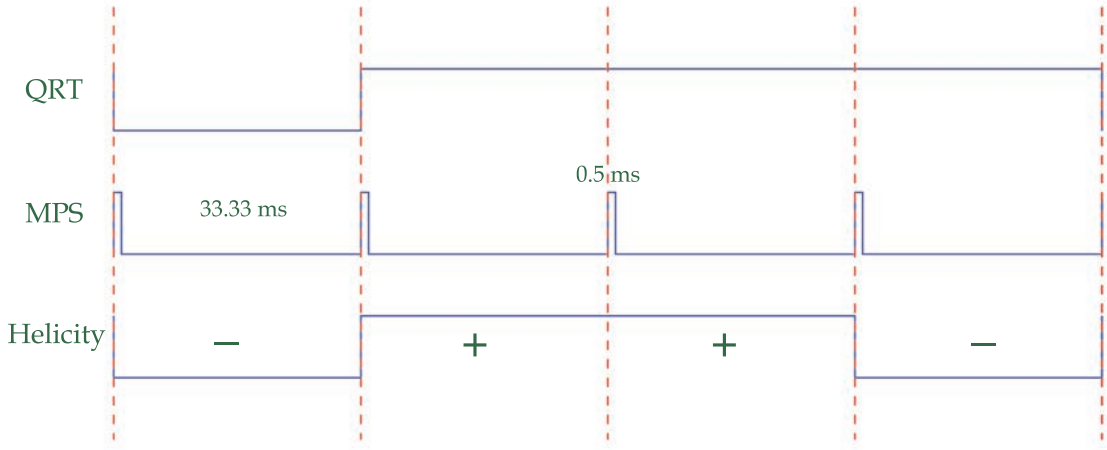

Figure 2.11: Beam helicity sequence used during experiment E04-007.

charge asymmetry

$$A_Q = \frac{Q^+ - Q^-}{Q^+ + Q^-} \, . \tag{2.1}$$

The sign of each helicity state also depends on the configuration of the insertable half-wave plate (IHWP). The status of the IHWP can be either *IN* if it is inserted or *OUT* if retracted. The relative sign of the beam polarization is determined from the Møller measurements. If during the Møller measurement the IHWP is *IN*, then the sign from Møller should be multiplied by -1. The IHWP was *IN* throughout the π^0 experiment.

Two Møller measurements were taken during the experiment. The measured polarization was approximately 67%. The Møller measurements results can be found in Appendix E.

For experiment E04-007, the "G0 helicity scheme" [64] was used. The schematic is shown in Fig. 2.11. The characteristics of this scheme are:

- The macro-pulse trigger (MPS signal at 30 Hz) is used as a gate to define periods when the helicity is valid.
- The helicity sequence has a quartet structure (either $+--+$ or $-++-$). The helicity of the first MPS gate is chosen pseudorandomly.
- Quartet trigger (QRT) defines when a new random sequence of four helicity states has begun.
- The helicity information sent to the halls are typically delayed by eight MPS.

Figure 2.12: Target ladder.

There exist a blank-off period of approximately 0.5 ms for each 33.3 ms gate period. This blank-off is the time during which the Pockel cell at the source is changing and settling.

2.4 Target

This section will explain the target system, cryogenic and solid targets, used for the E04-007 experiment. The quartet sequence provides for exact cancellation of linear drifts over the sequence's timescale. All three bits (helicity, QRT, gate) are read in the datastream for each event, and the copies are sent to scalers which have input registers. The delay of the helicity reporting breaks any correlations with the helicity of the event by suppressing crosstalk.

The cryogenic target system was mounted inside the scattering chamber along with the subsystems for cooling, gas handling, temperature and pressure monitoring, target control and motion, with an attached calibration and solid target ladder. The cryogenic target had three independent target loops: a liquid hydrogen (LH_2) loop, a liquid deuterium (LD_2) loop and a gaseous helium loop. Each of the two liquid loops had two cylindrical aluminium target cells mounted on the target ladder. The cells were 25.4 mm in diameter and 6 cm long. The cryogenic targets and the thickness of the sidewalls, entrance and exit windows are listed in

Table 2.1: Cryogenic target cells specifications.

Cryo-target	Enterance window (mm)	Exit window (mm)	Wall thikness (mm)
6 cm H_2 + coll.	0.074±0.012	0.118±0.015	0.136±0.006
6 cm H_2	0.119±0.003	0.142±0.006	0.142±0.010
6 cm D_2 + coll.	0.103±0.002	0.137±0.006	0.126±0.010
6 cm D_2	0.100±0.002	0.133±0.006	0.115± 0.004
6 cm He	0.116±0.003	0.139±0.004	0.138± 0.006
15 cm He	0.217±0.003	0.122±0.008	No data

Table 2.1.

As it can be seen in Table 2.1, the target had very thin entrance and exit windows for the beam and thin side walls to minimize the energy loss of the low energy protons recoiling out of the target. The first target cell in LH_2 and LD_2 loops (first and third cells in Fig. 2.12) were equipped with brass collimators. Collimators were used to shield the detectors from the cell windows.

The gaseous helium targets were spare cells and used as backup cells during the experiment. As shown in the Fig. 2.12, the targets were arranged in a vertical stack, which can be moved from one position to another under the remote control to select different targets.

The target ladder also had a "dummy" target (beneath the cryogenic targets, consisting of two thin pieces of aluminium, separated by empty space), which was used to measure contributions from the target cell. This dummy target was made of Al 6061-T6. The upstream foil had a thickness of 0.1176 ± 0.001 gr/cm^2 and the downstream foil had a thickness of 0.1186 ± 0.001 gr/cm^2.

The solid target ladder had five target positions occupied by a Carbon (^{12}C) target with hole, a regular Carbon (^{12}C) target, a Tantalum (Ta) target, a Beryllium-Oxide (BeO) target, and an empty target with no target foil. Table 2.2 lists the thickness of each target.

In general, solid targets were used for optics and calibration. In particular, solid Ta and C targets were used for beam energy determination using elastic scattering and C with hole was for beam alignment.

All target positions were surveyed before and after experiments. The motion during vacuum pump-down and cool-down was monitored and corrected in the position determination.

Table 2.2: Solid target ladder thickness and specifications.

Target	Material	Average thickness (g/cm^2)	Purity
Carbon with hole	^{12}C	N/A	N/A
Carbon	^{12}C	0.08388±0.00012	99.95%
Tantalum	Ta	0.0180±0.0001	99.5%
Berillium Oxide	BeO	0.149±0.001	99.0%
Empty	N/A	N/A	N/A

The targets were usually centred to about 1 mm with a typical position precision of about 0.5 mm. The target used for the production data taking was a 6 cm liquid hydrogen.

2.5 High Resolution Spectrometer

The core of the Hall A equipment is a pair of superconducting High Resolution Spectrometers, which are nominally identical in terms of their magnetic properties. Each of the two spectrometers consists of three $cos2\theta$ quadrupoles ($Q_1, Q_2,$ andQ_3) and one dipole (D). These superconducting magnets are arranged in the (QQDQ) configuration to deflect particles into their focal planes. The eight superconducting magnets, two dipoles and six quadrupoles, each have independent cryogenic controls and reservoirs. The cryogenic system which maintains the magnet systems is common to all eight magnets and the cryo-target. The cryogenic system is fed from a helium refrigerator called the End Station Refrigerator (ESR) dedicated to the cooling of the magnets and targets in all JLab end stations [62]. A schematic view of one of the Hall A HRSs is shown in Fig. 2.13.

At the focal planes the particles, dispersed vertically in momentum, are detected in the detector package. The momentum of the electron that reaches the detector package is determined by the magnetic field in the dipole magnet. The spectrometer's central momentum is related to the magnetic field of the dipole by

$$p_0 = \sum_{i=1}^{3} \Gamma_i B_0^i,$$

where Γ_i are the spectrometer constants and B_0 is the dipole magnetic field. These constants

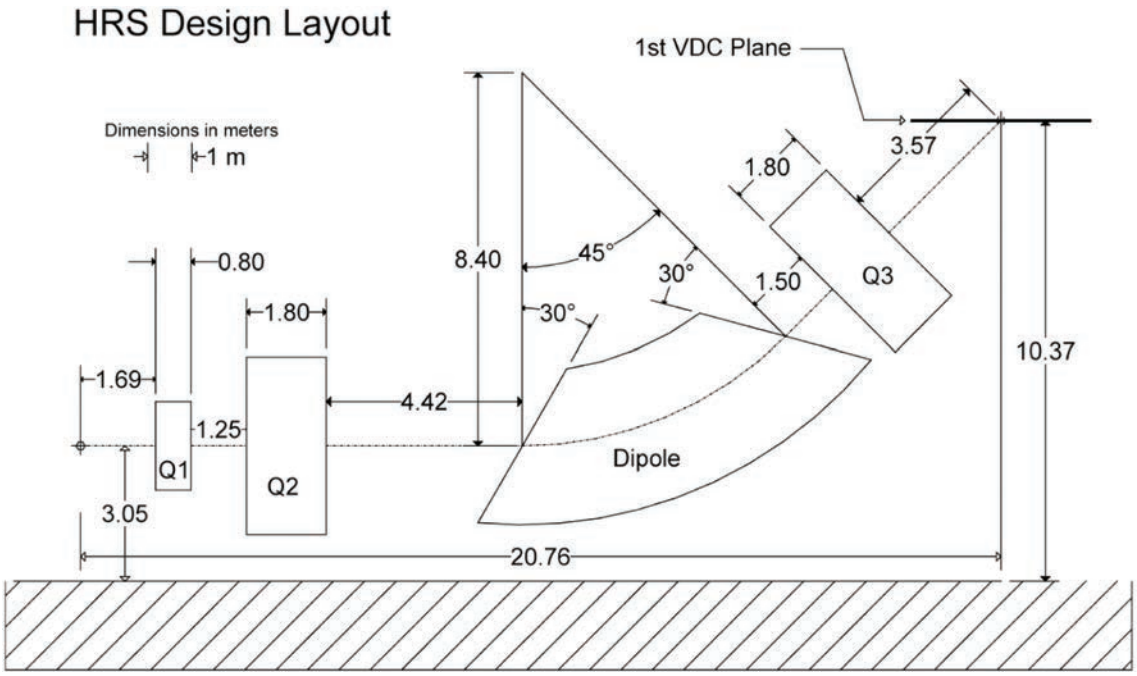

Figure 2.13: Schematic layout of HRS. The geometrical configuration of the dipole and three quadrupoles as well as the location of the first VDC tracking detector are shown.

were determined for both HRSs over their full momentum range.The constants for the spectrometers are given in Table 2.3 .

The optical length of the spectrometer is 23.4 meters, with a 45° vertical bending angle at the dipole. The spectrometers have a momentum range from 0.3 to 4.0 GeV/c . The momentum acceptance is about 9%. The HRSs provide a momentum resolution better than 1×10^{-4} and a horizontal angular resolution of better than 0.5 mrad at the maximum central momentum of 4 GeV/c [62]. The spectrometers can be moved clockwise or counter-clockwise about Hall A's pivot, where the target is located. The left spectrometer has minimum and maximum central angle of 12.5° and 144.5° respectively, with respect to the beamline. The minimum and maximum central angles for the right spectrometer are 12.5° and 130.5°, respectively. It should be noted that either spectrometer can be configured for the detection of either type of particles by simply switching the field polarity of the magnets. The general characteristics of the HRSs are summarized in Table 2.4. More details on spectrometer design can be found in [62].

Table 2.3: The spectrometer constant coefficients for LHRS and RHRS.

	Γ_1 (MeV T^{-1})	Γ_2 (MeV T^{-2})	Γ_3 (MeV T^{-3})
LHRS	2702 ± 1	0	-1.6 ± 0.4
RHRS	2698 ± 1	0	-1.6 ± 0.4

2.5.1 Detector Package

The detector package and all data-acquisition (DAQ) electronics are housed within a shielding hut (SH) to protect the detector against radiation background. The SH is equipped with air conditioning and fire suppression systems. The detector package for each of the two spectrometers is located on the top of the HRS structure, immediately after Q_3 (Fig. 2.3).

The HRSs are designed to perform various functions in the characterization of charged particles passing through the spectrometer. They can be tailored to the needs of individual experiments. The detector packages of both spectrometers are almost identical, except for a slight difference in the gas Cerenkov and the lead-glass counter. Each detector package is composed of

- A pair of Vertical Drift Chambers (VDCs), for precise tracking information (position and direction),
- Scintillator planes to provide a trigger to activate the data acquisition electronics, and precise timing for time-of-flight measurement,
- Cerenkov detectors (aerogel and gas) and lead-glass shower counter, both for particle identification (PID).

2.5.1.1 Vertical Drift Chambers

Particle tracking information for each HRS is provided by a pair of Vertical Drift Chambers separated by about 335 mm. Each VDC is composed of two wire planes in a standard UV configuration. The wires of each successive plane are perpendicular to one another, and lie in the laboratory horizontal plane. The wires of each plane are oriented at an angle of 45° with respect to the nominal particle trajectory as shown in Fig. 2.14. There are a total of 368 sense wires in each plane, spaced 4.24 mm apart [62].

Table 2.4: The design characteristic of the Hall A high resolution spectrometers; the resolution values are for the full width half maximum.

Configuration	QQDQ vertical bend
Bending angle	45°
Optical length	23.4 m
Momentum range	0.3 - 4.0 GeV/c
Momentum acceptance	$-4.5\% < \delta p/p < +4.5\%$
Momentum resolution	1×10^{-4}
Dispersion at the focus (D)	12.4 m
Radial linear magnification (M)	-2.5
D/M	5.0
Angular range of left HRS	$12.5° - 150°$
Angular range of right HRS	$12.5° - 130°$
Angular acceptance (Horizontal)	±30 mrad
Angular acceptance (Vertical)	±60 mrad
Angular resolution (Horizontal)	0.5 mrad
Angular resolution (Vertical)	1.0 mrad
Solid angle at $\delta p/p = 0$, $y_0 = 0$	6 msr
Transverse length acceptance	±5 cm
Transverse position resolution	1 mm

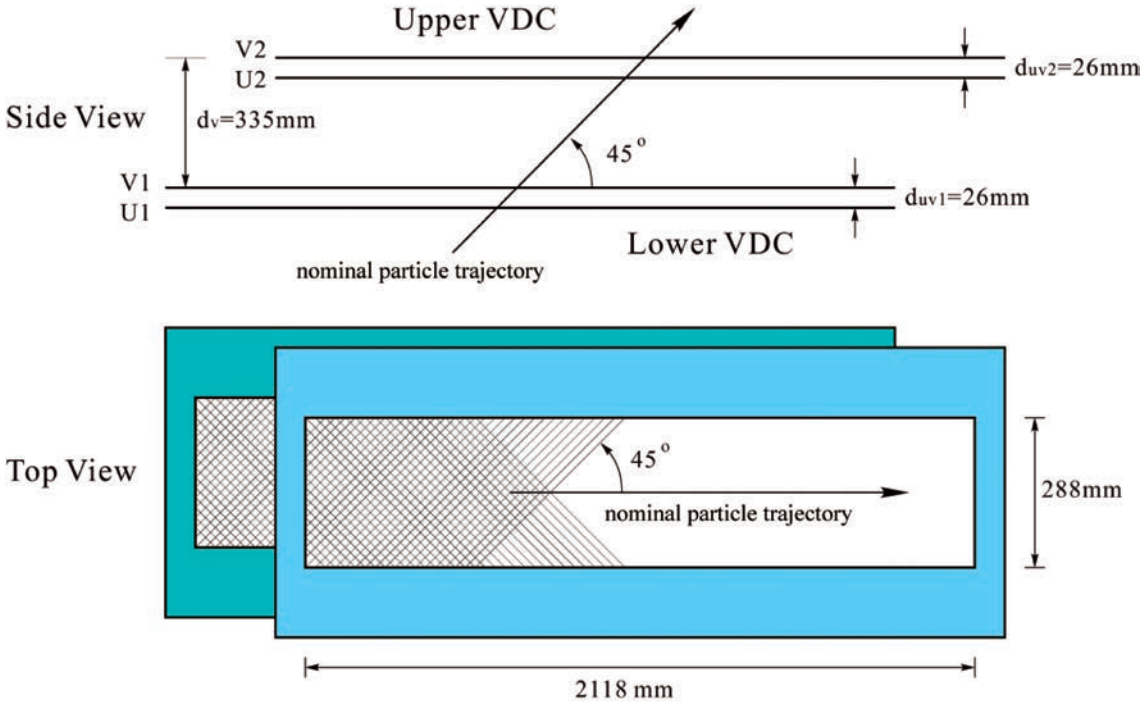

Figure 2.14: Schematic lay-out of a pair of Vertical Drift Chambers for one HRS (not to scale).

The VDCs are operated with their cathode planes at about −4 kV and the wires at ground with a gas mixture of argon (Ar, 62%) and ethane (C_2H_6, 38%). The charged particles produce ionization in the chamber gas when passing through the VDCs. The ionization electrons accelerate toward the wires along the path of the least time (geodetic path). The fired wires are read out with Time-to-Digital Converters (TDCs) operating in common stop mode. In this configuration, a smaller TDC signal corresponds to a larger drift time.

Using drift velocity[1] and time shift constants, the distance from the track to fired wire is precisely reconstructed. The position and direction of the track is then determined using a straight line fit. In the focal plane the position resolution, $\sigma_{x(y)}$, is about 100μm, and the angular resolution, $\sigma_{\theta(\phi)}$, is 0.5 mrad [62].

[1]Drift velocity is determined by parametrization and is approximately 50μm/ns.

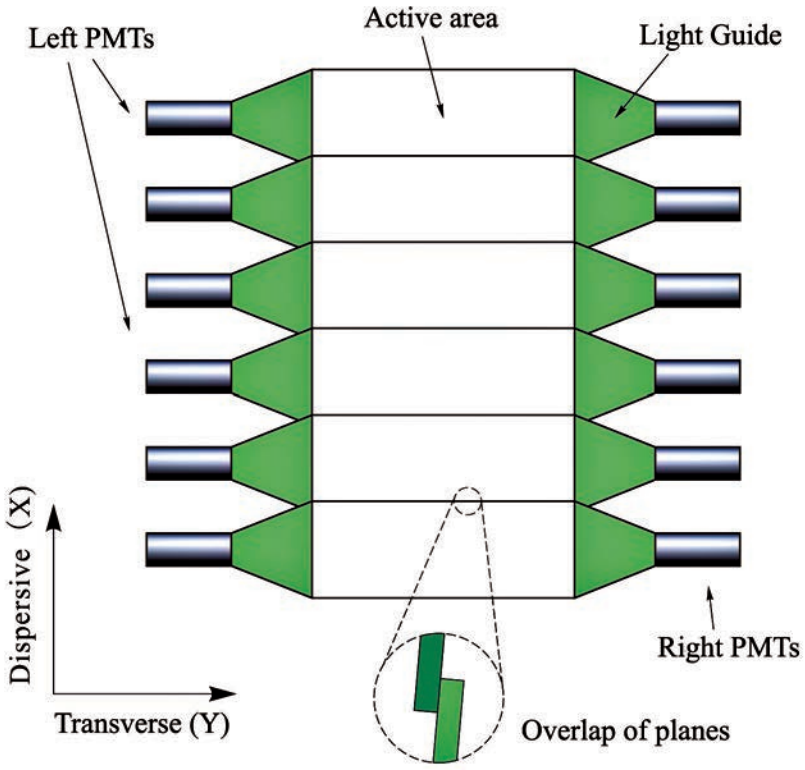

Figure 2.15: Layout of Scintillator Counters.

2.5.1.2 Scintillators

There are two planes of trigger scintillators S1 and S2 in each spectrometer. S1 is located about 1.5 meters away from the center of the first VDC plane. The S2 is about 2 meters away from S1. Each plane is composed of six overlapping paddles made of thin plastic scintillator (5 mm thick BC408). Each scintillator paddle is viewed by two photomultiplier Tubes (PMT) (Burle 8575), one at each end. The edges of two adjacent paddles overlap to avoid gaps between the paddles (see Fig. 2.15).

The scintillators are mainly used to generate triggers for the data acquisition system. The time resolution for each plane is about 0.30 ns [62]. The scintillators can also be used for particle identification by measuring the time-of-flight between the S1 and S2 planes.

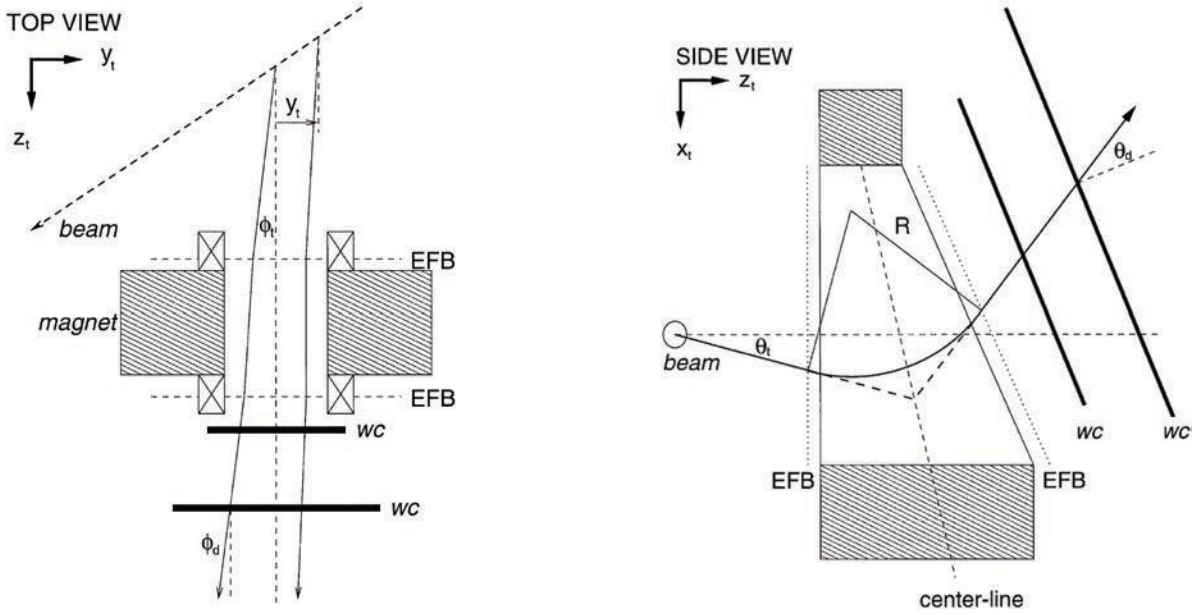

Figure 2.16: View of the non-dispersive plane (left) and dispersive plane (right) of the BigBite spectrometer. The dotted lines indicate the Effective Field Boundaries (EBF), and WC indicates the positoin of the Wire Chambers. The indexes d and t in θ and ϕ angles represent detector and target coordinates respectively.

2.6 BigBite Spectrometer

The BigBite spectrometer is a non-focusing magnetic spectrometer with a large angular and momentum acceptance. Its capabilities complement the two HRSs, which have very small acceptances but very good resolution. The HRSs can detect particles very precisely over a small kinematic range. BigBite, on the other hand, can cover a broad range of kinematics in a single setting, which is important when studying interactions for which cross sections are small. The BigBite spectrometer consists of

- A dipole magnet with a maximum magnetic field of 1.2 Tesla.
- Two sets of multi-wire drift chambers behind the magnet.
- The trigger planes, E and ΔE, consisting of segmented plastic scintillator bars.

BigBite has a solid angle acceptance of approximately 96 msr when placed 1 m from the target and its large acceptance allows detection of particles over a momentum ranging from 0.2 GeV/c to over 2.0 GeV/c in a single setting. BigBite has a horizontal acceptance of ±80

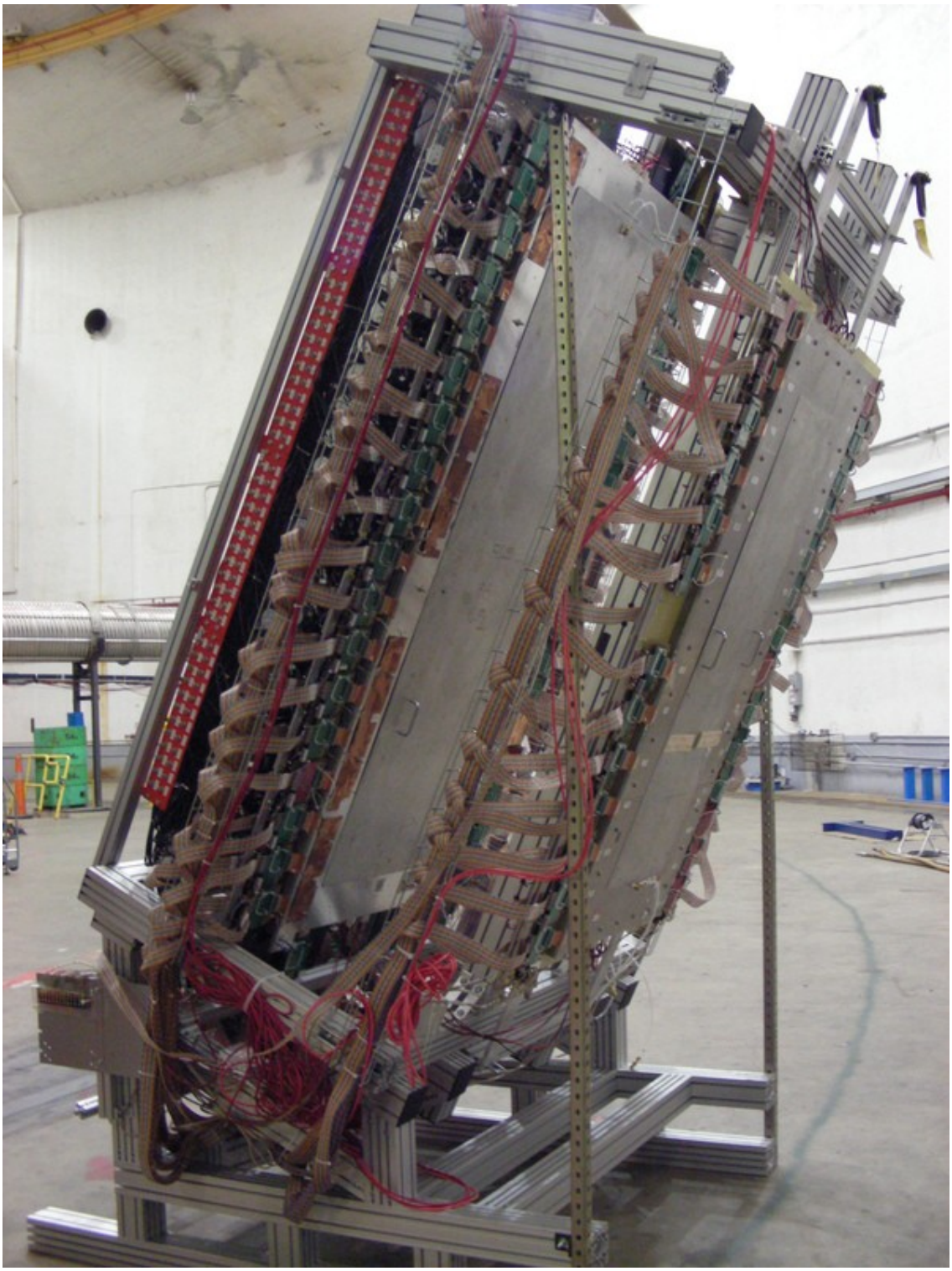

Figure 2.17: BigBite spectrometer's detector package.

Table 2.5: The general characteristic of the Hall A BigBite spectrometers.

Magnet	H-shaped dipole
Maximum magnetic field	1.2 T
Momentum range	0.2 - 2.0 GeV/c
Momentum resolution ($\delta p/p$)	1×10^{-2}
Solid angle acceptance	96 msr
Angular acceptance (Horizontal)	±80 mrad
Angular acceptance (Vertical)	±300 mrad
Angular resolution (Horizontal)	4 mrad
Angular resolution (Vertical)	4 mrad

mrad (±4.6°) and a vertical acceptance of ±300 mrad (±17.2°). The Multi-Wire Drift Chambers (MWDCs) allow for precise track reconstruction. Tracing the track through the magnetic field to the target yields the position of the scattering vertex and the size and direction of the momentum vector of the scattered particle at the target position (see Fig. 2.16).

The BigBite detector package for experiment E04-007 is shown in Fig. 2.17. The general characteristics of the BigBite spectrometer are summarized in Table 2.5 and the components of BigBite spectrometer will be discussed in the sections that follow.

2.6.1 Magnet

The magnet (originally designed for the internal target facility at NIKHEF) is an H-shaped dipole with a gap of 25 cm (see Fig. 2.18). The entrance face is perpendicular to the central trajectory while the exit face makes a 5° angle with it. This enhances (reduces) the field integral for particles entering the upper (lower) region of the magnet, thereby making the dispersion more uniform across the acceptance of the spectrometer. At the nominal field of 0.92 T, particles with momenta of 500 MeV/c that enter along the optical axis pass through the magnet along the central trajectory and are detected at 25° above horizontal level.

Both the yoke and polar pieces of the magnet are made from low-carbon steel. The water-cooled coils were made from hollow copper pipe with outer dimensions of $13.5 \times 15\text{mm}^2$ and a bore of 9.5 mm diameter. There are a total of ten coil pancakes, each with 36 turns. The coils are not parallel to the polar piece, but are slightly tilted such that the solid angle is not

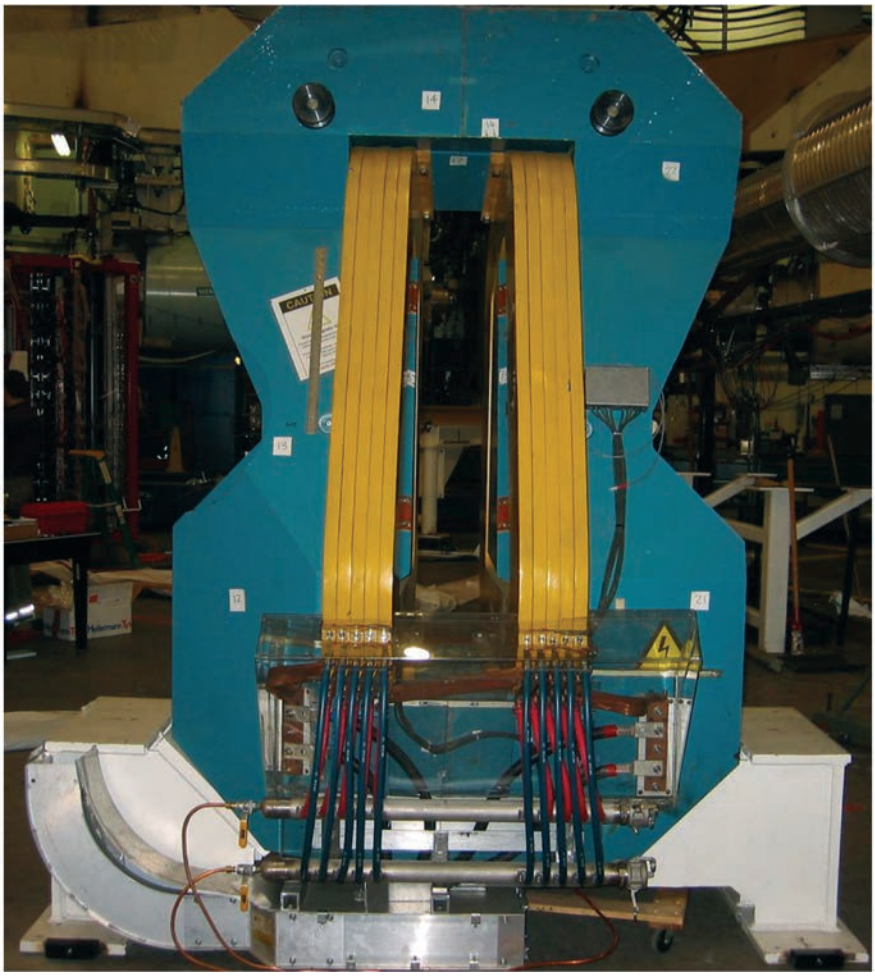

Figure 2.18: BigBite magnet in Hall A.

limited by the coils at the exit of the magnet. The 0.92 T field requires a current of 518 A. Under normal operating conditions the temperature of the coils rises to about 55° C. Each pancake is equipped with a temperature controlled switch to detect cooling problems [65].

Figure 2.19: Polyurethane balloon filled with helium provides low-density path for protons travelling from the target to the detector.

2.6.2 Helium Filled Balloons

For E04-007 experiment two helium filled balloons were used to provide low-density path for transporting low energy protons from the scattering chamber to the detectors. The balloon made of a 0.0102 cm thick polyurethane was placed in the BigBite gap (shown in Fig. 2.19). In fact, this helium conduit with polyurethane sides allowed the protons to travel from the target through the spectrometer to the wire chambers. The second similar balloon occupied the space between the two wire chambers. The sides of the second balloon was made of a 0.00254 cm thick aluminized mylar instead of polyurethane.

2.6.3 Multi-Wire Drift Chambers

A pair of Multi-Wire Drift Chambers were used in the experiment E04-007. These multi-wire drift chambers were designed to provide high rate capabilities, high resolution, as well as unambiguous track reconstruction to provide information on the track of the recoiled protons. The chambers operate in a high-rate background environment (up to 40 MHz at the location

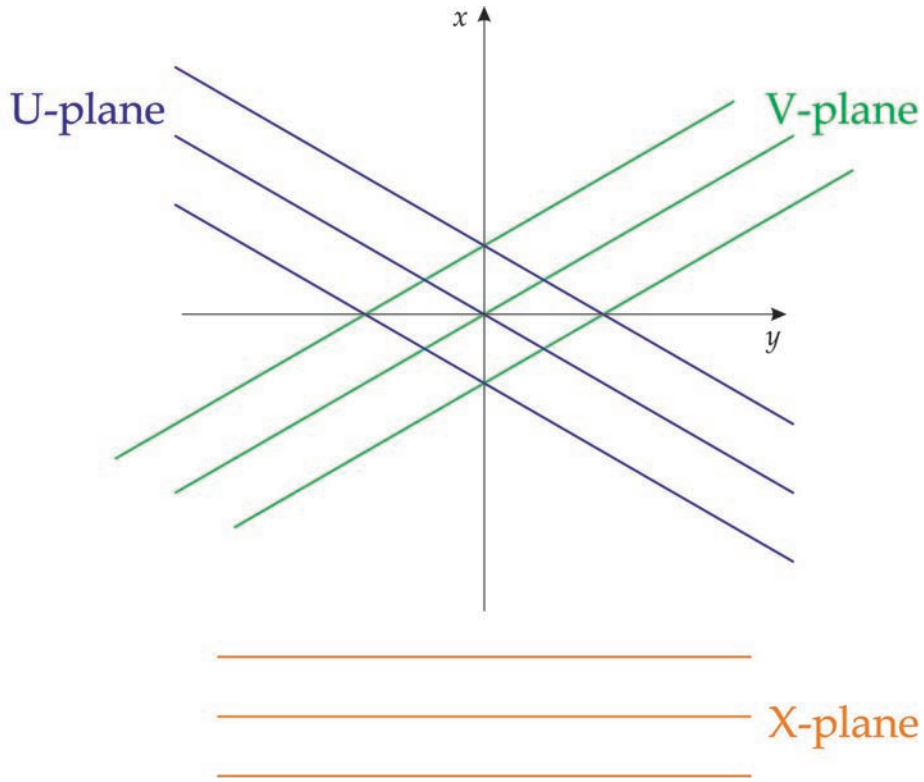

Figure 2.20: Orientation of the wires in the wire chambers.

of the first chamber) while providing a good spatial resolution. They are able to detect high energy electrons as well as low energy hadrons.

The MWDCs tracking system is composed of two separate drift chambers, which are spaced about 777 mm apart (see Fig. 2.17). Each chamber consists of six planes of parallel wires,each plane sandwiched between two high voltage cathode foils, and the whole plane assembly enclosed in a gas-tight frame. Chamber operates with a mixture of 50% Argon and 50% ethane at just above atmospheric pressure. The active area of the smaller chamber is 140 cm in the dispersive (x) direction $\times$ 35cm in the non-dispersive (y) direction and the active area of the larger chamber is 200 cm (x) $\times$ 50 cm (y).[2]

Each chamber has wires in three different directions to precisely measure track coordinates and angles in both x and y directions. The V(U) wires are at an angle of 60°(−60°) relative to the x-axis, while the X wires are perpendicular to the x-axis. The configuration of planes and

[2]By convention, the direction of increasing x is taken to be the direction of increasing momentum (dispersive direction), in other words, towards the ground (since the paths of particles with higher momentum are bent less by the BigBite magnet), the z axis is taken to point perpendicular to the wire planes in the direction of the particle tracks, and the y axis is taken so that the $\hat{x}, \hat{y}, \hat{z}$ axes form a right handed orthogonal coordinate system.

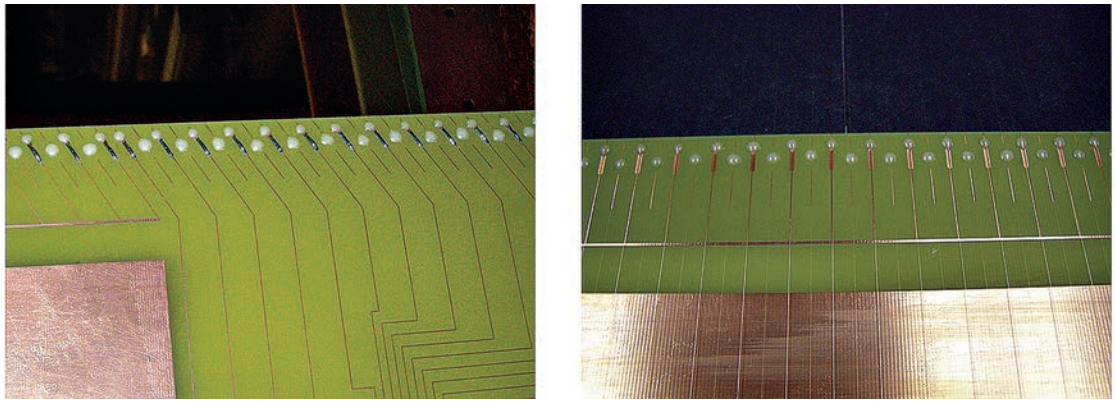

Figure 2.21: Orientation of wires in (U)V-plane (left) and X-plane (right).

wires for both chambers is shown in Fig. C.3. Each MWDC has six wire-planes, two in each orientation (U, V, X) i.e., U, U', V, V', X, X'.

The wires are alternating field (cathode) and signal (anode) wires separated by 0.5 cm (see Fig. 2.21).

The field wires are 90μm diameter copper-beryllium and the signal wires are 25μm diameter gold-plated tungsten. The signal wires are sense wires, which register hits. The field wires shape the electric field in a way to optimize the electron's drift toward the anode wire. Fig. 2.22 illustrates shape of the electric field around the signal wires. There are 4104 wires (2052 signal wires and 2052 field wires) in the BigBite wire chambers. The cathode planes are 12μm-thick double-sided copper-plated mylar. The copper layer on each side of the cathode foils has a thickness of 0.1200μm. The wires in the second plane of each pair (U', V', X') are shifted by 5 mm relative to the first plane so that the signal wires of the second plane overlay the field wires of the first plane. Figure 2.23 shows construction of MWDCs in pictures. Details on MWDC is elaborated in Appendix C.

For track reconstruction the measured drift times are used to determine the point at which a track crosses a given plane. However, the distance depends not only on time but on track angle. The distance from the track to the signal wire is known from the measured time required for the drift electrons to reach the wire. However, the track could have crossed the plane on either side of the wire from the same distance away. Arranging the wires with a 5 mm relative shift within each plane pair allows to resolve this left-right ambiguity of the track intercept.

The narrow anode to cathode gap of 3 mm allows us to minimize the chamber thickness to reduce multiple scattering of low energy hadrons. This makes these chambers suitable to be used for the E04-007 experiment, where BigBite was used to detect low energy protons.

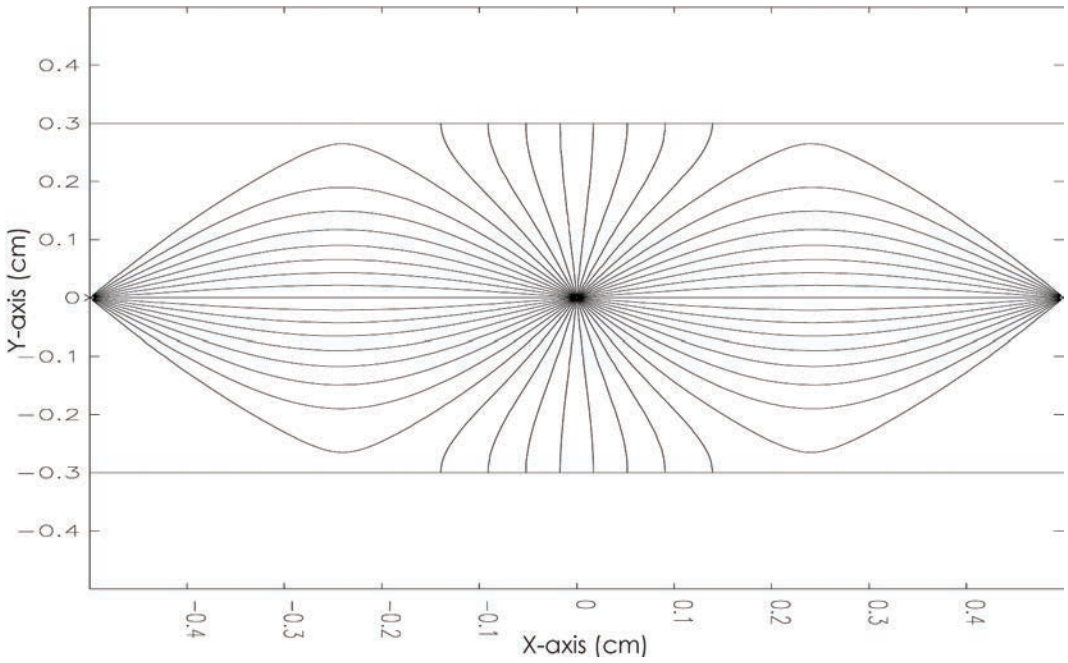

Figure 2.22: Electric field lines inside MWDCs. The signal wire, located at the origin, is held at a higher potential (ground) than the cathode film and field wires. Field lines start from the signal wire vertically to the cathode planes and horizontally to the field wires.

2.6.4 Scintillators

The scintillation detector is one of the widely used detection devices in particle physics. It makes use of the fact that certain materials when struck by an energetic particle or radiation emit a small flash of light, i.e., scintillation. A typical scintillator counter consists of a scintilllating material which is optically coupled to a photomultiplier tube (PMT) via a light guide.

There are six types of scintillator materials; organic crystals, organic liquids, plastic, inorganic crystals, gases and glasses [66]. In E04-007 experiment plastic scintillators were utilized, which are probably the most widely used of the organic detectors. They typically have density of ~ 1.0 gr/cm^3 and an index of refraction ~ 1.58.

A scintillator signal is capable of providing a variety of information such as the time that a particle hits the detector and the energy deposited by the particle.

Scintillation detectors are fast instruments in the sense that their response and recovery times are short, i.e., the time difference between two events and the time lost waiting for the scintillator to recover can be obtained with very good precision. The fast response makes the scintillation detectors useful for timing and triggering information.

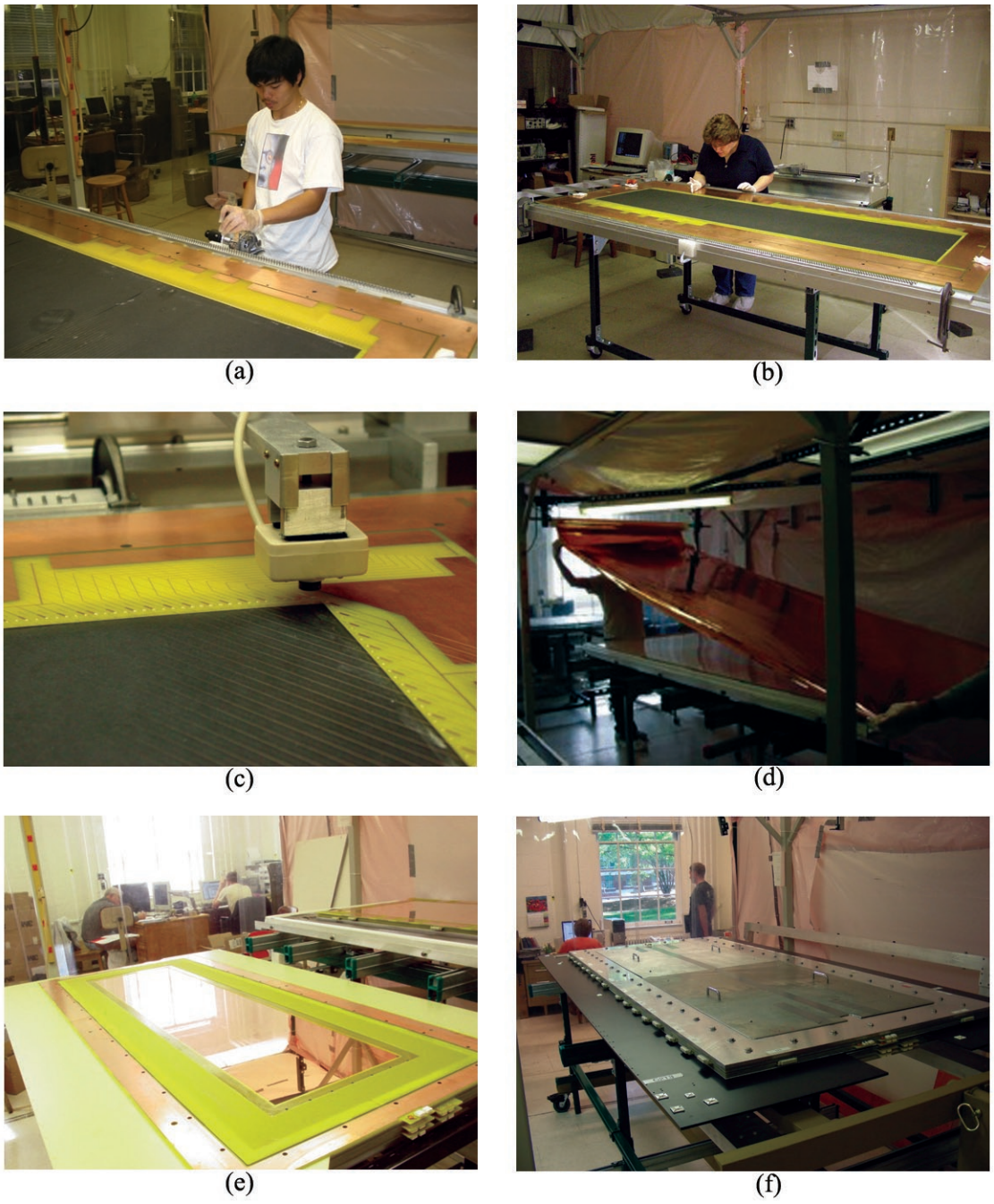

Figure 2.23: MWDC construction: (a) Stringing wires, (b) Securing wires, (c) Wire position measurement, (d) Stretching cathode planes, (e) Assembled wire-planes and cathode-planes, (f) completed chamber.

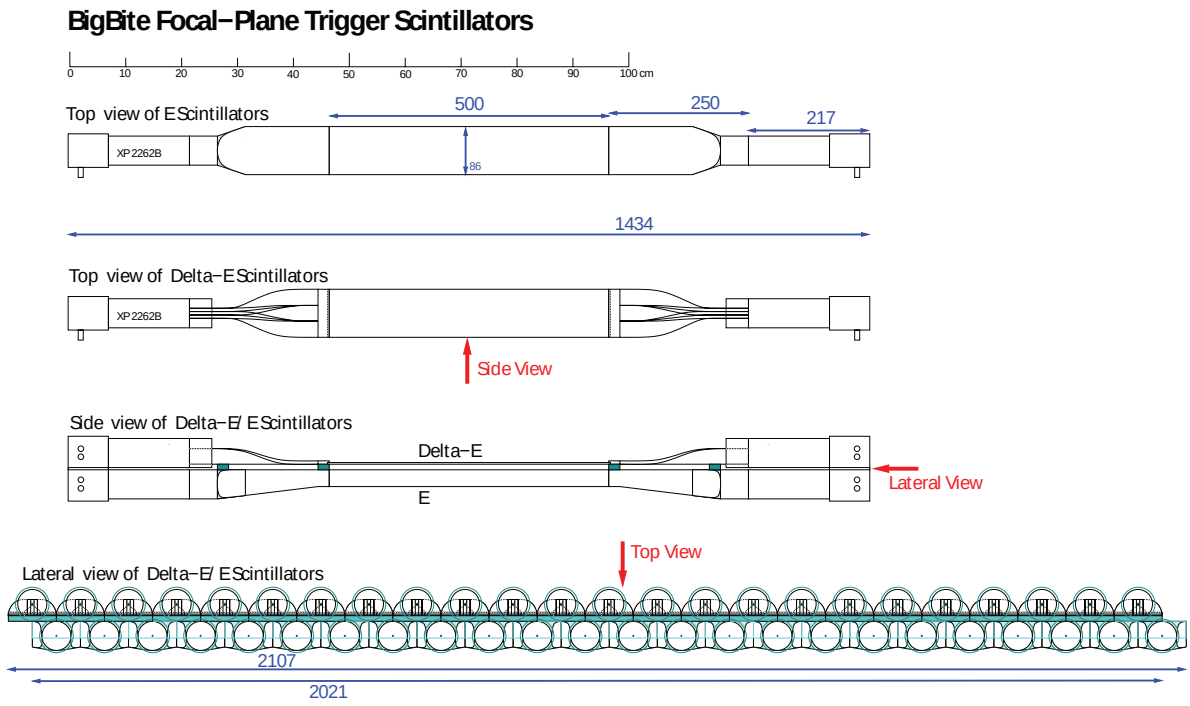

Figure 2.24: Trigger Scintillator planes for BigBite spectrometer.

Scintillation detectors are sensitive to energy. Above a certain minimum energy, scintillators behave in a near linear fashion with respect to the energy deposited, i.e., the light output of a scintillator is directly proportional to the excitation energy (the amplitude of the produced signal in first approximation is proportional to the energy deposited).

The BigBite scintillation detector formed the BigBite trigger for E04-007 experiment. The trigger planes consisted of two planes, ΔE (3 mm thick) and E (30 mm thick), of segmented plastic scintillator bars coupled to PMTs on both ends. Each trigger plane had 24 scintillator bars and each bar covered an area of 500×86 mm^2 (see Fig. 2.24). The scintillator bars in the E-trigger plane overlapped those of the ΔE plane, so that the trigger plane was effectively divided into 48 sectors. The scintillator planes were used for fast triggering and particle identification.

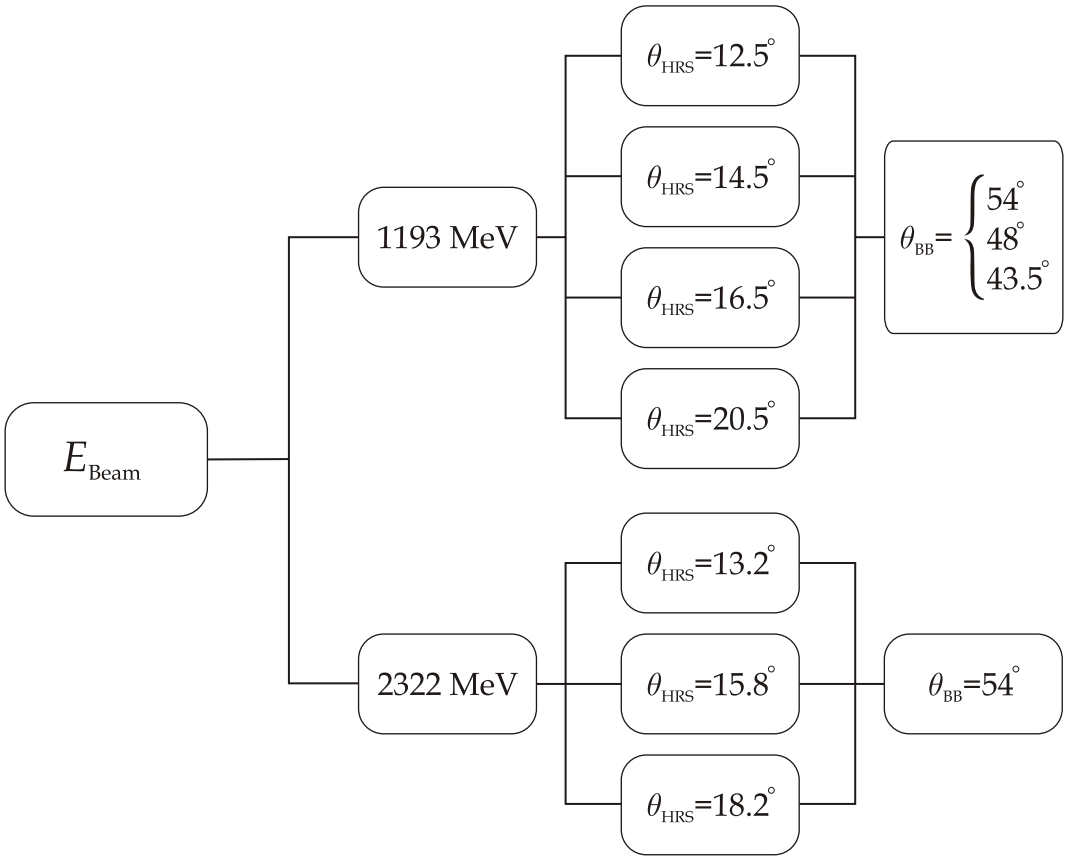

Figure 2.25: BigBite spectrometer (BB) and High Resolution Spectrometer (HRS) angle combinations for all kinematics in E04-007 experiment.

2.7 Experiment Kinematics

For experiment E04-007 data were collected with polarized electron beams at energies of 1193 MeV and 2322 MeV. The electrons were scattered off a cryogenic hydrogen target. The protons recoiled in a narrow cone and were detected in the BigBite spectrometer and the scattered electrons were detected in LHRS.

The 1193 MeV beam energy data were taken with HRS spectrometer at angles ranging from 12.5 to 20.5 degrees and BigBite ranging from 43.5 to 54 degrees. The accumulated charge summed over all these conditions was 4.818 Coulombs. Data were taken at 2322 MeV with HRS spectrometer at angles ranging from 13.2 to 18.2 degrees and BigBite at 54 degrees. These data corresponds to a total accumulated charge of 0.868 Coulombs. The set up is summarized in Fig. 2.25.

The details of the experiment kinematics and data selection will be discussed in Chapter 3.

Chapter 3

Data Acquisition and Analysis

Data for E04-007 experiment were taken in a 37 day period starting at the beginning of April, 2008. Sixteen different configurations of HRS (electron arm) and BigBite spectrometer (hadron arm) enabled data collection for seven different kinematics. The kinematics were labelled from A to Q. The kinematical set up is summarized in Table 3.1. It should be mentioned that the kinematics M and P were for calibration, i.e., no production data were taken for these settings.

In order to extract the relevant physical quantities, signal events need to be separated from background events. To qualify as a signal event, an event has to pass several selection criteria. This chapter describes the process of data acquisition and data analysis used to extract asymmetry, $A_{TL'}$, for the threshold π^0 electroproduction. The data analysis for threshold π^0 electroproduction cross section calculation is ongoing and will be discussed elsewhere [67].

3.1 Data Acquisition

The data acquisition was handled by the CODA (CEBAF Online Data Acquisition) software package, which is the standard data acquisition system developed by the Data Acquisition group for use at Jefferson Lab. It provides software tools for monitoring, accumulating, and recording data taken during experiment. Data for each run were written directly to disk and consisted of three types of information:

- Detector information read by the ADCs and TDCs: The trigger supervisor and Read Out Controllers (ROCs) handle the event-by-event retrieval of data recorded from the detectors.

Table 3.1: Summary of all kinematics

Q^2 (GeV/c)^2	Kinematics	E_{Beam} (MeV)	θ_{HRS} (deg.)	θ_{BB} (deg.)
0.056	D	1193	12.5	-54.0
	E			-48.0
	L			-43.5
0.076	C	1193	14.5	-54.0
	F			-48.0
	K			-43.5
0.097	B	1193	16.5	-54.0
	G			-48.0
	J			-43.5
0.146	A	1193	20.5	-54.0
	H			-48.0
	I			-43.5
0.251	N	2323	13.2	-54.0
0.349	O	2323	15.8	-54.0
0.428	M	1193	35.5	-54.0
0.450	Q	2323	18.2	-54.0
0.747	P	2323	23.6	-54.0

- Scalar information: Scalers provide information such as rates, current and charge accumulation.

- Information from EPICS (The Experimental Physics and Industrial Control System) database: The EPICS database provides real-time, slow varying information about the accelerator and target such as target temperature and pressure.

The hardware elements of CODA include commercial front-end Fastbus and VME digitization devices (ADCs, TDCs, scalers), the Struck Fastbus Interface (a VME interface to Fastbus), single-board VME computers, Ethernet networks, and Unix or Linux workstations. CODA also includes a number of custom software components. The most important custom software components of CODA are: the ROC which runs on the front-end electronics crates, the Event-Builder (EB) and Event-Recorder (ER) which run on a Linux workstation, and the Event-Transfer (ET) system which allows one to copy events from the ET system for online analysis without interrupting the data flow onto disk. Finally the Run Control process, a Graphical User Interface (GUI) from which users can select different experimental configurations such as trigger and target configurations, start and stop runs, as well as reset and monitor CODA components [68].

For each event which corresponds to a trigger accepted by the Trigger Supervisor (TS), data are gathered from the front-end boards by the ROC component, which buffers the data in memory and sends these buffers to the EB via the network. TS synchronizes the read-out of the front-end crates and handles the dead time logic of the system as well as interface cards for the Fastbus and VME crates, which facilitate communication between the trigger supervisor and the front-end crates. The EB assembles the events from the fragments sent by the various ROCs and passes them to the ER, which writes them to the local disk. The datafiles are subsequently written to tapes in the Mass Storage tape Silo (MSS) for long-term data storage and erased from the local disk after typically 24 hours. Using the ET system, some additional pieces of information from sources such as the control system, scalers and text files are inserted into the data stream every few seconds. In addition, the ET system is used by analysis clients to obtain a random sample of data in real-time, anywhere on the network. Block diagram of the hall A data acquisition (DAQ) is shown in Fig. 3.1.

For E04-007, EPICS provides information about the beam energy, beam position, and the state of the half-wave plate at the injector, which affects the beam helicity.

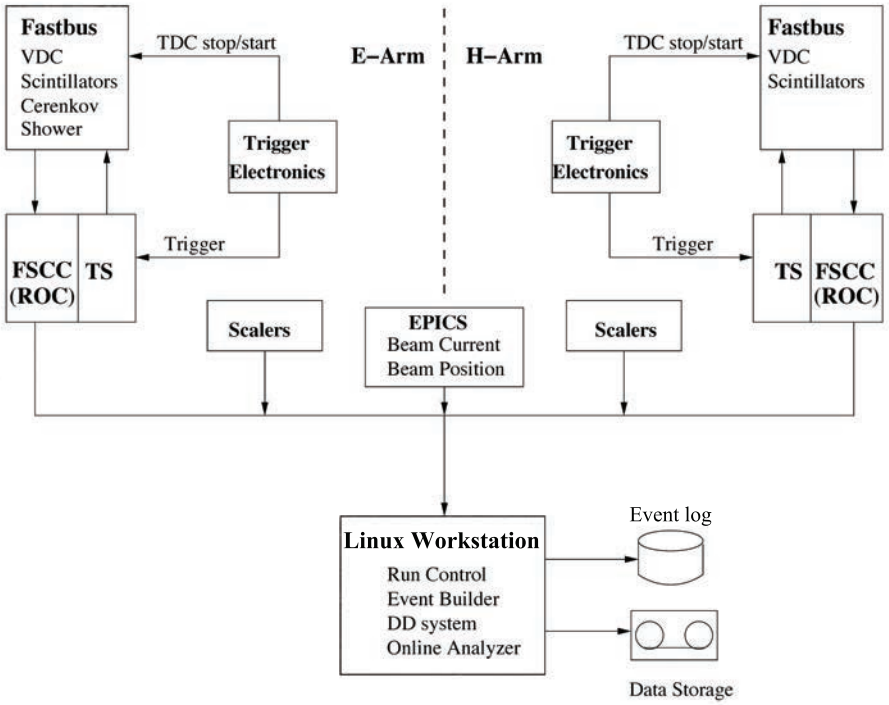

Figure 3.1: Block diagram of the Hall A DAQ system. The E-Arm (H-Arm) was LHRS (BigBite) during E04-007. The abbreviations "DD system" stands for Data Distribution system and "FSCC" stands for Fastbus Smart Crate Controller.

3.1.1 Data Processing

Once the raw signals from the data acquisition have been recorded, the task of interpreting those signals and calculating target vertex variable from this data remains. The recorded CODA file consists of the major components:

- Scaler events (DAQ reads the scaler values every $1-4$ seconds and feeds them into the main data stream. Since counted by stand-alone units, the scaler values are not effected by the DAQ dead time; therefore, they can be used to correct DAQ dead time).
- Physics events from the detectors.
- The header file which has a time stamp and run information such as run number, pre-scale factors and event numbers.

For experiment E04-007, the Hall A C++ Analyzer was used for the analysis of raw data. The Analyzer is developed by Hall A software group based on ROOT, an object oriented framework that has been developed at CERN. The Analyzer first calculates the particle track at the detector's focal plane, then reconstructs the target vertex, and finally calculates physics variables. The next task would be to generate stand-alone programs to further process the tracks and calculate reconstructed quantities (like scattering angle at the target) and physics quantities (missing mass, Q^2, etc.).

3.1.2 Trigger Setup

Trigger signals prompt the data acquisition system to start a readout of the detector information. In E04-007 experiment setup, six different types of triggers were generated and used in the data acquisition. T1, T2, T3, and T7 were singles triggers from the hadron arm (BigBite) and the electron arm (LHRS). T5 and T6 were coincidence triggers. T4 was the LHRS scintillator trigger used for trigger efficiency. T8 was the EDTM (Electronic Dead Time Measurements) pulser trigger. A summary of triggers is listed in Table 3.2. The trigger system consisted of commercial CAMAC and NIM discriminators, delay units, logic units and Memory Lookup Units (MLU). The MLU is a programmable device that, given a combination of logical signals at its inputs, provides a corresponding (programmed) combination of logical signals at its outputs.

Table 3.2: Triggers of E04-007 experiment.

T1	BigBite E-plane
T2	BigBite dE-plane
T3	L-HRS Singles
T4	L-HRS Efficiency
T5	T1.AND.T7
T6	T2.AND.T7
T7	LHRS Singles (center S1 paddles.AND.S2)
T8	EDTM 1024 Hz pulser

3.1.2.1 Single Arm Triggers

The main physics triggers were generated using scintillator signals. In LHRS the scintillators were arranged in two planes, with six scintillator paddles in each plane, and two PMTs viewing each paddle. Therefore, the PMTs of the two scintillator planes provided $2 \times 2 \times 6 = 24$ signals. The trigger of the LHRS, T7, was formed by requiring that both S1 and S2 scintillator planes had a hit and they were close enough to form valid track, i.e., one paddle in S1 and one paddle in S2 had a hit on both sides PMTs. Thus, this trigger requires four fired PMTs. The trigger diagram for LHRS is illustrated in Fig. 3.2.

In BigBite the scintillators were arranged in two planes, E and ΔE, with 24 paddles in each plane, and two PMTs viewing each paddle. Hence, the PMTs of the two scintillator planes provided $2 \times 2 \times 24 = 96$ signals. The triggers of the BigBite , T1 and T2, were formed by requiring that either E or ΔE scintillator planes had a hit, i.e., one paddle in E or one paddle in ΔE had a hit on both sides PMTs. Thus, this trigger requires two fired PMTs. The trigger diagram for E and ΔE triggers are illustrated in Fig. 3.3 and Fig. 3.4.

After generated, all types of triggers have their copies sent to a scaler unit for counting and a trigger supervisor (TS) unit to trigger data acquisition. The TS unit has a pre-scale function. If the pre-scale factor for a specific trigger type is N, then only 1 out of N triggers of that type is recorded in the data stream. This function is very useful to decrease the computer dead time caused by frequent data recording while keeping all the events with useful physics information. Therefore, during the production data taking, all the single arm triggers were highly pre-scaled, and all the T5 (coincidence) trigger events were kept in the data stream.

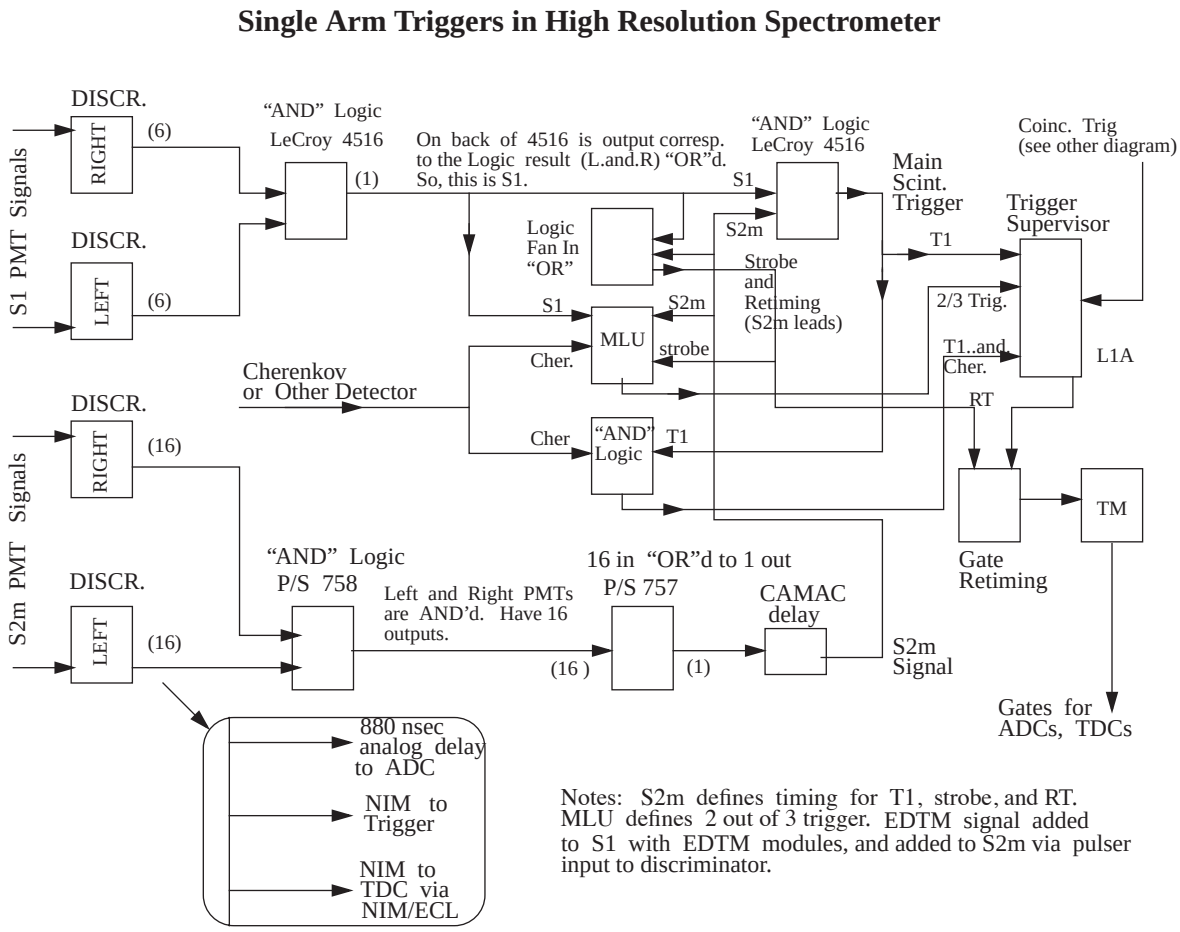

Figure 3.2: Trigger diagram for LHRS during E04-007 (Courtesy of R. Michaels, http://hallaweb.jlab.org/equipment/daq/strig.ps).

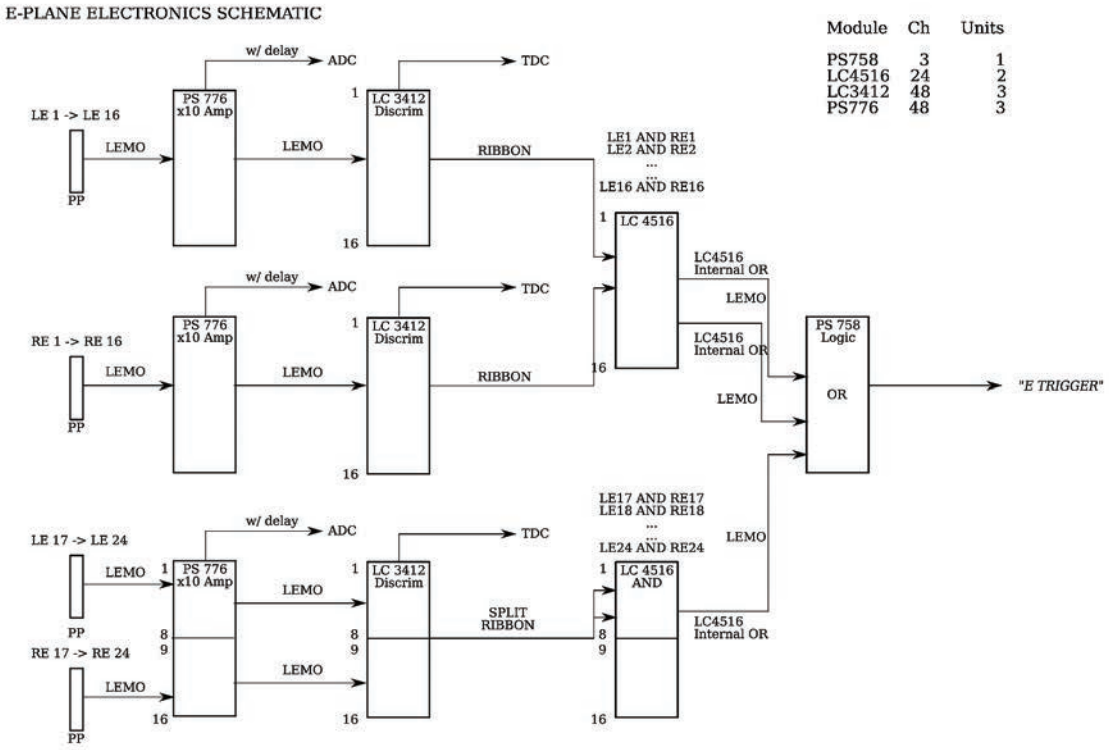

Figure 3.3: Trigger diagram for BigBite E-plane during E04-007.

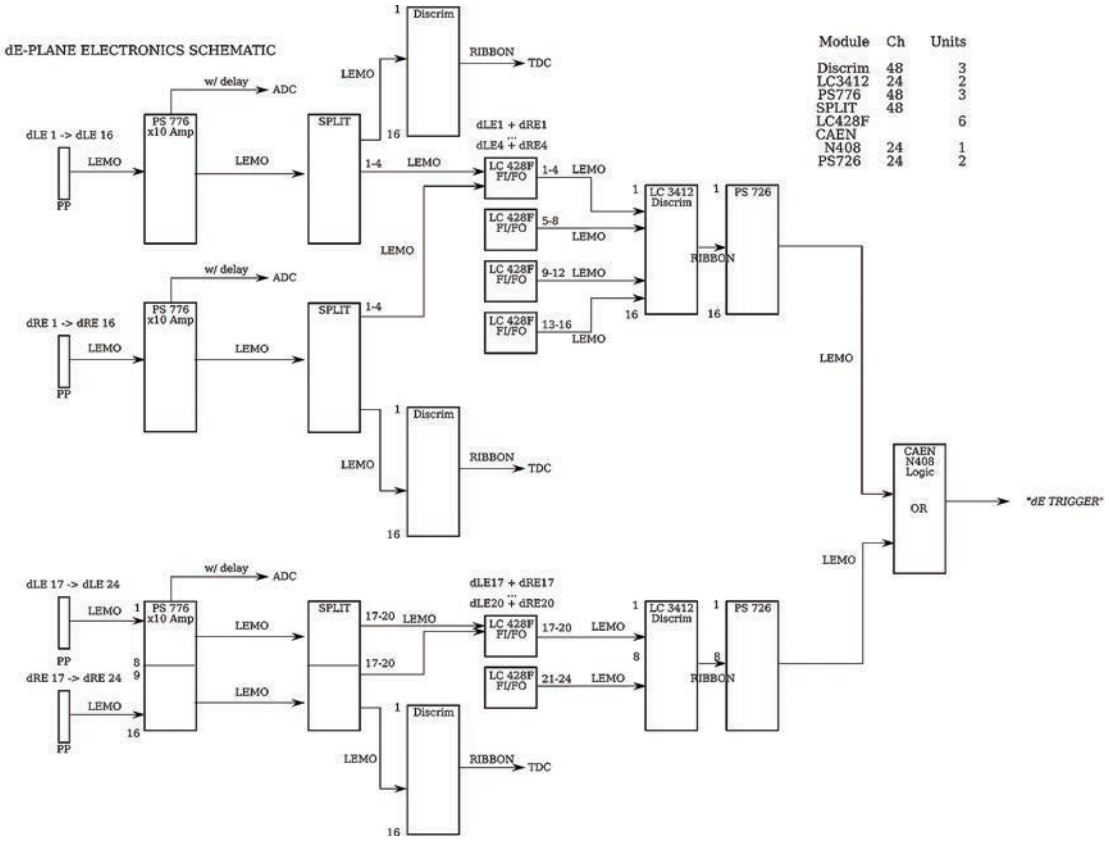

Figure 3.4: Trigger diagram for BigBite ΔE-plane during E04-007.

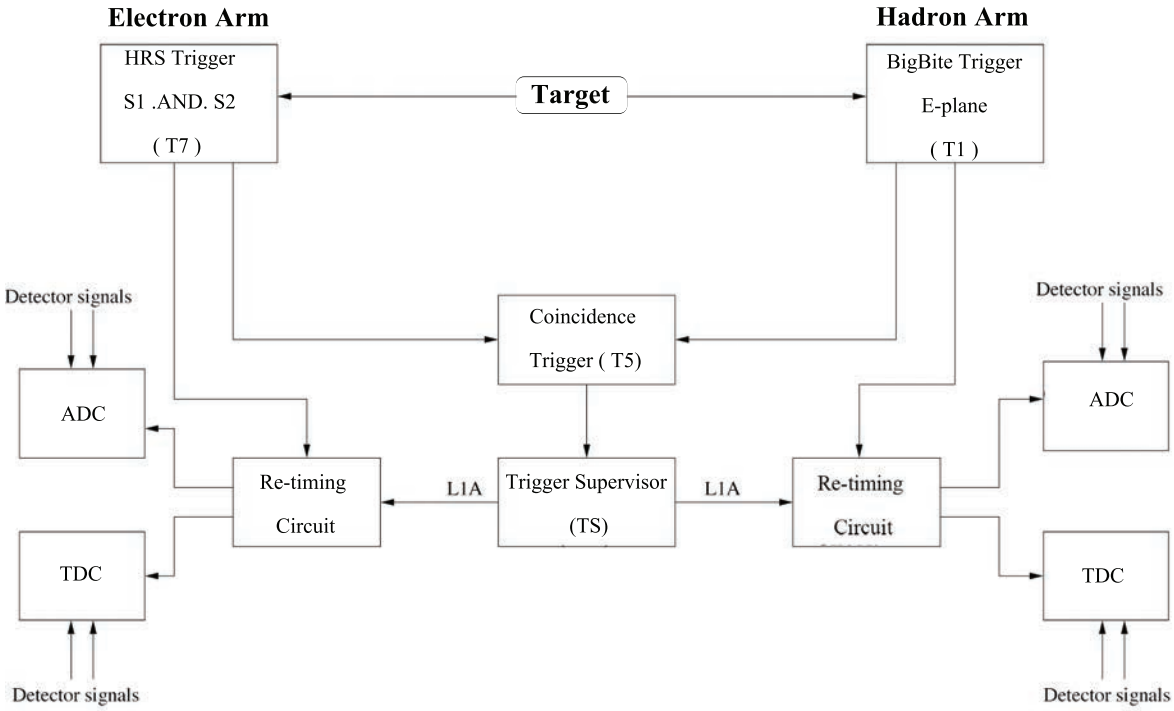

Figure 3.5: Schematic diagram of coincidence trigger setup between two spectrometers.

3.1.2.2 Coincidence Triggers

The coincidence trigger, T5, was formed with the HRS single trigger T7 and the BigBite single trigger T1 by overlapping the two triggers in time (logical AND). A sketch of coincidence trigger setup is shown in 3.5. The exact trigger formation time and the TOF of particles in both spectrometers are crucial in order to design the coincidence trigger. The TOF of the particles in each spectrometer was calculated by the momentum of the particles and distance they travelled in the two spectrometers. Cable delays were then added in T1 and T7, so that there was an overlap between them.

3.2 Data Analysis

Analyzing data includes detector calibration, particle identification, tracking, calculation of physics variables, and applying proper cuts to separate the signal from the background.

In the Hall A physics data analysis model, raw data from DAQ are stored in raw data files. Then, these data are decoded and analyzed by an event-processing program. The event processor creates Root files that contain raw and computed data, typically in Root Tree and

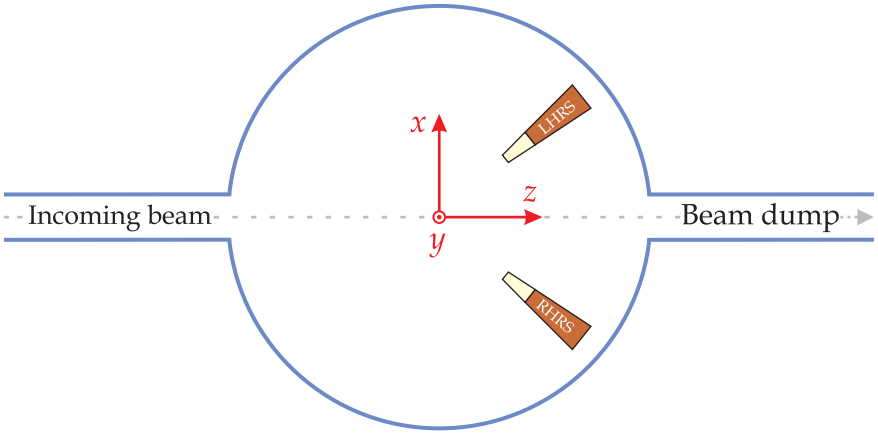

Figure 3.6: Top view of the Hall A coordinate system.

histogram format. Diagnostic information as well as final physics results are then extracted from the Root files using Root scripts. This general scheme applies to both on-line and off-line analysis.

For on-line analysis, experimenters have the option of analyzing either raw data stored in files on local disks of the DAQ computers or a random sample of the raw data stream that is distributed via network in real time. Network distribution is provided by the ET component of the CODA.

For off-line analysis, the raw data files are first retrieved from the JLab mass storage tape silo to staging disks, from where they can be processed either interactively or as part of a batch job. For batch processing, the JLab Computer Center maintains a large PC farm. The farm is shared among the various user groups from all three experimental halls performing data analysis.

In E04-007 experiment, scattered electrons from the $H(e,e'p)\pi^0$ reaction are identified in the LHRS in coincidence with recoiled protons in the BigBite. Analysis of the data for the extraction of asymmetry consists of various tasks. The first task is detector calibration and spectrometer optics optimization.

The principal element in calibration of LHRS is VDC tracking and magnetic reconstruction of the scattered electron momentum, direction and reaction vertex at the target. Reconstructed trajectories of particles in Hall A are specified in various coordinate systems. An overview of the coordinate systems is presented in the next section. A detailed description of the coordinate systems can be found in Ref. [69].

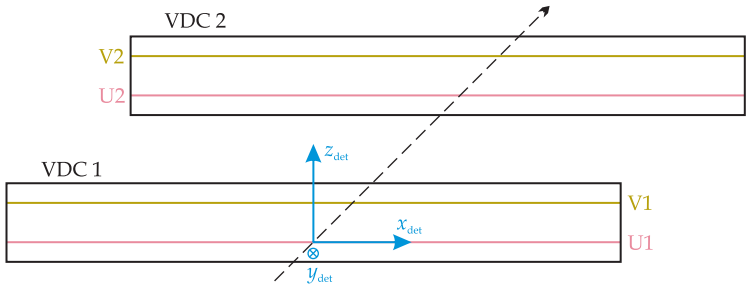

Figure 3.7: Side view of the detector coordinate system.

3.2.1 Coordinate Systems

The coordinate systems used in reconstruction of the trajectories of particles in Hall A are as described below. All coordinate systems are Cartesian.

1. ***Hall A Lab Coordinate System (HLCS)***

   The origin of this coordinate system is defined as the point of the intersection of the unrastered beam, centered in the last two BPMs, and the axis of rotation of the solid-target system. The incident unscattered beam leaves the target along the positive z direction, the y-axis points vertically upward, as shown in Fig. 3.6.

2. ***Detector Coordinate System (DCS)***

   The DCS is defined in relation to the VDCs. The origin of this system is at the intersection of wire number 184 in the first VDC's U1 plane with the perpendicular projection of wire number 184 in the first VDC's V1 plane onto the U1 plane (see Fig. 3.7 and 3.8). From this origin, the x-axis is along the long symmetry axis (dispersive direction) of the lower VDC, the y-axis is parallel to the short symmetry axis (transverse direction) of the lower VDC, and the z-axis is perpendicular to the first VDC's U1 plane pointing vertically upward.

3. ***Transport Rotated Coordinate System (TRCS)***

   The TRCS is obtained by rotating the DCS clockwise by 45° around the y-axis so that the new z-axis direction is along the spectrometers central ray, as shown in Fig. 3.9.

   This axis is also perpendicular to all detectors that follow the VDCs, so that x-axis and y-axis are along the dispersive and transverse directions of those detectors, respectively.

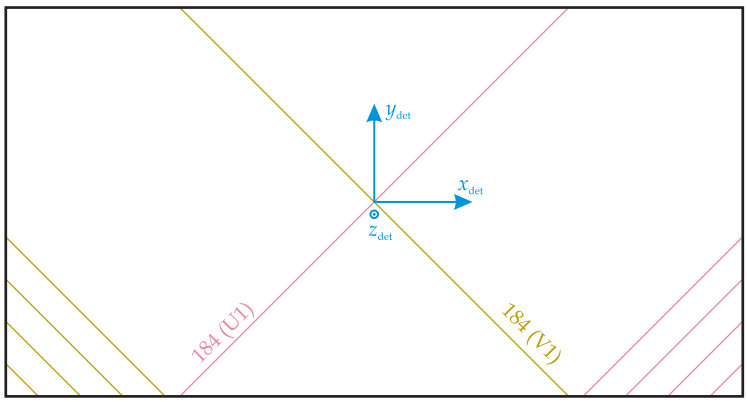

Figure 3.8: Top view of the detector coordinate system.

4. ***Focal Plane Coordinate System (FPCS)***

   The FPCS is a rotated coordinate system. It is obtained by rotating the DCS around its y-axis by an angle ρ, where ρ is the angle between the local central ray and the z-axis of the DCS (see Fig. 3.10). The local central ray is the ray at the focal plane, which for a given δ (the momentum relative to the central momentum of the spectrometer), has $x_{tg} = y_{tg} = \theta_{tg} = \phi_{tg} = 0$.

5. ***Target Coordinate System (TCS)***

   The origin of the TCS is defined as the point at a distance L from the mid-point of the central sieve slit hole, along a ray perpendicular to the sieve slit surface. The line perpendicular to the sieve slit surface of the spectrometer defines the z-axis (z_{tg}) and points away from the target. This of course implies that each spectrometer has its own TCS. The y-axis (y_{tg}) is parallel to the sieve surface in the transverse plane, and the x-axis (x_{tg}) is the line crossing the center of the sieve slit and pointing vertically downward in the dispersive plane. The target coordinate system is right handed. Under optimal circumstances, where the spectrometer is pointing directly at the hall center and the sieve slit is perfectly centered on the spectrometer, the origin of the TCS should coincide with the origin of the HLCS. Figure 3.11 shows a diagram of the TCS for the left spectrometer, where Θ_0 is the central angle of the spectrometer and the tangents of the out-of-plane angle, θ_{tg}, and the in-plane angle, ϕ_{tg}, are defined as

$$\tan\theta_{tg} = \frac{dx}{dz},$$
$$\tan\phi_{tg} = \frac{dy}{dz}.$$

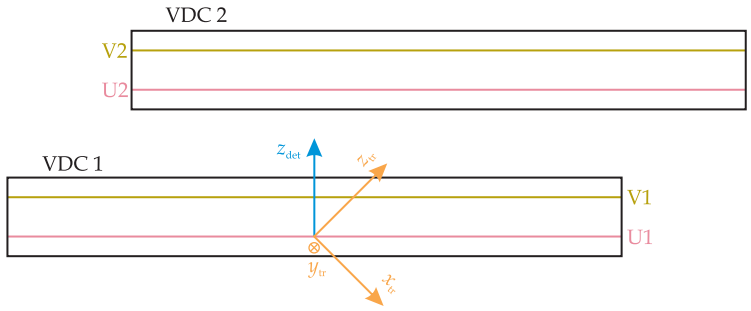

Figure 3.9: Transport rotated coordinate system.

3.2.2 LHRS Optics Calibration

The goal of HRS optics calibration is to connect focal-plane variables with target-coordinate variables. This task is performed by expanding focal-plane variables in polynomials and the coefficients of these polynomials are recorded as matrix elements in HRS databases [62]. When an event is detected by VDCs, two angular and two spatial coordinates are measured. The particle's position and the tangent of the angle made by its trajectory projected onto the dispersive axis are denoted by x_{det} and θ_{det} respectively. Analogous quantities projected onto the non-dispersive axis are denoted by y_{det} and ϕ_{det}. Focal plane coordinates are calculated by correcting for detector offsets from the ideal central ray of the spectrometer. These coordinates are then used to determine the target coordinates and relative momentum of the particle δ by using the optics matrix elements $(\theta_{\text{tg}}, \phi_{\text{tg}}, y_{\text{tg}}, \delta)$. δ is defined as

$$\delta = \frac{|\mathbf{k}| - |\mathbf{k_0}|}{|\mathbf{k_0}|}, \tag{3.1}$$

where $\mathbf{k}$ is the particle's measured momentum and $\mathbf{k_0}$ is the spectrometer central momentum.

The target coordinates of the detected particles are reconstructed from the focal plane coordinates with a set of optics matrix elements. In first-order approximation, a transformation matrix relating the measured focal plane coordinates to their counterparts at the target can be defined as [70]

$$\begin{bmatrix} \delta \\ \theta_{\text{tg}} \\ y_{\text{tg}} \\ \phi_{\text{tg}} \end{bmatrix} = \begin{bmatrix} \langle \delta \mid x_{\text{fp}} \rangle & \langle \delta \mid \theta_{\text{fp}} \rangle & 0 & 0 \\ \langle \theta_{\text{tg}} \mid x_{\text{fp}} \rangle & \langle \theta_{\text{tg}} \mid \theta_{\text{fp}} \rangle & 0 & 0 \\ 0 & 0 & \langle y_{\text{tg}} \mid y_{\text{fp}} \rangle & \langle y_{\text{tg}} \mid \phi_{\text{fp}} \rangle \\ 0 & 0 & \langle \phi_{\text{tg}} \mid y_{\text{fp}} \rangle & \langle \phi_{\text{tg}} \mid \phi_{\text{fp}} \rangle \end{bmatrix} \begin{bmatrix} x_{\text{fp}} \\ \theta_{\text{fp}} \\ y_{\text{fp}} \\ \phi_{\text{fp}} \end{bmatrix}. \tag{3.2}$$

The zero tensor elements of the above matrix result from the mid-plane symmetry of the spectrometer.

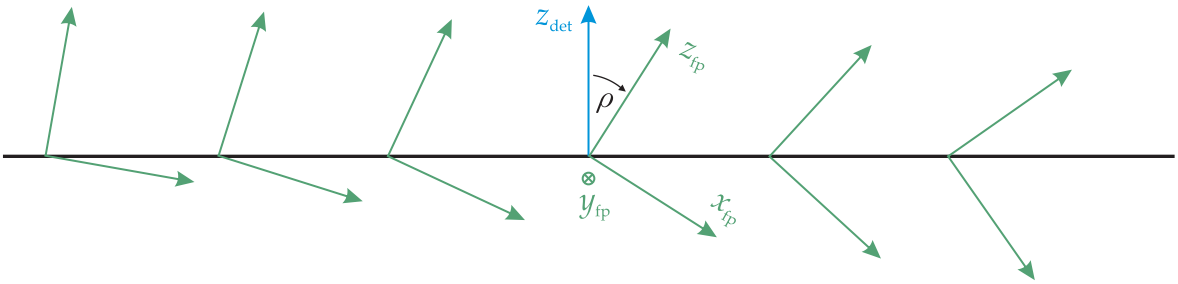

Figure 3.10: Focal plane coordinate system.

The situation in practice, however, is far more complicated, with four transformation tensors - one for each of the trajectory parameters - replacing the matrix in 3.2. The $x_{\rm tg}$ value was fixed at zero during the optics calibration to reduce the number of unknowns at target to four. These tensors are obtained, together with any position offsets of the spectrometer or VDC's, relative to their nominal (central) positions, using an optics optimization procedure. The four tensors are labeled Y_{jkl}, T_{jkl}, P_{jkl}, and D_{jkl} whose elements, which are polynomials in $x_{\rm fp}$ (the expansion of the focal plane coordinates is carried out up to the fifth order), relate focal plane and target quantities according to [70]

$$\begin{aligned} y_{\rm tg} &= \sum_{j,k,l} Y_{jkl}\theta_{\rm fp}^{j} y_{\rm fp}^{k}\phi_{\rm fp}^{l}\,, \\ \theta_{\rm tg} &= \sum_{j,k,l} T_{jkl}\theta_{\rm fp}^{j} y_{\rm fp}^{k}\phi_{\rm fp}^{l}\,, \\ \phi_{\rm tg} &= \sum_{j,k,l} P_{jkl}\theta_{\rm fp}^{j} y_{\rm fp}^{k}\phi_{\rm fp}^{l}\,, \\ \delta &= \sum_{j,k,l} D_{jkl}\theta_{\rm fp}^{j} y_{\rm fp}^{k}\phi_{\rm fp}^{l}\,. \end{aligned} \tag{3.3}$$

The superscripts on focal plane coordinates denote the power of each focal plane variable. The tensors Y_{jkl}, T_{jkl}, P_{jkl}, and D_{jkl} are defined as

$$\begin{aligned} Y_{jkl} &= \sum_{i=1}^{m} C_i^{Y_{jkl}} x_{\rm fp}^{i}\,, \\ T_{jkl} &= \sum_{i=1}^{m} C_i^{T_{jkl}} x_{\rm fp}^{i}\,, \\ P_{jkl} &= \sum_{i=1}^{m} C_i^{P_{jkl}} x_{\rm fp}^{i}\,, \\ D_{jkl} &= \sum_{i=1}^{m} C_i^{D_{jkl}} x_{\rm fp}^{i}\,. \end{aligned} \tag{3.4}$$

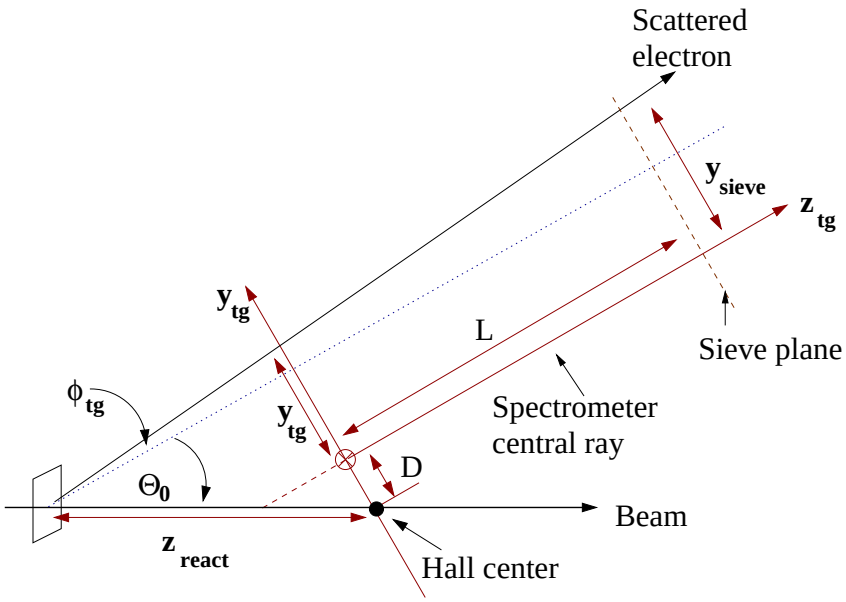

Figure 3.11: Target coordinate system for electron scattering from a thin foil target. The $x_{\rm tg}$ coordinate is not shown, since it is the vertical displacement and points into the page.

In Eqs. 3.4, the i index numerates the powers of $x_{\rm fp}$ in the power expansion of the tensor elements. Mid-plane symmetries of the spectrometer require that in Y_{jkl} and P_{jkl}, $(k + l)$ would be odd, while in D_{jkl} and T_{jkl}, $(k + l)$ would be even. The optics matrix elements $C_i^{Y_{jkl}}$, $C_i^{T_{jkl}}$, $C_i^{P_{jkl}}$, *and* $C_i^{D_{jkl}}$ are read from the database.

The procedure for optimizing these tensors [70] involves detecting electrons which undergo elastic scattering from the optics target (see Table 2.2). The ^{12}C and Ta foil targets were used because the intersection point of the incoming electron beam and any of these foils effectively provides a point target.

During optics data taking a sieve slit collimator was placed at the entrance to the LHRS aperture. The sieve is a 5 mm thick tungsten sheet with a pattern of 49 holes (7×7), spaced 25 mm apart vertically and 12.5 mm apart horizontally. Two of the holes, one in the center and one displaced two rows vertically and one horizontally, are 4 mm in diameter. The rest of the holes are 2 mm in diameter. The large holes allow for an unambiguous identification of the orientation of the image at the focal plane. The target foil position along the beam axis ($z_{\rm react}$) and the position of the center of the sieve slit holes ($x_{\rm sieve}$ and $y_{\rm sieve}$) must be known very accurately. For this reason they were generally surveyed at the beginning of the experiment.

For E04-007 experiment the HRS survey was done before the beginning of the experiment in February. The result of the survey can be found in Appendix D.

The coefficients of the polynomials in equation 3.3 can be determined from this optics data by minimizing the difference between the reconstructed and surveyed target foil and sieve slit hole position.

It was later discovered that no sieve slit data with the ^{12}C foil target had been taken during E04-007 optics calibration running. This prevents us from determining the optics matrix elements for the LHRS. Fortunately, an earlier experiment (i.e., experiment E05-110) had kinematics with comparable momentum. To compensate for the lack of sieve slit in our experiment, we adopted the transport matrix values from the experiment E05-110. When used on our elastic hydrogen runs with sieve slit, the reconstructed x_{sieve} vs. y_{sieve} plot of Fig. 3.12 was obtained, next to which the actual geometric pattern of the sieve slit can also be seen for comparison. In the sieve plot, shown in Fig. 3.12, the two large sieve holes, which are used to determine the sieve orientation (See the sieve pattern on the right side of Fig. 3.12), can be easily identified. As it can be seen, the sieve pattern obtained, in this case for elastic scattering off an extended target, using the adopted transport matrix elements, is in adequate agreement with the expected sieve pattern.

3.2.3 Examining Momentum Calibration of LHRS and BigBite

The momentum calibration of LHRS and BigBite was performed by measuring elastic electron scattering off the cryogenic H_2 target. The momentum and energy measurements must comply with the fact that for elastic scattering kinetic energy and momentum are separately conserved. That means the quantities

$$\Delta p^0 = k^0 + p^0 - k'^0 - p'^0 \,, \tag{3.5a}$$

$$\Delta \mathbf{p} = \mathbf{k} + \mathbf{p} - \mathbf{k'} - \mathbf{p'} \,, \tag{3.5b}$$

$$\Delta p^2 = (k + p - k' - p')^2 \,, \tag{3.5c}$$

must be zero (when the measured momenta are corrected for radiative loses befor and after scattering). In Eqs. 3.5, k, k', and p, p' are the four momenta of incoming, outgoing electron and incoming, outgoing proton of the elastic scattering, respectively. Equation 3.5c gives the "missing mass" for the interaction while Eqs. 3.5a and 3.5b give the "missing energy" and "missing momentum".

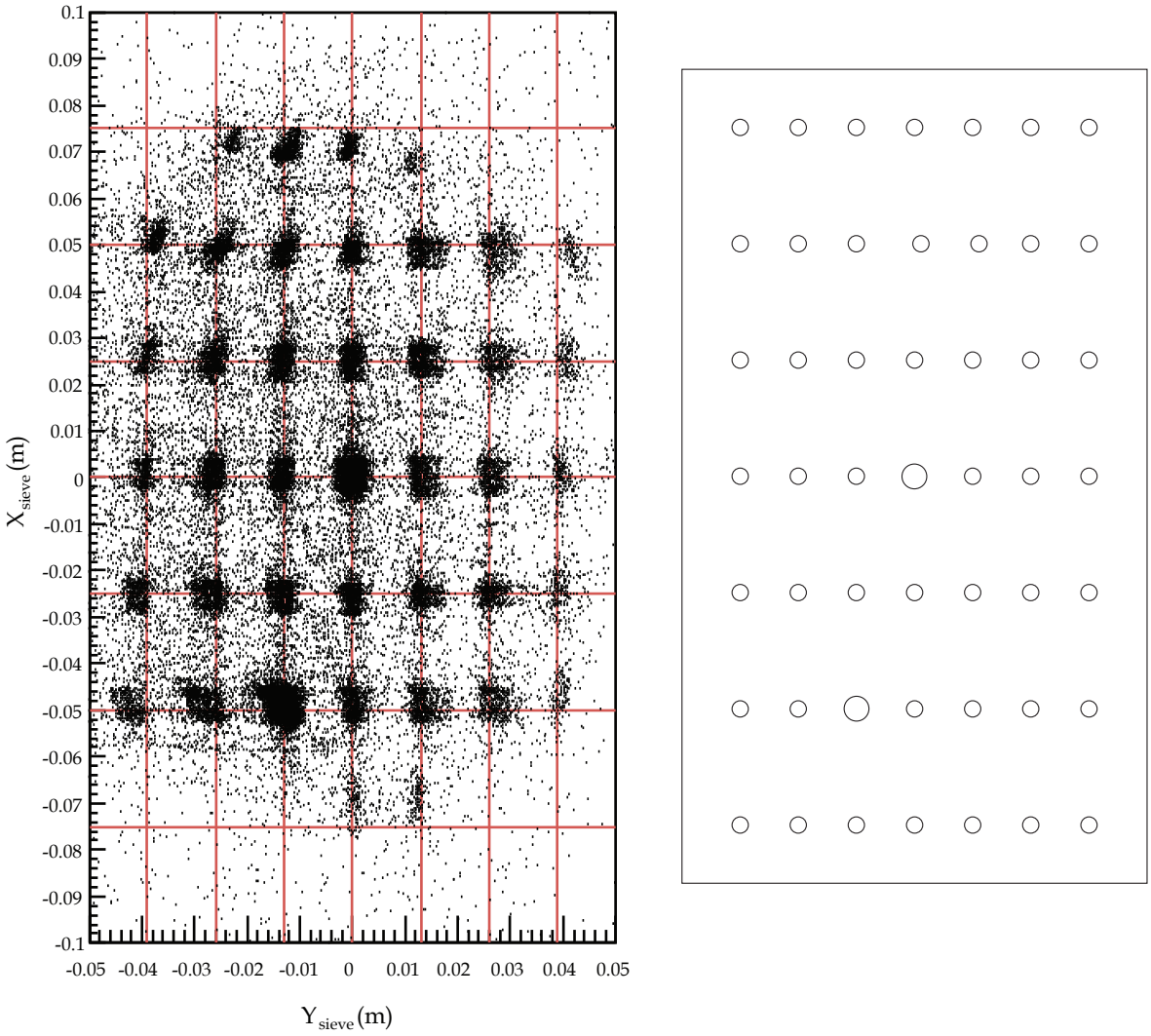

Figure 3.12: Left: Sieve pattern for an elastic run with the LH2 target. The central momentum for LHRS was set to be $p_0 = 0.9654$ GeV/c, and the scattering angle to be $\theta_0 = 35.5°$, Right: Sieve holes' geometry.

The amplitude of missing momentum vector ($|\Delta\mathbf{p}|$) as well as its x-, y-, and z-component, missing energy (ΔE), and missing mass for an elastic coincidence run are shown in Fig. 3.13. The peaks are centered around zero as expected indicating sufficiently accurate momentum calibration of LHRS and BigBite. The width of the peaks are due to the resolution of the two spectrometers, multiple scattering of electrons and protons in the spectrometers, and radiation before and after scattering. Especially, tail of the missing energy spectrum on the positive side (e) and the shifting of the missing momentum and missing mass peaks to positive values (d and f) are due to radiative loses.

3.2.4 Event Selection and Cuts

The event selection and cuts must be chosen very carefully to suppress the accidental background level. Due to the existence of high rate singles, there is a number of multiple-track events (i.e., number of tracks > 1) in LHRS, Fig. 3.14 **a**, and BigBite spectrometer, Fig. 3.14 **b**. For such events, the reconstructed kinematic variables may not be from the real coincidence event of the $H\,(e, e'p)\,\pi^0$ reaction. For that reason, only single-track events were selected for the analysis. Since we are calculating an asymmetry, not a cross section in this thesis, our results are not affected by the loss of efficiency.

In the course of data analysis, we must apply an optimized set of cuts to filter out particles that did not originate from the target, and particles other than those of interest.

In the following sections, we describe the cuts employed to accomplish these objectives.

3.2.4.1 Reconstructed Target Variables

We already saw, in section 3.2.2, that the optical properties of left HRS were parametrized in the transport tensor. After obtaining the optimized transport tensor elements, one can reconstruct the target variables and then place cuts on them. Applying acceptance cuts restrict events to well-understood regions of the spectrometer. However, they should not be made too narrow since this affects the statistical uncertainty. The LHRS variables are shown Fig. 3.15. The angular cuts and target vertex cut applied to the LHRS data include

- $|\phi_{\text{tg}}| < 25$ mrad
- $|\theta_{\text{tg}}| < 55$ mrad
- $-0.03\text{ m} < z_{\text{react}} < 0.03\text{ m}$

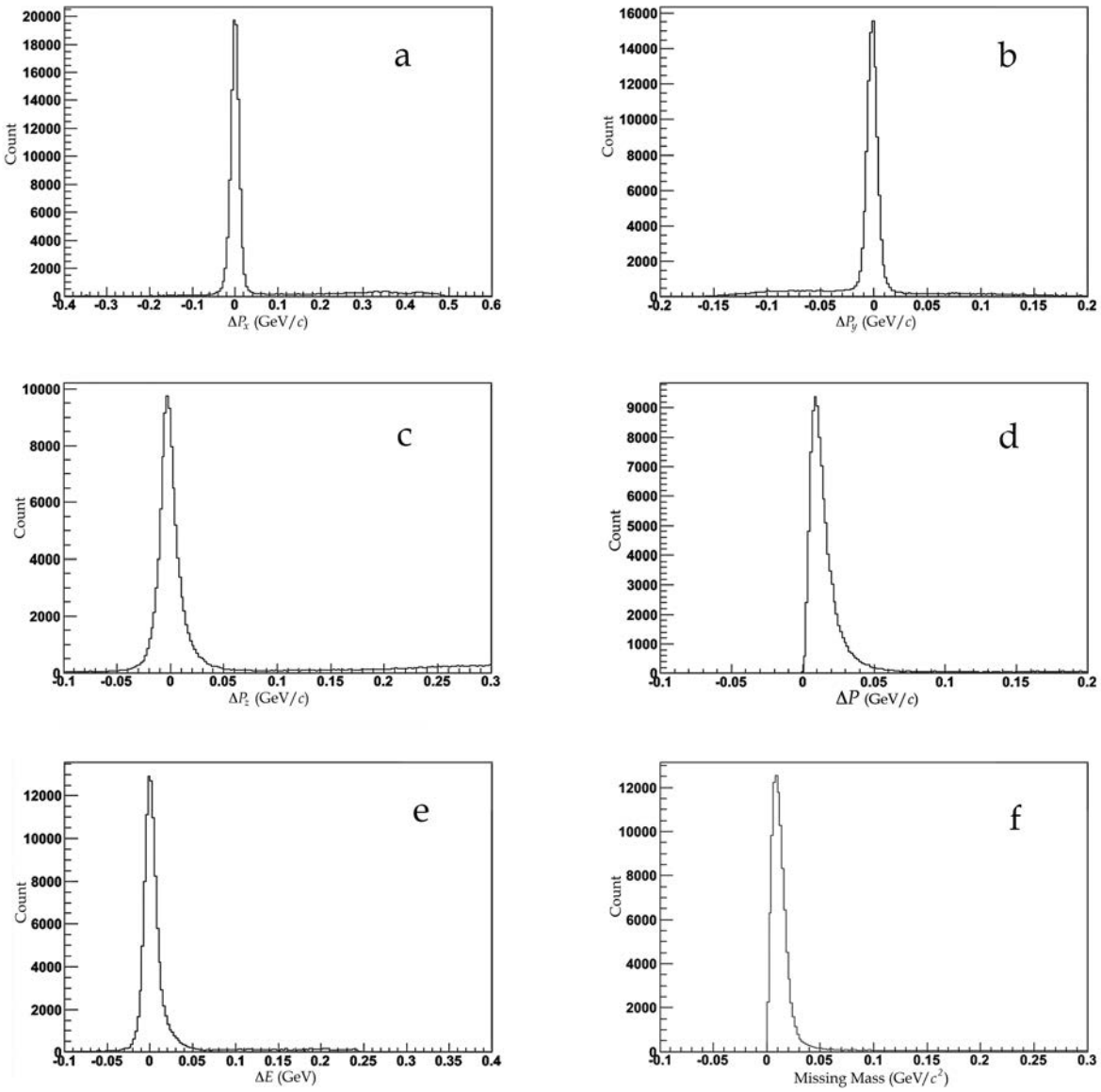

Figure 3.13: Energy-momentum conservation in elastic scatterings: **a**, **b**, **c**, Missing momentum in x, y, and z direction; **d**, Amplitude of missing momentum vector; **e**, Missing energy; **f**, Missing mass.

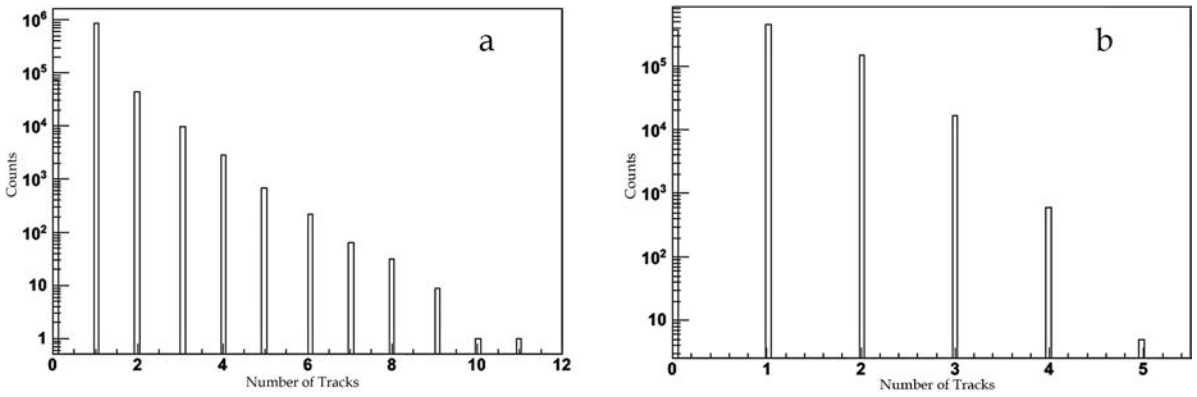

Figure 3.14: Number of tracks distribution: **a**, tracks in LHRS; **b**, tracks in BigBite.

3.2.4.2 Coincidence Time

Rejecting events which do not correspond to a coincidence between the hadron and electron triggers is the next step in cleaning up the data. For each trigger type, a TDC module records the time when the corresponding trigger is received. The coincidence time of flight (TOF) is measured by starting a TDC when a trigger is observed on the LHRS and stopping it when a trigger is observed on the BigBite. Real coincidences events are expected to have a narrow range of coincidence times, since for a given kinematics the momentum range of the recoiled proton is small. There are also random coincidences caused by uncorrelated single-arm events in each spectrometer that just happen to fall within the coincidence time window. These accidental coincidences form a flat background in the coincidence TOF spectrum.

It is desirable to make the coincidence time peak as narrow as possible so the real coincidences are easily separated from background and the statistical uncertainty coming from accidentals within the peak time window is reduced. Much of the width of the raw coincidence TOF peak arises due to the following factors:

- Differences in scintillator offsets.
- Time walk effects due to variation of scintillator signal strengths.
- Differences in path lengths of the electron and proton through the spectrometers.

These effects are taken into account to obtain the corrected TOF spectrum shown in Figure 3.16. The peak at the center of the distribution corresponds to the region where there are good coincidence events, whereas events out of this region are due to false coincidence.

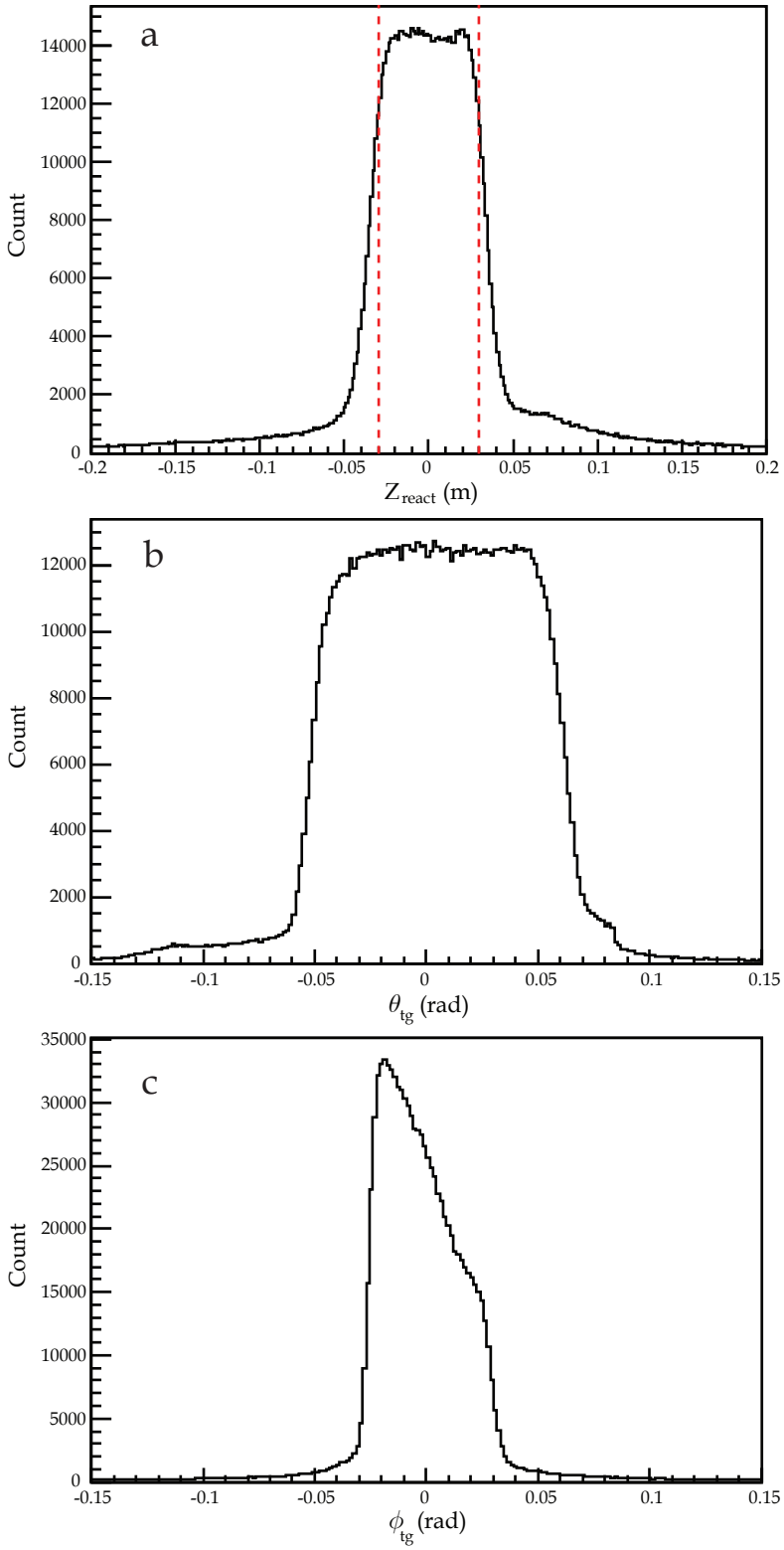

Figure 3.15: LHRS variables : **a**, Target vertex along the beam reconstructed from LHRS data.The cuts filter out particles that did not originate from the target; **b**, Reconstructed θ_{tg} distribution for LHRS **c**,Reconstructed ϕ_{tg} distribution for LHRS.

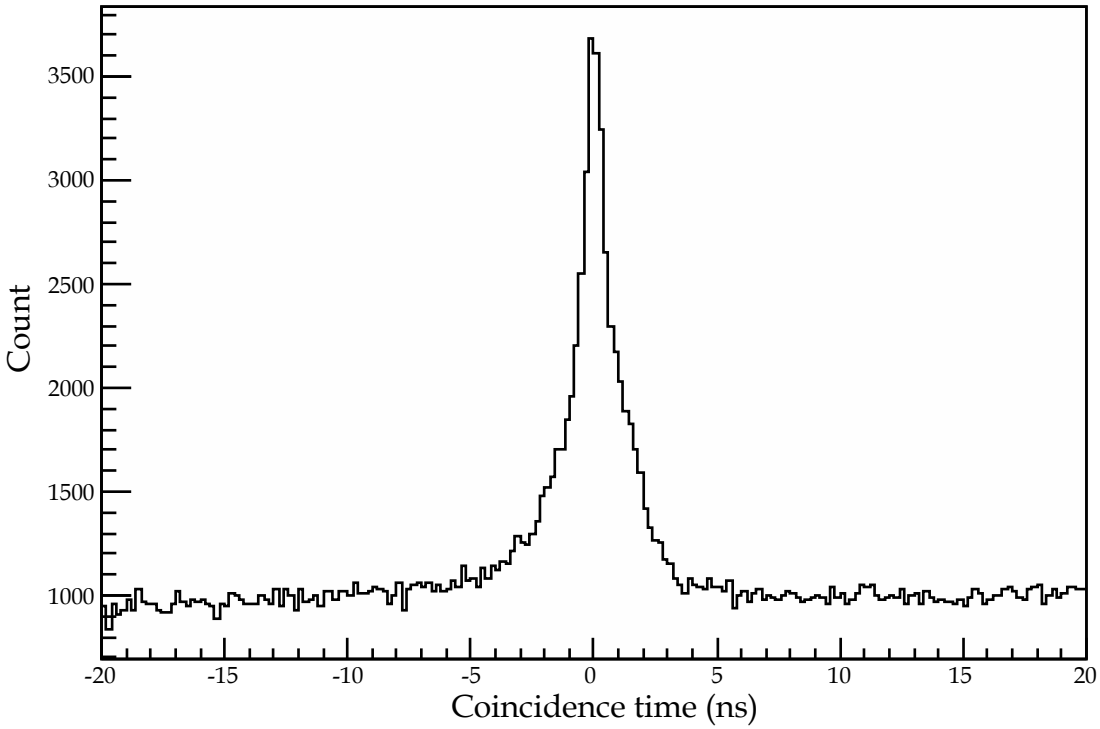

Figure 3.16: The coincidence TOF spectrum. The peak represents real coincidence events.

3.2.4.3 Missing Mass

It was previously mentioned that the neutral pion is detected in coincidence with the scattered electron and ejected proton. The word "detected" maybe a somewhat misleading as we really do not detect the pion through any detector. Instead, we identify coincidence events which correspond to π^0 production. The identification of such coincidence events is through energy-momentum conservation, by matching the undetected mass or what is called the missing mass with the mass of π^0, which is $m_\pi = 134.9766$ Mev [8]. The relation between energies and momenta involved in a π^0 electroproduction event is (in terms of four-momenta)

$$k^\mu + p^\mu = k'^\mu + p'^\mu + p_\pi^\mu , \tag{3.6}$$

where the notation for the four momenta of the process is already explained in section 1.1.2. If we simply rearrange Eq. 3.6 in the form

$$p_\pi^\mu = k^\mu + p^\mu - k'^\mu - p'^\mu ,$$

and square both sides and then take a square root, we obtain

$$\sqrt{p_\pi^2} = m_\pi = \sqrt{(k + p - k' - p')^2}, \tag{3.7}$$

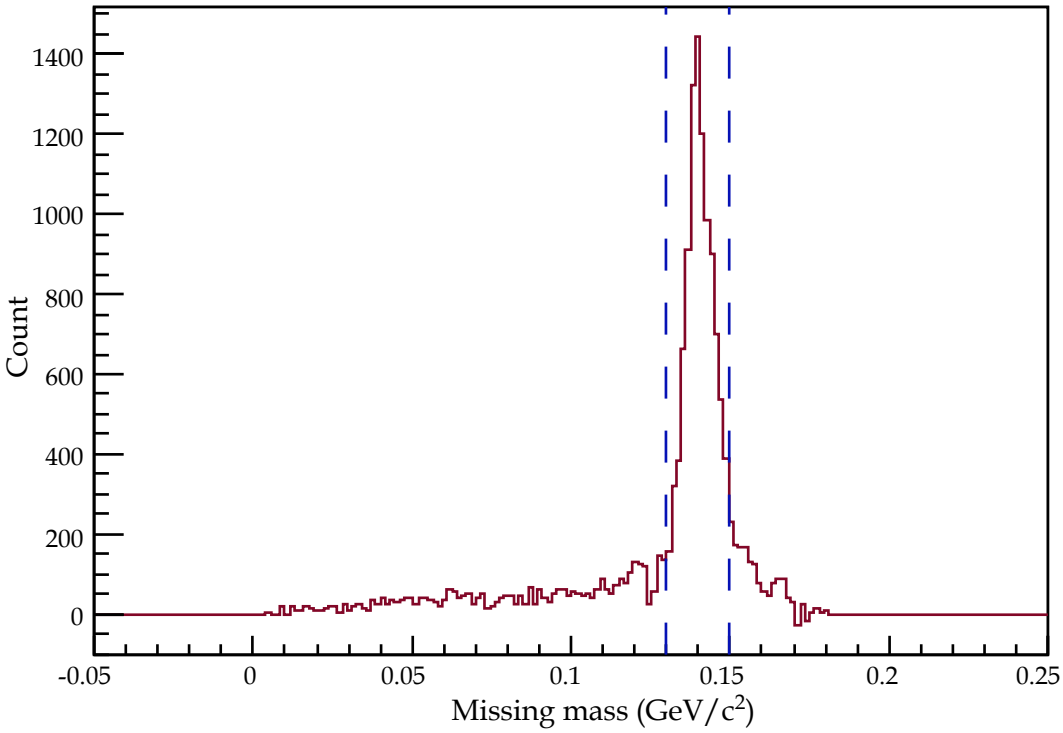

Figure 3.17: Missing mass for a production run.

which is the missing mass. Since the four momentum square of π^0 is always mass square, the right hand side of Eq. 3.7 gets the name "missing mass." To identify coincidence events in which a pion is produced, we must demand that the missing mass, expressed in terms of the four momenta of all other particles that have been detected, would be equal to the mass of π^0. That basically means applying the cut

$$130 \text{ MeV} < \sqrt{(k + p - k' - p')^2} < 150 \text{ MeV}, \tag{3.8}$$

on the data to rule out the irrelevant events. The Shape of the missing mass for coincidence events is shown in Fig. 3.17, which visualizes the cut of Eq. 3.8.

3.2.5 Particle Identification

As described in section 2.6.4, particle identification (PID) on the BigBite spectrometer was achieved by using a set of scintillator detectors. One can identify protons by studying the energy distribution of the proton events in the detector. The first layer, δE-planes, is 3 mm thick, while the second layer, E-plane, is 30 mm thick. The lowest energy protons with kinetic energy smaller than 200 MeV come to stop in the δE plane depositing all their energy in δE, and non in E. The medium energy protons (250 MeV $< KE_P <$ 700 MeV) stop in the E counter. While the fraction of energy they deposit in δE goes down the energy deposited in E goes up with increasing kinetic energy of the protons. Finally the highest energy protons with energy larger than 700 MeV punch through both scintillator planes. The energy deposited by these protons in each plane goes down as proton's kinetic energy increases. Figure 3.18 shows a collection of δE vs. E plots for the energy deposits in the E and δE scintillators. The energy signatures of protons in the scintillator bars can define the cuts for selecting protons, based on their energies. The observed hit patterns in plots of Fig. 3.18 confirm that all 24 scintillator bars record the hits optimally.

3.2.5.1 Background Subtraction

An important part of selecting signal events is minimizing the background due to target walls and other sources. The liquid hydrogen target was enclosed by aluminium walls, and events from beam interactions with the cell walls has to be subtracted from the liquid target yields. The subtraction of events coming from the aluminium target cell that holds the cryogenic target material can be accomplished using the so-called "dummy" target. Aluminium dummy-target data were taken during the experiment. The dummy data are analyzed in the same fashion as the data from the cryotarget i.e., identical cuts are used. The spectra from the dummy target are then created in the variables of interest (missing mass, Q^2, etc.) and subtracted bin by bin from the cryotarget spectra.

After applying various cuts and subtracting background, the data need to be corrected for inefficiencies such as data acquisition dead time, tracking inefficiencies, and detector inefficiencies. which good events might be lost.

For asymmetry measurements, the systematic uncertainties such as detector efficiencies, target density, absolute charge measurement, spectrometer acceptance and dead time of data acquisition cancel to the first order. However, the experimental inefficiencies need to be kept

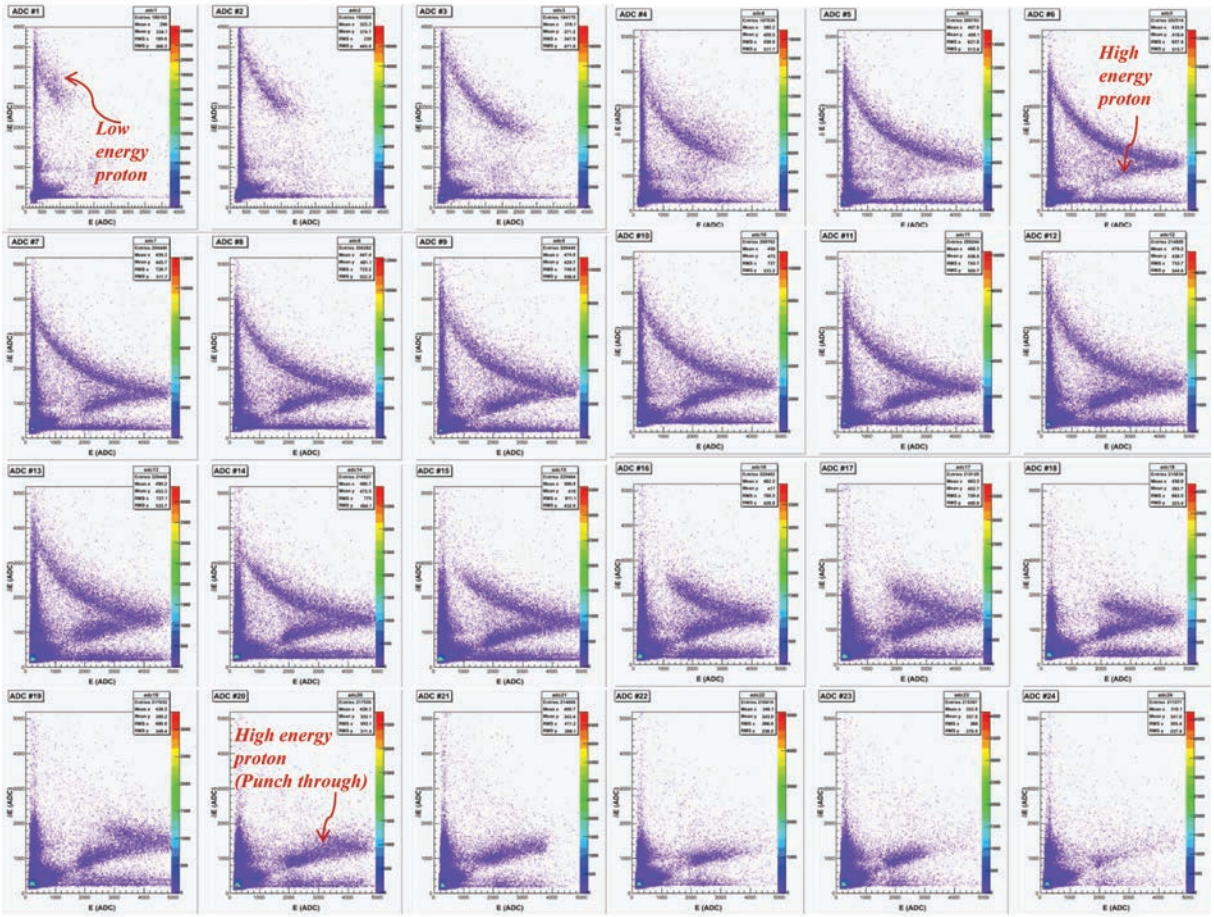

Figure 3.18: Two-dimensional distribution of energy deposits in all 24 bars of the E and δE scintillators. The low energy protons come to stop in δE, protons with higher energies pass through δE and cease the motion in E. Those with even higher energies punch through both scintillators.

low, so that the second order helicity dependent asymmetries do not arise. A brief explanation of the experimental asymmetries is presented here for completeness.

3.2.5.2 Computer and Electronic Dead Time

The computer dead time is due to the finite time required for the electronic modules and computers to process an event, so the dead time refers to a potentially good event not being recorded because the data acquisition was busy. Therefore, one must correct for events that are lost or not recorded during this processing time. In general, dead times can be divided into two categories: non-extendible (non-paralyzable) and extendible (paralyzable) [66]. In the non-extendible case, the module in question ignores new inputs while processing an event. So-called extendible modules will accept additional input while processing the first event, and extend the output generated accordingly. This produces a prolonged period during which no event is accepted. The element is thus paralyzed.

Experimentally, the computer dead time is directly measured by scalers that record the number of triggers. The triggers are only read out for those events for which the Trigger Suprvisor (TS) is not busy.

Chapter 4

Asymmetry

Asymmetry observables have been postulated and measured throughout physics to test our understanding of space-time, spin and parity. Most of the time the definition of asymmetry is purely experimental, based on the number of events with positive and negative value of a dynamical observable, such as momentum, helicity, etc. The objective is to see whether the interaction involved regards the sign of that dynamical observable. For example, in a scattering experiment if the cross section changes value with the orientation of the spin of the projectile it is a clear indication that the interaction is spin-dependent. An asymmetry is most useful when we can tag events with dynamical observables that are two-valued, such as spin, helicity, chirality, and forward or backward motion. In such cases, the asymmetry is defined as the subtraction of events with positive and negative tags divided by the sum of them, i.e., total number of events. This way, the asymmetry is a dimensionless fraction, which is often represented as percentage. Experimentally speaking, the notable advantage of an asymmetry measurement is that most of the possible systematic uncertainties such as, detector efficiencies, target density, absolute charge measurements, spectrometer acceptance and the dead time of data acquisition, which are often difficult to determine, cancel to the first order.

In a scattering experiment like E04-007, the physical definition of asymmetry is expressed in terms of cross sections, as we defined $A_{TL'}$ in Eq. 1.21 back in chapter 1. That is the subtraction of cross sections tagged positive and negative, according to the helicity of the projectile, divided by the sum of them. However, because cross section is directly proportional to the number of events, the aforementioned definition reduces to a more experimental definition in terms of number of events. For our case the TL' asymmetry can be rewritten in the form

$$A_{TL'}(\theta_{\pi,\mathrm{CM}}) = \frac{1}{\mathcal{P}_e} \left. \frac{\tilde{N}^+(\theta_{\pi,\mathrm{CM}}) - \tilde{N}^-(\theta_{\pi,\mathrm{CM}})}{\tilde{N}^+(\theta_{\pi,\mathrm{CM}}) + \tilde{N}^-(\theta_{\pi,\mathrm{CM}})} \right|_{\phi_{\mathrm{CM}}=\mathrm{const.}}, \tag{4.1}$$

where $\mathcal{P}_e$ is the beam polarization and $\tilde{N}^{\pm}(\theta_{\pi,\mathrm{CM}})$ are the normalized number of qualified[1] events with positive/negative beam helicity, which correspond to a pion ejected into given $\theta_{\pi,\mathrm{CM}}$ and ϕ_{CM}.

The TL' asymmetry measures the sensitivity of the interaction to the beam helicity. Obviously, if the scattering had no helicity dependence the cross section would not differ for positively or negatively polarized incident electrons. The sensitivity of the interaction to the helicity of the beam is manifested itself in the $R_{TL'}$ structure function (see Eq. 1.19), which appears in the cross section only because of beam polarization. The consequence of $A_{TL'}$ defined at $\phi_{\mathrm{CM}} = 90°$ in Eq. 1.21, is that in the numerator the $\sin\phi_{\mathrm{CM}}$ that accompanies $R_{TL'}$ in Eq. 1.19 becomes unity and in the denominator R_{TL} will be absent because of its $\cos\phi_{\mathrm{CM}}$ factor in Eq. 1.19. In principle, however, $A_{TL'}$ can be defined at any ϕ_{CM} and $\theta_{\pi,\mathrm{CM}}$ to observe its energy (Q^2 and ΔW) dependence. Although angular distribution of $A_{TL'}$ is a potent test for theoretical models, the current discrepancies are primarily Q^2 and ΔW dependent. Therefore, an $A_{TL'}$ at a fixed $\theta_{\pi,\mathrm{CM}}$ would provide more information regarding the nature of the discrepancies between theory and experiment at low Q^2s and ΔWs.

4.1 Asymmetry in Terms of Experimentally Measured Quantities

The asymmetry given in Eq. 4.1 involves $\tilde{N}^{\pm}$, which is the normalized number of events. If $N^{\pm}(\theta_{\pi,\mathrm{CM}})$ is the number of events that refer to the creation of a pion into $\theta_{\pi,\mathrm{CM}}$, the normalized number of events is defined as

$$\tilde{N}^{\pm}(\theta_{\pi,\mathrm{CM}}) = \frac{N^{\pm}(\theta_{\pi,\mathrm{CM}})}{Q^{\pm}}, \tag{4.2}$$

where $Q^{\pm}$ is the gated charge of $\pm$ helicity. The charge delivered under each helicity state is registered by BCM readout (bcmu3 was used for analysis), which basically refers to the number of incident electrons, gated by the helicity state. The above normalization is necessary from two equivalent standpoints. First is that in the definition of cross section the number of events into the angle θ is to be divided by the incoming flux, which in this case can be

[1] By *qualified* we mean events that pass the physical and technical selection criteria, explained in section 3.2.4, for being a valid π^0 production event.

replaced with the accumulated charge. Second is that by this normalization we make sure of the universality of the data. Meaning that we can combine runs with different incoming flux and that the data are on the same footing with other experimental data with different beam luminosity. In asymmetry measurement, this normalization manifests itself even in a smaller scale. The division by accumulated charge for each helicity state in every run of the experimental data, ensures that the difference, $N^+/Q^+ - N^-/Q^-$, is due to the physical nature of the collision and not related to the different number of incoming electrons. Since the number of events can change by the incoming electron flux, if the charge normalization for each helicity state is ignored, the difference between ± number of events causes a *false* asymmetry which is basically due to the beam flux.

The normalization of asymmetry in Eq. 4.1 by beam polarization $\mathcal{P}_e$ has the same justification. The beam polarization can vary during an experiment and it differs from one experiment to another. Therefore by this normalization we in fact give asymmetry per unit polarized electron, which does not depend on beam polarization percentage. The TL' asymmetry, therefore, in terms of measurable quantities is simply given by

$$A_{TL'}\left(\theta_{\pi,\mathrm{CM}}\right) = \frac{1}{\mathcal{P}_e} \left. \frac{N^+\left(\theta_{\pi,\mathrm{CM}}\right)/Q^+ - N^-\left(\theta_{\pi,\mathrm{CM}}\right)/Q^-}{N^+\left(\theta_{\pi,\mathrm{CM}}\right)/Q^+ + N^-\left(\theta_{\pi,\mathrm{CM}}\right)/Q^-} \right|_{\phi_{\mathrm{CM}}=\mathrm{const.}} . \tag{4.3}$$

4.2 Asymmetry Error Calculations

The uncertainties in the experiment are separated into two groups, statistical and systematic uncertainties. This section describes the sources of statistical and systematic errors associated with the measured asymmetry and includes estimates of the magnitude where appropriate.

4.2.1 Systematic Uncertainty

It's been already mentioned that error estimation for asymmetry is free of most systematic uncertainties since they cancel out to the first order. Those include detector efficiencies, target density, absolute charge measurements, spectrometer acceptance and the dead time of data acquisition. However, systematic uncertainties due to beam polarization and the aluminium contamination of events (from the target cell) need to be evaluated.

An error in the Møller measurements of beam polarization $\mathcal{P}_e$, which appears in asymmetry through Eq. 4.3, causes a corresponding error in the experimental values of $A_{TL'}$. The relative

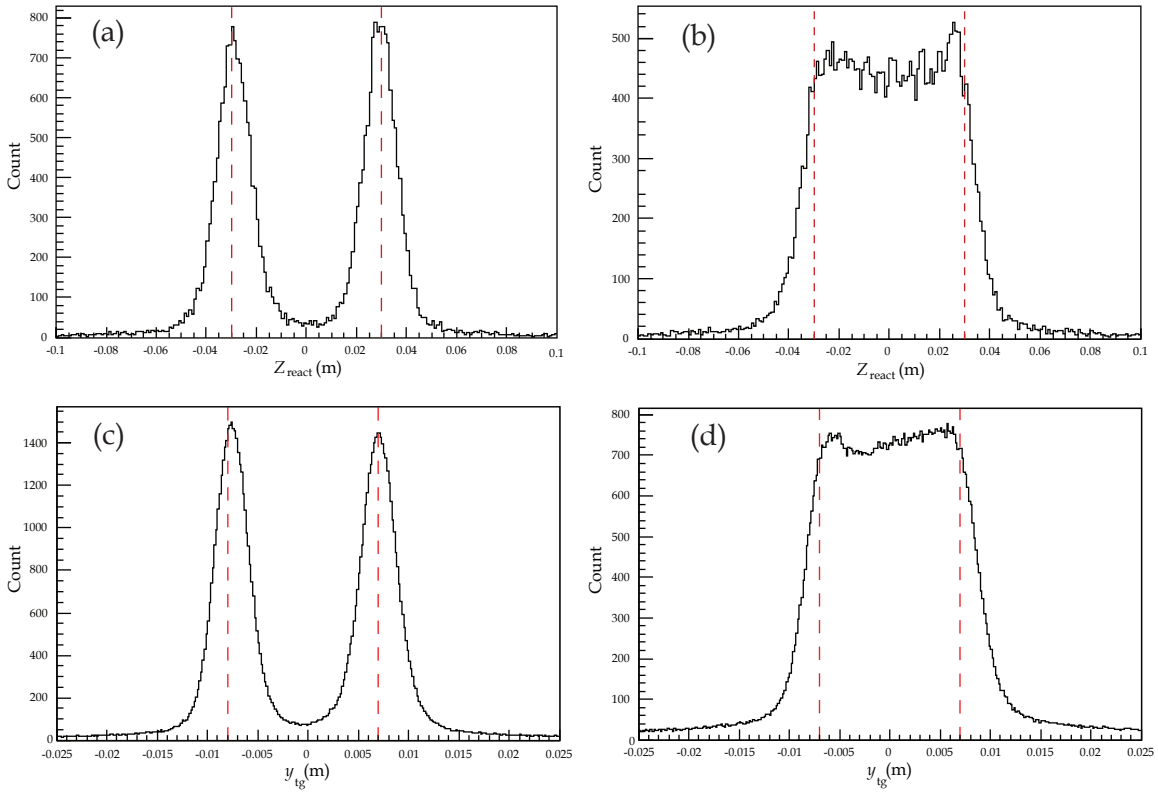

Figure 4.1: Event distribution along the beam line: (a) for a dummy aluminium run; (b) for a hydrogen run. Event distribution along y_{tg}: (c) for a dummy aluminium run; (d) for a hydrogen run. Vertical dashed lines indicate the applied cuts.

uncertainty in beam polarization measurements amounts to 3%. This translates into a 3% relative error in $A_{TL'}$ due to beam polarization. Given that the size of the measured asymmetry is about $1-2\%$, the absolute uncertainty due to polarization measurement is only about 0.06%.

Another source of error is the events associated with the scatterings off the aluminium cap of the target cell, through the reaction ^{27}Al$(e,e'p)$, which have passed the selection criteria for good events. Electron scatterings off a dummy aluminium target cell provides us with the data that can be used to estimate the amount of aluminium event contamination in production runs. Figure 4.1 (a) shows the distribution of aluminium events along the beam line, Z_{react}, which was obtained from a dummy-target run [2], analyzed through the same selection cuts as a hydrogen target. In Fig. 4.1 (b), we display the distribution of events along the beam line for a hydrogen target in the same kinematics configuration. Figure 4.1 (c), shows the y_{tg} spectrum

[2]The dummy run presented in Fig. 4.1 (a) is taken from the kinematics configuration K. For other kinematics configurations, one observes the same aluminium event distribution along the target width, with just different number of events.

Table 4.1: The aluminium contamination for different kinematics settings. The range in Q^2 for each kinematics setting is due to HRS acceptance.

Central Q^2 (GeV/c)^2	Q^2 range (GeV/c)^2	Aluminium event contamination (%)
0.056	0.043-0.073	8.6
0.076	0.059-0.094	6.7
0.097	0.076-0.116	7.2
0.146	0.122-0.165	2.5

for the aluminium events at exit window. The y_{tg} spectrum for the hydrogen target is shown in Fig. 4.1 (d). If we assume that running conditions (e.g., beam energy, trigger setup, etc.) were the same for both aluminium dummy and hydrogen target in each kinematics, the fraction of aluminium events in hydrogen events can be found through a division of normalized number of events

$$R = \frac{N_{Al}/T_{Al}Q_{Al}\,(1-DT_{Al})}{N_{H_2}/T_{H_2}Q_{H_2}\,(1-DT_{H_2})} = \frac{T_{H_2}}{T_{Al}}\frac{N_{Al}Q_{H_2}\,(1-DT_{H_2})}{N_{H_2}Q_{Al}\,(1-DT_{Al})}\,, \tag{4.4}$$

where $T_{H_2(Al)}$ is the thickness of the cap (see section 2.4), $Q_{H_2(Al)}$ is the charge accumulated, $N_{H_2(Al)}$ is the number of events and $DT_{H_2(Al)}$ is the DAQ dead time, for the hydrogen (aluminium) target. The percentage errors in number of hydrogen events due to aluminium event contamination are listed in Table 4.1 for Each kinematics setting. As the table indicates the contamination due to end-caps is lass than 9% for all of our settings. Therefore we assign a 9% systematic error in asymmetry due to end-cap contribution. This uncertainty combined in quadrature with the contribution due to polarization measurement gives a total systematic uncertainty of approximately 10% (relative). The relative statistical uncertainty for all our data points is approximately 20 – 30% (see Table 4.3) . Therefore our systematic uncertainty is smaller than statistical uncertainty for all settings.

4.2.2 Statistical Uncertainty

The effects of counts which qualify as valid events but are indeed background should be considered in the statistical error analysis of asymmetry measurement. We determine the number of background events and their asymmetry by using a cut in the coincidence TOF spectrum. This background TOF cut window has the same width (8 ns) as the good events cut,

but is over the flat region of the TOF spectrum to the right of the coincidence TOF peak (see Fig. 3.16). The normalized number of events $\tilde{N}^{\pm}$ for each helicity is the subtraction of *measured* and *background* events, i.e.,

$$\tilde{N}^{\pm} = \tilde{N}^{\pm}_{\mathrm{m}} - \tilde{N}^{\pm}_{\mathrm{bg}} \,. \tag{4.5}$$

We may define a measured and background asymmetry as

$$A_i = \frac{\tilde{N}^{+}_{i} - \tilde{N}^{-}_{i}}{\tilde{N}^{+}_{i} + \tilde{N}^{-}_{i}} \,, \tag{4.6}$$

where $i = \mathrm{bg}, \mathrm{m}$ standing for background and measured, respectively. If we further define a dilution factor f

$$f = \frac{\tilde{N}^{+}_{\mathrm{bg}} + \tilde{N}^{-}_{\mathrm{bg}}}{\tilde{N}^{+}_{\mathrm{m}} + \tilde{N}^{-}_{\mathrm{m}}} \,, \tag{4.7}$$

it is easy to show that the asymmetry can be written in the form

$$A = \frac{A_{\mathrm{m}} - f A_{\mathrm{bg}}}{1 - f} \,. \tag{4.8}$$

The corresponding error in asymmetry is then given by

$$(\delta A)^2 = \frac{1}{(1-f)^2}\left[(\delta A_{\mathrm{m}})^2 + (f\delta A_{\mathrm{bg}})^2 + \left(\frac{A_{\mathrm{m}} + A_{\mathrm{bg}}}{1-f}\right)(\delta f)^2\right] \,. \tag{4.9}$$

To obtain error for the asymmetry data representing a kinematics of many runs, the asymmetry data and errors of all runs must be consolidated into one according to the error weighted sum

$$A_\alpha = \frac{\sum_j A_j \Big/ \delta A_j^2}{\sum_j 1 \Big/ \delta A_j^2}, \tag{4.10a}$$

$$\frac{1}{\delta A_\alpha} = \sqrt{\sum_j \frac{1}{\delta A_j^2}}, \tag{4.10b}$$

where α indicates a given kinematics and j a run within kinematics α.

4.3 The Extraction of Asymmetry from Experimental Data

We explained in chapter 3 how the raw data were acquired (in section 3.1) and how they needed to be handled (in section 3.2) to be meaningful.

The asymmetry is extracted from the sets of data collected throughout the experiment that proved to be meaningful from both physical and technical standpoints. The considerations

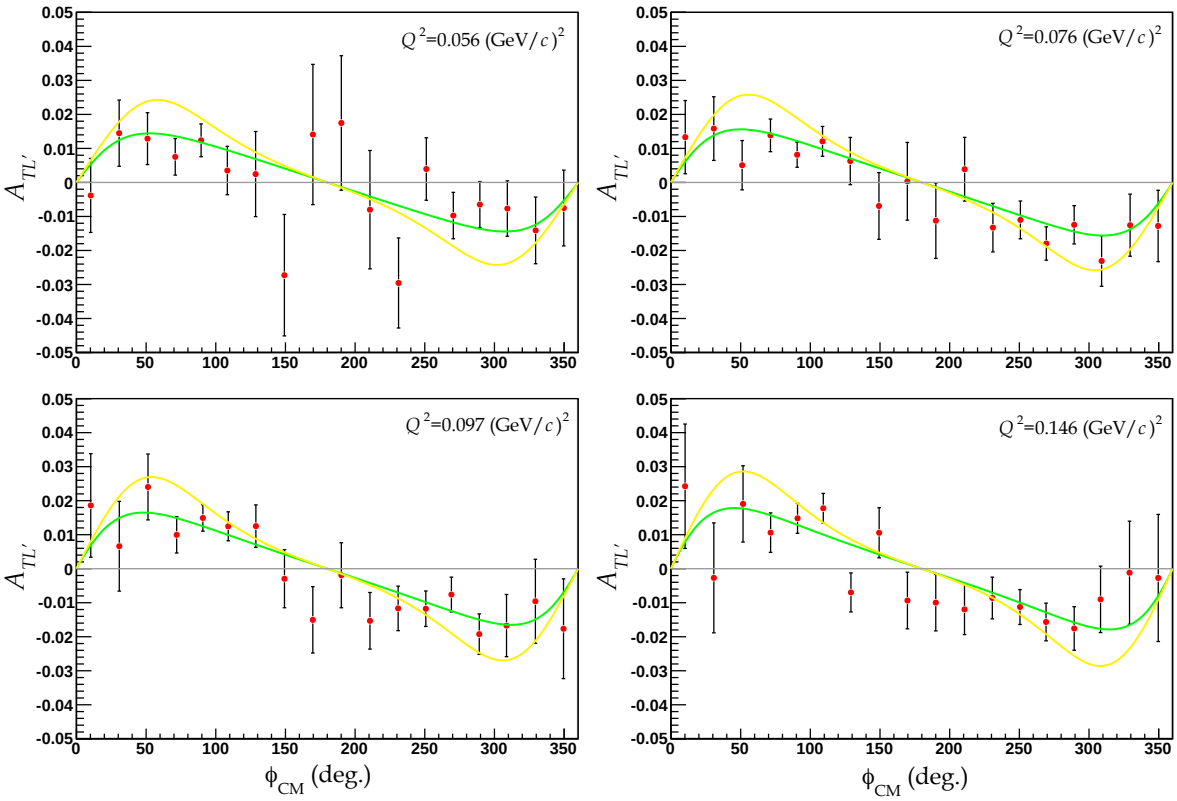

Figure 4.2: ϕ_{CM} dependence of asymmetry at various Q^2s for integrated $0° \leq \theta_{\pi,\mathrm{CM}} \leq 180°$ and $0\ \mathrm{MeV} \leq \Delta W \leq 20\ \mathrm{MeV}$: red circles are the present experimental data; green line, DMT model [39]; yellow line, MAID model [38].

and tasks involved in the process of turning *raw* data into *analyzed* data was explained in section 3.1.

After we take into account all calibration steps (sections 3.2.2,3.2.3, 3.2.4, 3.2.4.1) and particle identification considerations (section 3.2.5) through analyzing raw data, we can begin to extract the desired physical quantities from the analyzed data. The asymmetry extraction from analyzed data involves two major steps:

1. The calculation of asymmetry according to its experimental definition of Eq. 4.3.

2. The estimation of error for asymmetry according to the method outlined in section 4.2.

In the first step, the *measured*[3] qualified number of events $N_{\mathrm{m}}^{\pm}$ with ± electron helicity states are identified through the application of missing mass cut (section 3.2.4.3) on analyzed

[3]In accordance to the nomenclature used in previous section, where measured number of events include both true and accidental ones, see Eq. 4.5.

Table 4.2: The configurations pertaining to each kinematics (given central Q^2) from which runs were taken to extract asymmetry.

Central Q^2 (GeV/c)^2	Q^2 range (GeV/c)^2	Configurations	E_{Beam} (MeV)
0.056	0.043-0.073	D, E, L	1193
0.076	0.059-0.094	C, F, K	1193
0.097	0.076-0.116	B, G, J	1193
0.146	0.122-0.165	A, H, I	1193

data, which ensures that events correspond to the production of a neutral pion in coincidence with the detection of the kinematically-correlated scattered electron and recoiled proton. The state of incoming electron's helicity is additionally identified through the helicity variable in the analyzed data, which is used to tag the number of qualified events as $N^{\pm}_{m}$ for each beam helicity state.

As explained in section 3.2.4.2 the $N^{\pm}_{m}$ may still have accidental events due to background that must be dealt with. The rejection of background events $N^{\pm}_{bg}$ is taken into account through the application of the time-of-flight cut (section 3.2.4.2), which gives us the ability to identify the true number of events $N^{\pm}$, in Eq. 4.5, and perform the error calculations.

Since we would like to present the asymmetry at fixed Q^2s, an organization of all runs pertaining to each Q^2 is necessary. In Table 4.2, we summarize the configurations related to each kinematics[4]. Due to finite acceptance of the left HRS, the Q^2 in each kinematics setting varies slightly within a range which is given in Table 3.1. The values of fixed Q^2 for which we present data are indeed the central values pertaining to each kinematics. Once analyzed data for all corresponding runs at a given Q^2 is combined, the evaluation of asymmetry for both *measured* and *background* events is achieved straightforwardly since $Q^{\pm}$ charge is read off the corresponding BCM and the beam polarization $\mathcal{P}_e$ = 67% is known through Møller measurements (see Appendix E). At this point, a test to experimental asymmetry values is its ϕ_{CM} distribution. Figure 4.2 shows the experimental asymmetry data against ϕ_{CM} in comparison with MAID [38] and DMT [39] curves, which indicate a symmetrical behaviour for $A_{TL'}$ as expected. This concludes the first step of the asymmetry extraction procedure, stated above.

[4]A similar but more comprehensive table, Table 3.1, was given in chapter 3.

For the second step, the error estimation, the measured and background asymmetries of each run yield the corresponding error for that run through Eq. 4.9. Combining the asymmetry values of all runs within a given kinematics, we also evaluate the error by combining the errors of all runs within that kinematics using the error weighted sum expressions of Eqs. 4.10.

4.4 Results

In this section, we present the experimental asymmetry data in two forms

1. At fixed Q^2 versus ΔW.

2. At fixed Q^2 versus $\theta_{\pi,\mathrm{CM}}$.

The experimental determination of $A_{TL'}$ at low Q^2 near threshold as a function of ΔW, Q^2, and $\theta_{\pi,\mathrm{CM}}$ is the main goal of this experiment. A comparison of $\theta_{\pi,\mathrm{CM}}$ distribution of $A_{TL'}$ between theory and experiment helps discriminating between theoretical models.

The new experimental asymmetry data at various Q^2s versus ΔW are presented in Fig. 4.3 along with theoretical predictions from MAID [38], DMT [39] and HBChPT [36, 37]. The experimental $A_{TL'}$ data are also provided in tabular form in Table 4.3. Looking at Fig. 4.3, it is clear that the DMT predictions seem mostly in agreement with experiment. Large disagreements with MAID were also observed in previous experimental work of Ref. [61] at $Q^2 = 0.05$ (GeV/c)^2 (see the already familiar[5] Fig. 4.4), which exists with similar magnitude in the presented data at $Q^2 = 0.056$ (GeV/c)^2, as MAID model overestimates the experiment. This issue, however, does not seem to be limited to just very low Q^2. Present data show that MAID predictions do not compare well with experiment at higher Q^2 values either, as it can be seen in Fig. 4.3.

For all four Q^2s, DMT predictions are in better agreement with the present JLab data. At $Q^2 = 0.056$ (GeV/c)^2 the agreement between DMT values and the present data is not as well as it was with previous experimental data at $Q^2 = 0.05$ (GeV/c)^2 (see Fig. 4.4). Since the two Q^2s are very close, it seems that the presented data has weakened the DMT agreement with experiment at $Q^2 \simeq 0.05$ (GeV/c)^2. Despite its better agreement with experiment than MAID, the DMT predictions seem to overshoot our data especially for $\Delta W > 25$ MeV at $Q^2 = 0.076$ and 0.146 (GeV/c)^2.

As for HBChPT predictions, which motivated the E04-007 experiment, the comparisons with the present JLab data have mixed qualities. Let us begin by looking at the comparison

[5] This figure is Fig. 1.7 in chapter 1, which is presented here as well for an easy read.

Table 4.3: The present experimental values of asymmetry at various Q^2s tabulated against ΔW, which were obtained by integrating $\theta_{\pi,\mathrm{CM}}$ and ϕ_{CM} over $[0°, 180°]$ and $[20°, 120°]$, respectively.

	$Q^2 = 0.056(\mathrm{GeV}/c)^2$		$Q^2 = 0.076(\mathrm{GeV}/c)^2$		$Q^2 = 0.097(\mathrm{GeV}/c)^2$		$Q^2 = 0.146(\mathrm{GeV}/c)^2$	
ΔW (MeV)	$A_{TL'}$	$\pm\ \delta A_{TL'}$	$A_{TL'}$	$\pm\ \delta A_{TL'}$	$A_{TL'}$	$\pm\ \delta A_{TL'}$	$A_{TL'}$	$\pm\ \delta A_{TL'}$
5	0.005	0.012	0.009	0.009	-0.004	0.011	0.002	0.014
10	0.001	0.008	0.009	0.006	0.030	0.008	0.019	0.009
15	0.011	0.006	0.007	0.005	0.005	0.006	0.019	0.007
20	0.009	0.005	0.019	0.004	0.012	0.005	0.014	0.006
25	0.008	0.004	0.012	0.003	0.011	0.004	0.019	0.005
30	0.017	0.004	0.014	0.003	0.018	0.004	0.012	0.005
35	0.021	0.004	0.015	0.003	0.018	0.004	0.026	0.005
40	0.015	0.004	0.016	0.003	0.020	0.004	0.012	0.005
45	0.016	0.006	0.014	0.005	0.014	0.005	0.015	0.006

for $Q^2 = 0.056\ (\mathrm{GeV}/c)^2$. This Q^2 is particularly important since it is close to the $Q^2 = 0.05\ (\mathrm{GeV}/c)^2$ comparison of Fig. 4.4, where there was a sharp disagreement between HBChPT and experimental data of Ref. [61]. The presented data seem to be in better agreement with HBChPT than any of the theoretical predictions up to 30 MeV away from the threshold. Starting from $\Delta W = 30$ MeV, the DMT model is in better agreement with the present data compared to ChPT. Therefore, the disparity between ChPT and previous experimental data of Ref. [61] at $Q^2 = 0.05\ (\mathrm{GeV}/c)^2$, Fig. 4.4, seems to have been reduced by the presented data, for $Q^2 = 0.056\ (\mathrm{GeV}/c)^2$, at least for the near threshold region of $\Delta W < 30$ MeV. Even though this partial agreement at very low Q^2 seems to be a good news for ChPT calculations, comparisons at higher Q^2s do not add to this success very much. As it can be seen from Fig. 4.3, the agreement between ChPT predictions and the present data reduces to $\Delta W \leq 15$ MeV for $Q^2 = 0.076, 0.097\ (\mathrm{GeV}/c)^2$ and even $\Delta W \leq 5$ MeV for $Q^2 = 0.146\ (\mathrm{GeV}/c)^2$, within experimental errors.

The present JLab data for $\theta_{\pi,\mathrm{CM}}$ distribution of asymmetry for $\Delta W = 20$ and 40 MeV bins[6] within each Q^2 are presented in Fig. 4.5, where they are compared with MAID, DMT and HBChPT predictions. The experimental data are also provided in tabular forms in Tables 4.4 and 4.5. Overall, MAID predictions overestimate the experimental data except in forward and

[6] $\Delta W = 20$ and 40 MeV bins correspond to 15 MeV $\leqslant \Delta W \leqslant$ 25 MeV and 35 MeV $\leqslant \Delta W \leqslant$ 45 MeV intervals, respectively.

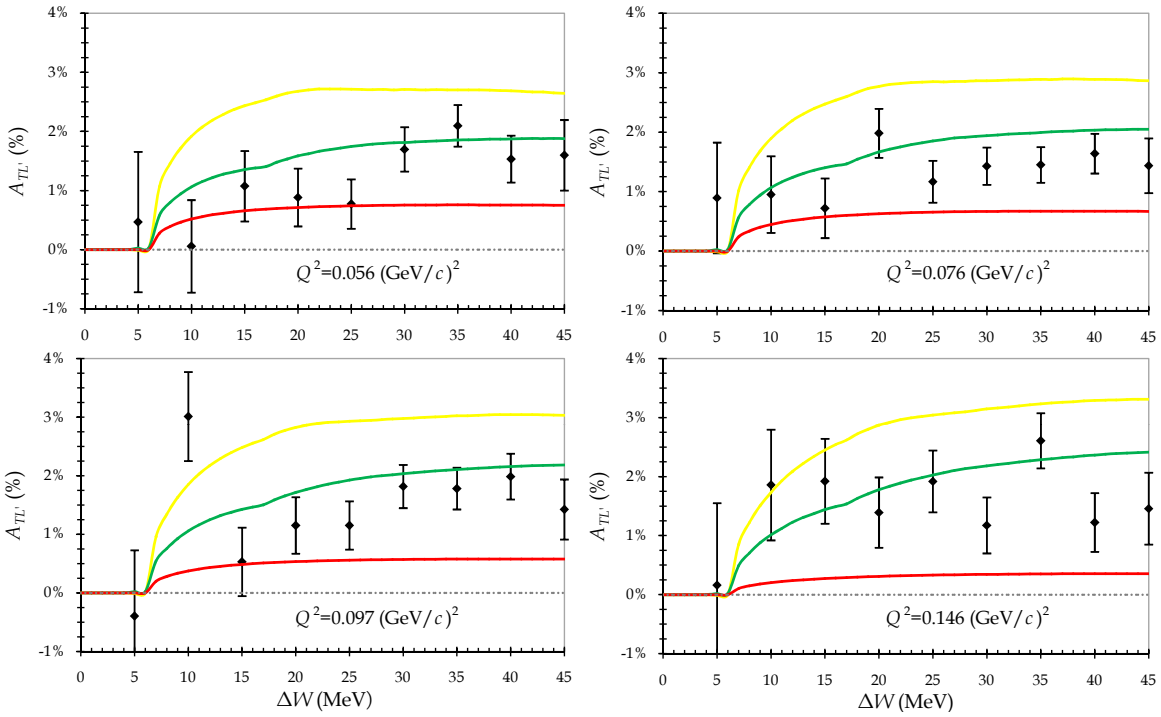

Figure 4.3: Asymmetry at various Q^2s for integrated $\theta_{\pi,\mathrm{CM}}$ and ϕ_{CM} over $[0°, 180°]$ and $[20°, 120°]$, respectively: diamonds are the present experimental data; green line, DMT model [39]; yellow line, MAID model [38]; red line, HBChPT [36, 37].

backward scattering regions.

DMT predictions are in better agreement with the present data compared to MAID. However, at $Q^2 = 0.056$ (GeV/c)^2 DMT values are only in accordance with the presented data for backward scattering angles. This disparity with experiment reduces as Q^2 increases for DMT predictions, while the general overestimation of MAID stays unchanged for all Q^2s.

Figure 4.5 shows that HBChPT predictions are in better agreement with experiment at lower Q^2 values of 0.056 and 0.076 (GeV/c)^2 for the $\Delta W = 20$ MeV bin compared to higher Q^2s. For $Q^2 = 0.056$ (GeV/c)^2 and the $\Delta W = 20$ MeV bin, ChPT values are mostly within the error bars of the present data, better than those of DMT model. This agreement, however, fades away for the $\Delta W = 40$ MeV bin. Generally speaking, HBChPT values at a given Q^2 and for the $\Delta W = 40$ MeV bin agree with experiment only in forward and backward scattering angles, except for $Q^2 = 0.097$ (GeV/c)^2, where the agreement is only limited to backward direction. In these cases ChPT underestimates the experiment for intermediate angles by about a factor of two. At $Q^2 = 0.097, 0.146$ (GeV/c)^2 and for the $\Delta W = 20$ MeV bin, ChPT values are generally lower than experimental data except for forward and backward scattering angles. This is while

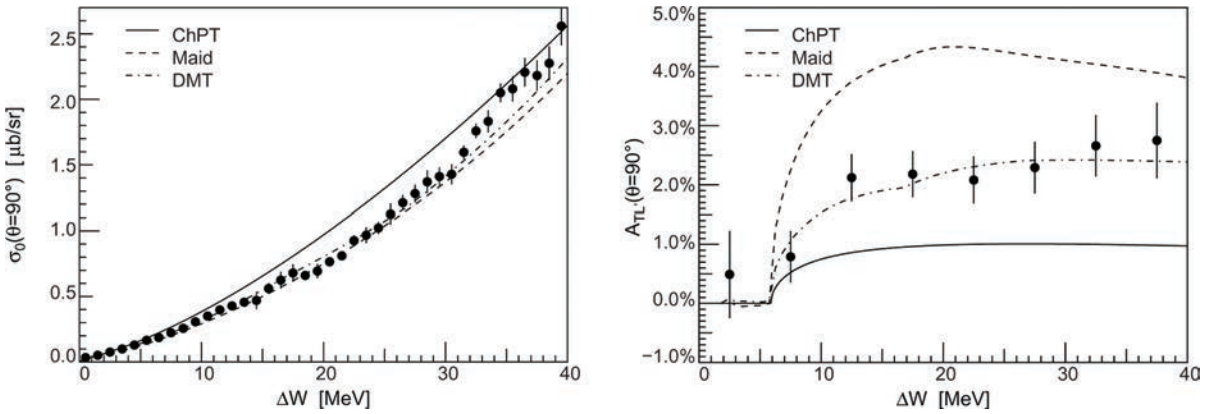

Figure 4.4: π^0 electroproduction unpolarized differential cross section $\sigma_0 = \sigma_T + \epsilon_l \sigma_L$ (left) and TL' asymmetry (right) at $Q^2 = 0.05$ (GeV/c)^2 versus ΔW: circles, the experimental data [61]; ChPT [36, 37], DMT [39] and MAID models [38] are indicated on the graphs.

DMT model is in better agreement with experiment at $Q^2 = 0.097$ (GeV/c)^2 for the $\Delta W = 20$ MeV bin, where its values are mostly within the error bars.

Putting ChPT aside, we see that the two phenomenological models, MAID and DMT, have good agreement with each other and experiment in cross section data versus ΔW (Fig. 4.4). Nonetheless, they do not agree with each other in asymmetry data versus ΔW at various Q^2s. Further insight into the two models may reveal the reason.

The MAID model is a phenomenological effective field theory which demands unitarity and isopsin symmetry on final hadronic states. While it utilizes conventional Lagrangians for γNN, $\gamma\pi\pi$ interactions, it uses two different interaction Lagrangians for πNN system: One in pseudo-scalar and one in pseudo-vector form. The pseudo-vector Lagrangian is preferred since it fulfils the partially conserved axial current symmetry and is consistent with LETs and ChPT to leading order. However, as the pseudo-vector term is anomalous at higher energies and cannot be renormalized, the model switches to pseudo-scalar term at some threshold energy. The model includes terms for heavy mesons ρ and ω exchanges and treats baryon excitations in Breit-Wigner form (see the diagrams e, f, g, and h in Fig. 1.5).

On the other hand, the most important note about DMT model is that it is not a field theory. It is a meson exchange model that incorporates the dynamics of pions, nucleons and excitations. The DMT model follows the methods of relativistic quantum mechanics to calculate transition amplitudes between relevant hadronic states through the appropriate potentials. The transitions can be represented by diagrams for better visualization but by no

means is it a diagrammatic approach through perturbation theory. Even though DMT is not a field theory, it enjoys potentials from effective field theories like MAID and ChPT. In that sense, the transitions between Fock space states via a comprehensive Hamiltonian, which contains potentials from the second quantization space, lean toward a field theoretic treatment. The model possesses a Hamiltonian that includes free and interaction terms. The interaction terms are propagated by free propagator (advanced or retarded Green's function) to formulate the transition or T-matrix. The T matrix is the equivalent of the scattering S matrix except that it is a solution to an integral equation where the Green's function of the free theory propagates the interaction and the T matrix. In the evaluation of T matrix, the model takes potentials from MAID and ChPT. One important feature of the model is the off-shell pion re-scattering in the final hadronic states. The assumption is that the pion, regardless of the creation mechanism, scatters off the nucleon repeatedly (perhaps creating a pion cloud around the nucleon) before it breaks free. This scattering feature intends to describe the excitations. Models with similar assumptions have shown improvements in their results for multipoles, at low Q^2 [44, 71, 72].

Near threshold, the contributions of excitation states are negligible. That means the consideration of final state interactions through pion scattering is not contributing much in terms of excitations. Having said that, phenomenological studies have shown that the inclusion of pion-nucleon interaction in final state at near threshold has an effect in improving the values of multipoles[7], even though it has been dominated by a single re-scattering term [39].

Since the 2001 version of MAID, the final state interactions have been added to the model through phenomenological terms. However, the addition of final state interaction in MAID does not include the off-shell pion re-scattering.

The two models have fundamental differences in approach and elements of their calculations for π^0 electroproduction. If we assume that the DMT model's approach through utilizing potentials from MAID and ChPT produces equivalent results as those of MAID, then the difference may be the absence of the off-shell pion re-scattering in the MAID model. However, this can be only the source of disparity if the two models' approaches came out equivalent in the absence of final state hadronic interactions for both of them.

It is difficult to point out a simple source of success for DMT over MAID, so is to pinpoint a simple reason as why MAID is not in agreement with experimental asymmetry considering

[7]This shows that the phenomenological effects of the off-shell pion re-scattering terms are not limited to the intermediate excitations, otherwise it would not have made an improvement in the multipoles near threshold.

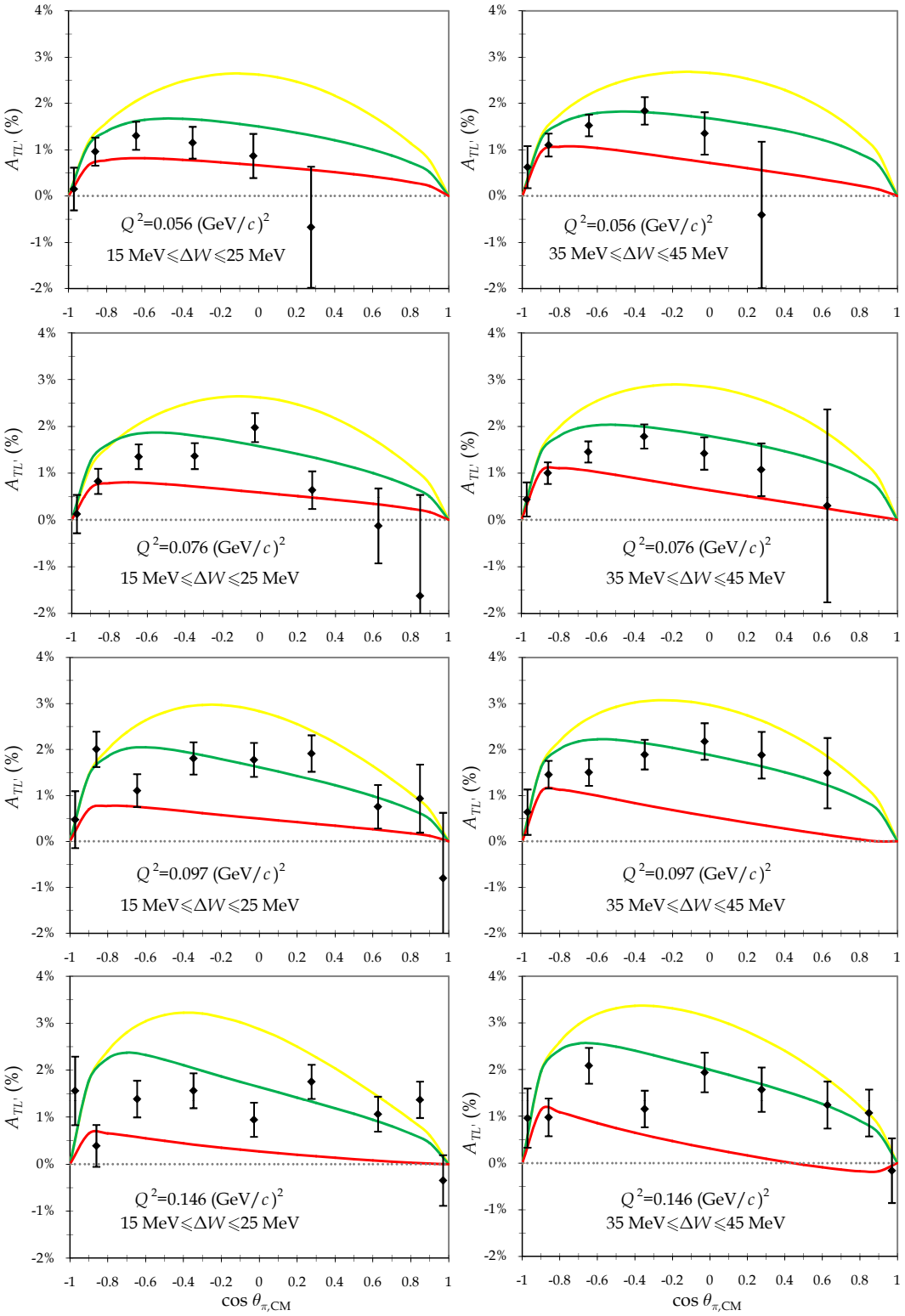

Figure 4.5: $\theta_{\pi,\mathrm{CM}}$ distribution of asymmetry for ϕ_{CM} integrated over $[20°, 120°]$: same as in Fig. 4.3.

Table 4.4: The present experimental values of asymmetry at various Q^2s tabulated against $\theta_{\pi,\mathrm{CM}}$ for the $\Delta W = 20$ MeV bin (15 MeV $\leq \Delta W \leq$ 25 MeV) and ϕ_{CM} integrated over $[20°, 120°]$.

	$Q^2 = 0.056(\mathrm{GeV}/c)^2$		$Q^2 = 0.076(\mathrm{GeV}/c)^2$		$Q^2 = 0.097(\mathrm{GeV}/c)^2$		$Q^2 = 0.146(\mathrm{GeV}/c)^2$	
$\theta_{\pi,\mathrm{CM}}$ (deg.)	$A_{TL'}$	$\pm\,\delta A_{TL'}$	$A_{TL'}$	$\pm\,\delta A_{TL'}$	$A_{TL'}$	$\pm\,\delta A_{TL'}$	$A_{TL'}$	$\pm\,\delta A_{TL'}$
14.0					-0.008	0.014	-0.003	0.005
32.0			-0.016	0.022	0.009	0.007	0.014	0.004
51.2			-0.001	0.008	0.008	0.005	0.011	0.004
74.0	-0.007	0.013	0.006	0.004	0.019	0.004	0.018	0.004
91.6	0.009	0.005	0.020	0.003	0.018	0.004	0.009	0.004
110.4	0.012	0.003	0.014	0.003	0.018	0.004	0.016	0.004
130.2	0.013	0.003	0.014	0.003	0.011	0.004	0.014	0.004
149.4	0.010	0.003	0.008	0.003	0.020	0.004	0.004	0.004
166.7	0.002	0.005	0.001	0.004	0.005	0.006	0.016	0.007

its agreement with experimental cross section (as a function of ΔW). One conclusion, however, can be made easily. Since DMT and MAID models both provide the unpolarized cross section[8] $\sigma_0 = \sigma_T + \epsilon_L \sigma_L$ which is in agreement with experiment (see Fig. 4.4), they must differ in $R_{TL'}$ and R_{TT} structure function values to have given such two very different predictions for the asymmetry. This is obvious by looking at asymmetry's definition (at $\phi_{\mathrm{CM}} = 90°$) once more, i.e.,

$$A_{TL'}(\theta_{\pi,\mathrm{CM}}) = \left.\frac{\sigma^+(\theta_{\pi,\mathrm{CM}}) - \sigma^-(\theta_{\pi,\mathrm{CM}})}{\sigma^+(\theta_{\pi,\mathrm{CM}}) + \sigma^-(\theta_{\pi,\mathrm{CM}})}\right|_{\phi_{\mathrm{CM}}=90°} = \frac{\sqrt{2\epsilon_L(1-\epsilon)}R_{TL'}}{R_T + \epsilon_L R_L - \epsilon R_{TT}} \,. \tag{4.11}$$

Looking at the above equation, one sees the unpolarized cross section $\sigma_0 = \sigma_T + \epsilon_L \sigma_L$, for which MAID and DMT seem to agree with experiment equally, is present in the denominator of $A_{TL'}$ asymmetry[9]. The difference between the two models must have resulted in different values for $R_{TL'}$ and R_{TT} structure functions.

[8]Note that as we mentioned in section 1.1.2, the alternative notation σ_i with $i = T, L, TT, TL, TL'$ is used for the virtual photon cross sections $d\sigma_i/d\Omega_{\pi,\mathrm{CM}}$ of Eq. 1.20. The σ_0 is just the sum of the first two terms in the cross section of Eq. 1.19.

[9]Let us remind ourselves, that the structure functions R_i are related to the virtual photon cross sections σ_i according to Eq. 1.20.

Table 4.5: The present experimental values of asymmetry at various Q^2s tabulated against $\theta_{\pi,\mathrm{CM}}$ for the ΔW = 40 MeV bin (35 MeV $\leq \Delta W \leq$ 45 MeV) and ϕ_{CM} integrated over [20°, 120°].

	Q^2 = 0.056(GeV/c)^2		Q^2 = 0.076(GeV/c)^2		Q^2 = 0.097(GeV/c)^2		Q^2 = 0.146(GeV/c)^2	
$\theta_{\pi,\mathrm{CM}}$ (deg.)	$A_{TL'}$	$\pm\,\delta A_{TL'}$	$A_{TL'}$	$\pm\,\delta A_{TL'}$	$A_{TL'}$	$\pm\,\delta A_{TL'}$	$A_{TL'}$	$\pm\,\delta A_{TL'}$
14.0							-0.002	0.007
32.0							0.011	0.005
51.2			0.003	0.021	0.015	0.008	0.012	0.005
74.0	-0.004	0.016	0.011	0.019	0.025	0.005	0.016	0.005
91.6	0.014	0.005	0.014	0.022	0.025	0.004	0.019	0.004
110.4	0.018	0.003	0.018	0.003	0.019	0.003	0.012	0.004
130.2	0.0155	0.002	0.015	0.002	0.015	0.003	0.021	0.004
149.4	0.011	0.002	0.010	0.002	0.015	0.003	0.010	0.004
166.7	0.006	0.005	0.004	0.004	0.006	0.005	0.010	0.006

If we define the asymmetry at ϕ_{CM} = const. $\neq 90°$, the asymmetry takes the form

$$\begin{aligned} A_{TL'}(\theta_{\pi,\mathrm{CM}}) &= \left.\frac{\sigma^+(\theta_{\pi,\mathrm{CM}}) - \sigma^-(\theta_{\pi,\mathrm{CM}})}{\sigma^+(\theta_{\pi,\mathrm{CM}}) + \sigma^-(\theta_{\pi,\mathrm{CM}})}\right|_{\phi_{\mathrm{CM}}=\mathrm{const.}} \\ &= \frac{\sqrt{2\epsilon_L(1-\epsilon)}\sin\phi_{\mathrm{CM}} R_{TL'}}{R_T + \epsilon_L R_L + \sqrt{2\epsilon_L(1+\epsilon)}\cos\phi_{\mathrm{CM}} R_{TL} + \epsilon\cos 2\phi_{\mathrm{CM}} R_{TT}}\,, \end{aligned} \tag{4.12}$$

where R_{TL} structure function is additionally involved. In this case, a possible difference in R_{TL} of MAID and DMT needs to be considered, which will add to the complication as why the two models give different asymmetry values.

In Fig. 4.6 we display the virtual photon cross sections TL, TT, and TL' of MAID and DMT versus ΔW at two Q^2s, the lowest and the highest of the presented data. The comparison shows that the two models do not agree with each other in none of the virtual photon cross sections, as we suspected. The disagreement and even the shapes of the virtual photon cross sections are exactly the same for the two intermediate Q^2s, 0.076 and 0.097 (GeV/c)^2. For that reason and to avoid repetition, we do not show the comparisons for those two Q^2s. The differences between the structure functions originate from the multipoles involved. However, comparing the multipoles do not reveal anything unless we know the diagrams or transition matrix elements involved in the evaluations of each multipole in the framework of both models. This requires a meticulous theoretical analysis to spot the sources of disparity within the models, which is outside the scope of this thesis.

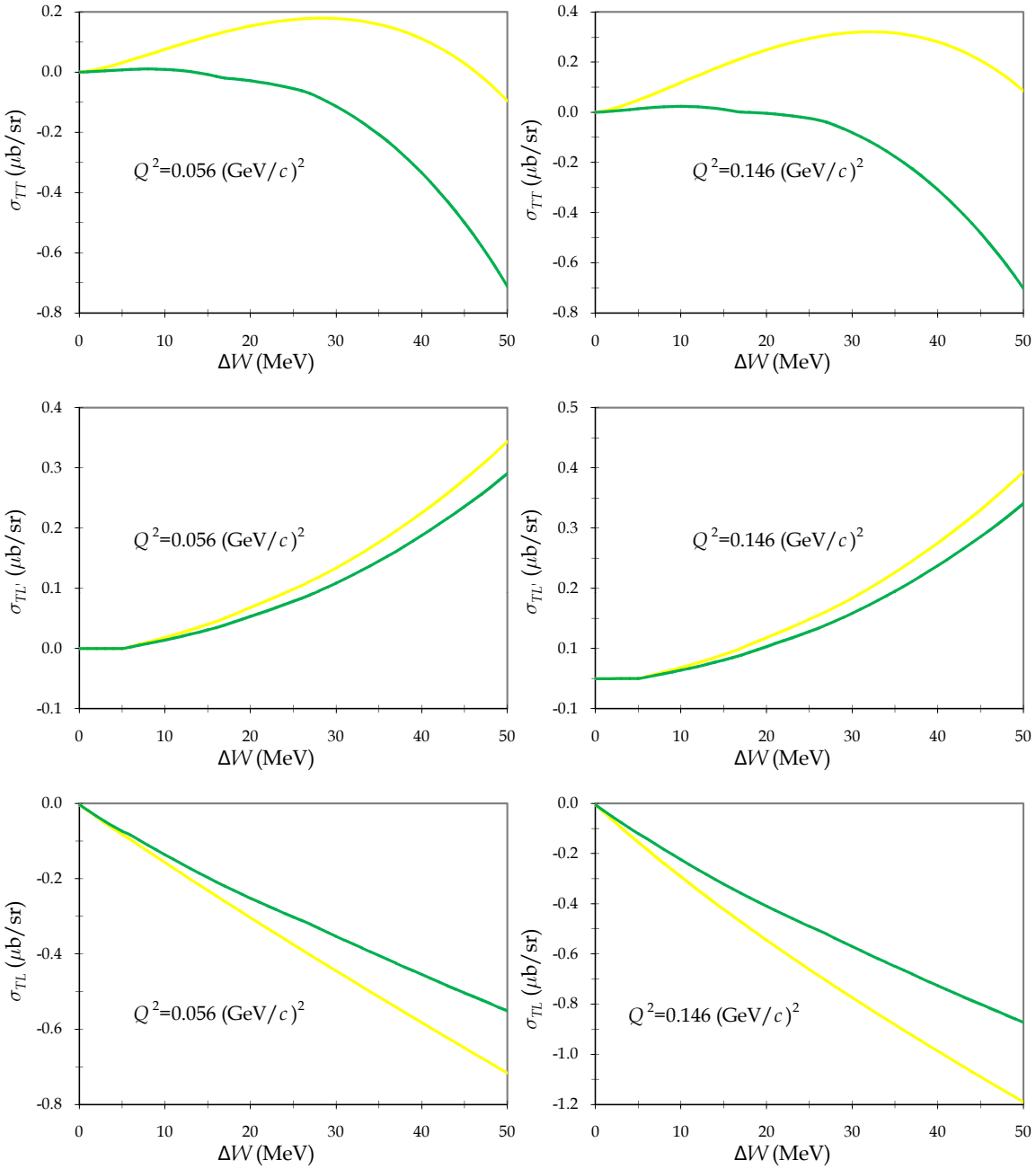

Figure 4.6: Virtual photon cross sections of MAID and DMT at Q^2 = 0.056 and 0.146 (GeV/c)^2 for $\theta_{\pi,\mathrm{CM}}$ = 90°: green line, DMT model [39]; yellow line, MAID model [38].

As why MAID and DMT do not agree on $\theta_{\pi,\mathrm{CM}}$ distribution of asymmetry, one cannot be easily exclusive. This is because the $\theta_{\pi,\mathrm{CM}}$ dependence of the cross section is fairly distributed amongst all structure functions[10]. Therefore, the $\theta_{\pi,\mathrm{CM}}$ dependence of asymmetry cannot simply be traced to a specific structure function. This inconclusiveness can be better understood if we once again look at the comparisons of MAID's unpolarized cross sections with the data from the second MAMI experiment [56] where the angular dependence of σ_0 is presented (in Fig. 1.6). MAID predictions for $\theta_{\pi,\mathrm{CM}}$ dependence of σ_0, which only depends on σ_T and σ_L, are not in good agreement with experiment. That means unlike the ΔW dependence case, we cannot easily isolate a few structure functions and seek the source of disparity, in the $\theta_{\pi,\mathrm{CM}}$ dependence, amongst them. For the MAID model the $\theta_{\pi,\mathrm{CM}}$ distribution disagreements with experiment in σ_0 and asymmetry data means that all structure functions play roles in the discrepancies.

Therefore, when comparing MAID and DMT we cannot be definitive on which of the structure functions may be the origin of the disparity. This is because, the $\theta_{\pi,\mathrm{CM}}$ dependence of asymmetry is a complicated matter depending on different multipoles, which appears through all structure functions. A thorough analysis of multipoles and their role in the $\theta_{\pi,\mathrm{CM}}$ dependence of asymmetry is a theoretical undertaking, which is outside the scope of this thesis.

However, there maybe a phenomenological reason for the differences we have observed between the predictions of TL' asymmetry provided by MAID and DMT models. If written in terms of multipoles, TL' asymmetry consists of different combinations of multipols compared of those in unpolarized cross section expression. The reason MAID and DMT are close in their predictions for unpolarized cross section, σ_0, might be that these phenomenological models have tuned some of the multipole combinations of the cross section expression to the experimental data, for some time. Asymmetry expression shares some of those multipole combinations with σ_0, but there are other combinations which perhaps have been tuned to experiment since the first experimental data on asymmetry became available not so long ago.

[10] To see this, one needs to look at the multipole decompositions of structure functions R_i. See the Appendix B of Ref. [9]

Conclusion

We have provided TL' asymmetry data at $Q^2 = 0.056, 0.076, 0.097$ and 0.146 $(\mathrm{GeV}/c)^2$ in terms of ΔW, and $\theta_{\pi,\mathrm{CM}}$, and ϕ_{CM}. The experimental data on the angular distribution of TL' asymmetry are the first of its kind, while the Q^2s at which the data are provided are new additions to the body of the data.

The overall amplitude of our asymmetry data (at $Q^2 = 0.056$ $(\mathrm{GeV}/c)^2$ against ΔW) is close to that of the third MAMI experiment [61] at $Q^2 = 0.05$ $(\mathrm{GeV}/c)^2$. Furthermore, the present JLab data at $Q^2 = 0.056$ $(\mathrm{GeV}/c)^2$ seem to agree with the general observation of the Mainz data; that the experimental asymmetry values are considerably smaller than MAID's predictions.

Since we have four Q^2 settings and provide $\theta_{\pi,\mathrm{CM}}$ dependence of asymmetry in addition to ΔW dependence, we observe some interesting trends. The data in terms of ΔW seem to indicate that

- Experimental data agree with the HBChPT prediction at $Q^2 = 0.056$ and 0.076 $(\mathrm{GeV}/c)^2$ toward the threshold for $\Delta W < 30$ MeV and $\Delta W < 20$ MeV, respectively. In both cases, DMT model is closer to experiment further away from the threshold.

- The span of HBChPT agreement with experiment near threshold shrinks to $\Delta W \leq 5$ MeV region as Q^2 increases. DMT model is generally in better agreement with experiment at higher Q^2s.

- MAID's predictions are consistently larger than the experimental data at $Q^2 = 0.056, 0.076,$ 0.097 $(\mathrm{GeV}/c)^2$ except for the region below the $\pi^+ n$ threshold ($\Delta W \leq 5.9$ MeV), where errors are large. This is also true for MAID's predictions when compared to the theoretical values of DMT and HBChPT. At $Q^2 = 0.146$ $(\mathrm{GeV}/c)^2$, MAID's predictions are within experimental error bars up to $\Delta W = 15$ MeV.

The data in terms of $\theta_{\pi,\mathrm{CM}}$ seem to indicate that

- The data at $Q^2 = 0.056$ (GeV/c)^2 and for the $\Delta W = 20$ MeV bin agree with the HBChPT predictions for most angles, within experimental errors.
- Except the above case, HBChPT underestimates the experimental data at various higher Q^2s for most angles.
- MAID model generally overestimates the experiment.
- The DMT model's angular distribution of asymmetry has a mixed comparison with the present data, but it is in better overall agreement with experiment compared to MAID and HBChPT.

At the end, one can say that the discrepancy between ChPT and experimental data of Ref. [61] at $Q^2 = 0.05$ (GeV/c)^2 is improved in favour of ChPT through the present data at $Q^2 = 0.056$ (GeV/c)^2, at least for $\Delta W < 30$ MeV[11]. In the same region, $\Delta W < 30$ MeV, the agreement of DMT and experimental data of Ref. [61] also seemed to have been weakened through the present data. Further away from threshold, however, ChPT still disagrees with experiment at $Q^2 = 0.056$ (GeV/c)^2 and DMT agrees with it.

[11] This is because the two Q^2s are only 0.006 (GeV/c)^2 apart.

Appendix A

The Geometry of Scattering and Reaction Planes

In this Appendix, we define the scattering and reaction planes depicted in Fig. A.1 and the out of plane angle ϕ. The following definitions are all expressed in terms of Lab frame quantities. The definitions in Hadronic CM frame can be obtained by replacing the corresponding three-momenta and angles with their CM counterparts.

- **Scattering Plane**: The scattering plane is defined by the three-momenta of the incoming and outgoing electrons. That means the normal to the plane is simply

$$\hat{n}_S = \frac{\hat{k} \times \hat{k}'}{\sin\theta_e} \,. \tag{A.1a}$$

  Therefore, the unit vectors of the coordinate system shown in Fig. A.1 are

$$\hat{x} = \hat{y} \times \hat{z} = \hat{y} \times \hat{q} \,, \tag{A.1b}$$

$$\hat{y} = \frac{\mathbf{k} \times \mathbf{k}'}{|\mathbf{k}|\,|\mathbf{k}'|\sin\theta_e} = \frac{\hat{k} \times \hat{k}'}{\sin\theta_e} \,, \tag{A.1c}$$

$$\hat{z} = \hat{q} \,. \tag{A.1d}$$

  That means the virtual photons three-momentum vector in this coordinate system is $\mathbf{q} = \left(0, 0, |\mathbf{q}|\right)$.

- **Reaction Plane**: The reaction plane is defined by the three-momenta of the virtual photon $\hat{q} = (0, 0, 1)$ and the three-momentum of the pion $\hat{p}_\pi = \left(\sin\theta_\pi \cos\phi, \sin\theta_\pi \sin\phi, \cos\theta_\pi\right)$

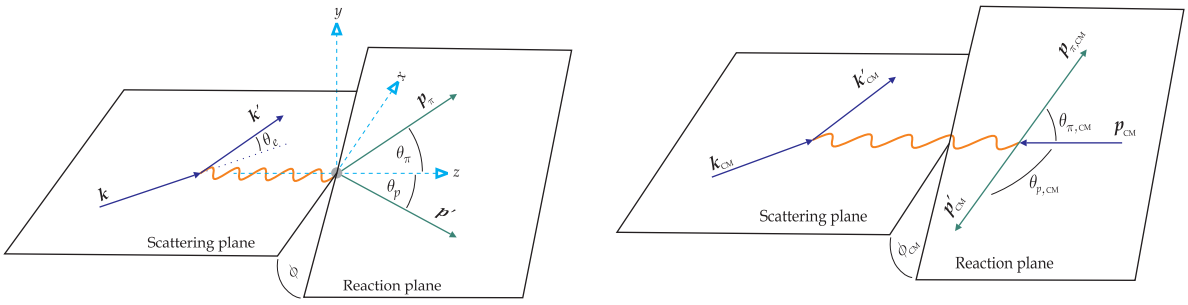

Lab frame π-N CM frame

Figure A.1: The depiction of the scattering and reaction planes: in Lab frame and in pion-nucleon center-of-momentum frame. Note that the momemta are all three-vectors and the scattering plane is defined by the momenta of incoming and outgoing electrons, which is the $x-z$ plane in the lab frame.

or equivalently the three-momentum of the recoiled proton. The normal to the plane is given by

$$\hat{n}_R = \frac{\hat{q} \times \hat{p}_\pi}{\sin\theta_\pi} = \Big(\sin\phi, -\cos\phi, 0\Big), \tag{A.2}$$

where the components are given in the coordinate system defined by the unit vectors of Eqs. A.1b.

The out of plane angle ϕ is the angle between the two unit vectors $\hat{n}_S$ and $\hat{n}_R$.

Appendix B

Lab and Hadronic CM Frames

The definitions of lab and hadronic CM frames along with the transformation of physical observables between the two frames are discussed here.

B.1 The Definitions of Lab and CM Frames

The lab observer sees two initial particles: an incoming electron, which scatters off a stationary proton (see Figs. A.1 and B.1). This results in three final particles: a scattered electron, a recoiled proton and a neutral pion. While the scattered electron stays in the same plane as incoming electron (scattering plane), the hadronic final particles happen to go off in a different plane (reaction plane) which makes an angle ϕ (out of plane angle) with scattering plane. In lab frame the virtual photon propagates along the z axis, which is the intersection of the two planes.

The CM observer sees an incoming electron, which scatters off a moving proton through the exchange of a virtual photon (see Figs. A.1 and B.1). In the CM frame, the virtual photon and incoming proton move toward each other with the same three momentum along the z-axis, which is the intersection of scattering and reaction planes. According to the CM observer, the scattered electron and incoming electron form the scattering plane and the recoiled proton and produced neutral pion move in opposite directions (with the same three momentum) in the reaction plane.

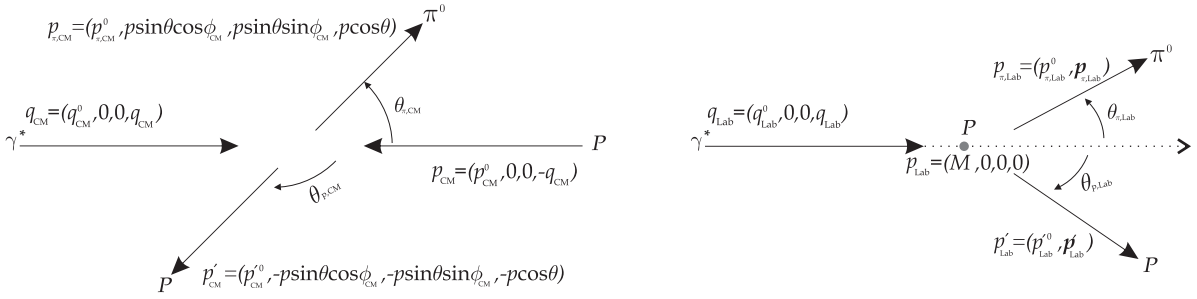

Figure B.1: The kinematics in hadronic CM frame (left) and lab frame (right).

B.2 The Transformation Between Lab and CM Frames

The lab and CM observers move with respect to each other at some speed along the z axis. Their observations are therefore transformed into those of the other observer through Lorentz transformation (boost only). The transformation of any four vector A^μ measured in lab frame to CM frame is given by

$$A^0_{\mathrm{CM}} = \gamma\left(A^0_{\mathrm{lab}} - \boldsymbol{\beta}\cdot\mathbf{A}_{\mathrm{lab}}\right), \tag{B.1a}$$

$$A_{\parallel\mathrm{CM}} = \gamma\left(A_{\parallel\mathrm{lab}} - \beta A^0_{\mathrm{lab}}\right), \tag{B.1b}$$

$$\mathbf{A}_{\mathrm{CM}\perp} = \mathbf{A}_{\mathrm{lab}\perp}, \tag{B.1c}$$

where

$$\boldsymbol{\beta} = \beta\hat{z} = \frac{|\mathbf{q}|}{k^0 - k'^0 + M}\hat{z}, \tag{B.2a}$$

$$\gamma = \frac{k^0 - k'^0 + M}{W}, \tag{B.2b}$$

and $A_\parallel$ and $A_\perp$ are the components of $\mathbf{A}$ along and perpendicular to z axis (the direction of $\boldsymbol{\beta}$), respectively. The same transformations (Eqs. B.1) can be applied for going from CM to lab, however one must note that the direction of $\boldsymbol{\beta}$ is reversed in that case. Even though β and γ in Eqs. B.2 are expressed in terms of lab-frame-measured quantities that are not Lorentz invariant, the values are the same as those measured by the CM observer, since they refer to the relative velocity on which both observers agree.

Appendix C

Multi-Wire Drift Chambers

The detailed procedure for construction of multi-wire drift chambers is presented in this Appendix.

Multi-Wire Proportional Counters (MWPC), which were first introduced by Charpak (1968, 1970) at CERN, can be considered as the ancestors of the **horizontal drift chambers**, also known as Multi-Wire Drift Chambers (MWDC).

A MWDC consists of many parallel field and signal wires stretched in a plane between two cathode planes. The space between wires and cathode planes are filled with a gas mixture. The wires are maintained at a potential of a few kV. Charged particles passing through the gas ionize the gas atoms in their paths and the so-released electrons drift to the signal wires. The electric field strength around the thin signal wires is very high, so the primary electrons are accelerated and reach kinetic energies such that they themselves start to ionize the gas atoms. This results in a charge avalanche, which creates a cloud of electrons moving towards the wire. The approach of this electron cloud induces a measurable voltage pulse on the wire. The arrival time of the pulse is registered electronically. The known position of the wire tells us where the particle passed by. To achieve a good resolution over large areas, an enormous number of wires together with amplifiers are required.

A set-of-three precision MWDCs was constructed at the University of Virginia (UVA) for the BigBite spectrometer. These multi-wire drift chambers were designed to provide high rate capabilities, high resolution, as well as unambiguous track reconstruction. The chambers operate in a high-rate background environment while at the same time provide a good spatial resolution. They are able to detect high energy electrons as well as low energy hadrons.

Figure C.1: Cathode and wire planes before assembling the drift chambers.

The constituents of each wire chamber are

- Wire-planes.
- Cathode-planes.
- Gas-planes.
- End-plates.
- Transport support.

The wire-planes and cathode-planes on alternating layers are sandwiched between two gas-planes. The gas, cathode, and wire frames are prefabricated printed circuit boards (PCBs) made of G10/FR4 material, etched with copper. The space between wires and cathode planes are filled with a gas mixture. Two 9.5 mm thick aluminium end-plates are bolted down on both sides of the chamber to provide support and mechanical rigidity. (see Figs. C.1 and C.2.) The properties of multi-wire drift chambers are summarized in C.2.

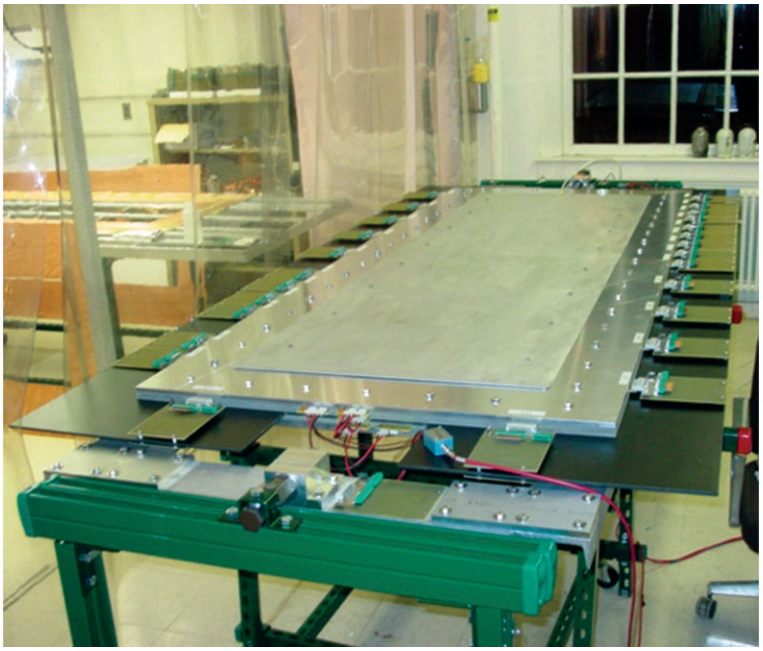

Figure C.2: A complete multi-wire drift chamber .

C.1 Wire Planes

There are six wire-planes in each wire chamber. Each chamber has wires in three different directions (U, V, X) to precisely measure track coordinates and angles. By convention (when chambers are positioned as shown in Fig. 2.17) the direction of increasing x is taken to be along the dispersive direction of the spectrometer (direction of increasing momentum) in other words, x points towards the ground. The z axis is taken to point perpendicular to the wire planes along the direction of the central ray of the spectrometer, and the y axis is taken so that the $\hat{x}, \hat{y}, \hat{z}$ axes form a right handed orthogonal coordinate system. The V(U) wires are at an angle of $60°(-60°)$ relative to the x-axis, while the X wires are perpendicular to the x-axis.The configuration of planes and wires for both chambers is shown in Fig. C.3.

The dimensions of the active area for the smaller chamber, is 35 cm$\times$ 140 cm. It contains 141 signal wires for each of U and V planes, and 142 wires for the X plane. The larger chamber has an active area of 50 cm $\times$ 200 cm, with 200 signal wires for the U (V) plane and 202 wires for the X plane. Each signal wire has its own dedicated electronic output channel (preamp, discriminator, and TDC) whereas the field wires all are connected to a common channel for high voltage connection. See Figs. C.7.

Two different type of wires were used for the wire-planes in drift chambers. Each wire frame

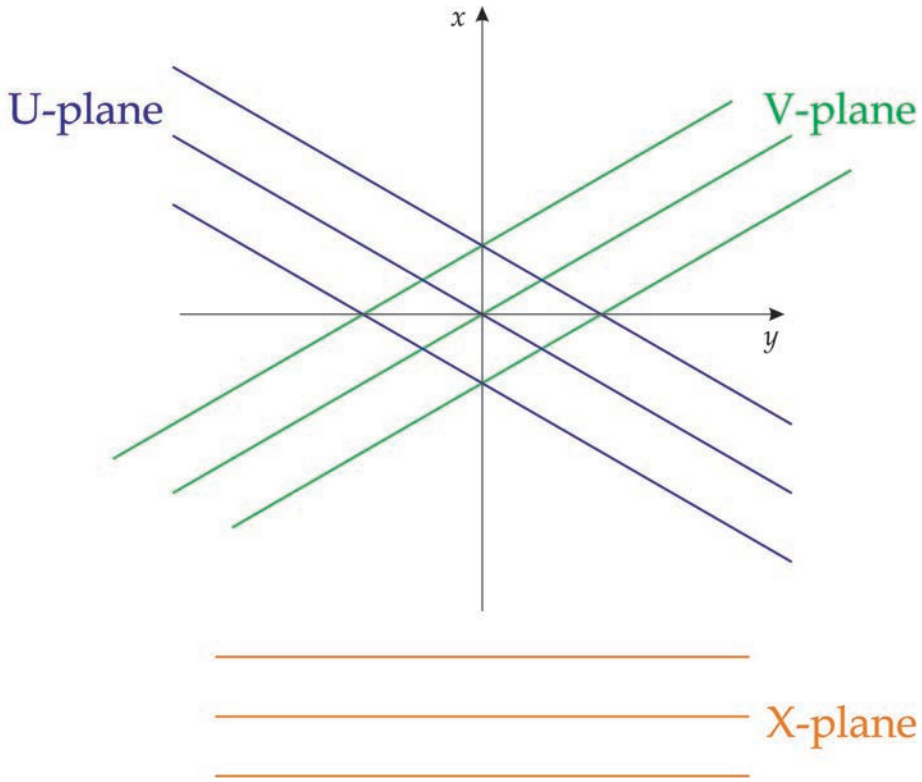

Figure C.3: Orientation of the wires in the wire chambers.

consists of alternately strung field and signal wires spaced 5 mm apart. The sense wires are 25 μm diameter gold-plated tungsten and the field wires are 90 μm diameter copper-beryllium (98.1% Cu, 1.8%Be). A balance should be struck between the desire for high tension to avoid large displacements under the electrostatic forces existing between the wires during operation and the necessity to avoid permanent deformation of the wire due to too much tension. The field wires have a quoted yield tensile strength of 200,614 MPa corresponding to permanent deformation due to a weight of more than 5 kg. A weight of 70 g was chosen in order to avoid undue stress on the frame itself. The more fragile signal wires are deformed by a weight of around 100 grams. To prevent the wire from snapping under extreme field conditions, the signal wires were chosen to have a tension of 40 grams.(see Table C.1).

C.1.1 Wire Stringing

An aluminium frame was used for precise positioning of the wires on their frames. This frame consists of an aluminium baseplate (used to support and align the wire frame) and two removable rails on either side of the wire frame. The rails are shown in Fig. C.4 (right) and

Table C.1: The specifications of wires in drift chambers.

	Field wires	Signal wires
Mass density	$5.35 \times 10^{-5}(kg \cdot m^{-1})$	$6.036 \times 10^{-6}(\frac{\text{kg}}{\text{m}})$
Wire's diameter	90 (μm)	25 (μm)
Hanging mass	77.3 (gr)	46.2 (gr)
Nominal Tension	0.757 (N)	0.453 (N)

Figure C.4: Stringing wires (left) and close-up of aluminium jig for X plane (right). The wires are threaded underneath the screws and over the horizontal rod where the weight is then applied.

contain two rows of guide pins and two rows of screws. Each wire was initially secured to the rail by a screw, then was run around the guide pin and across the wire frame to the second rail. It was positioned around the guide pin on the second rail and underneath the screw, which was left loose. Once tension was applied to the wire, this screw was fastened down and the wire remained under tension and properly positioned (see Fig. C.4.)

C.1.2 Wire Tension Measurement

Tension measurement of sense and field wires are crucial since they have to be mechanically stable in the presence of high electric fields. Tension less than desired will cause the wire to sag which destroys the uniformity of the field throughout the chamber between the wires and between the wire and the cathode plane. Since the electric field depends on the inter-wire and wire to cathode frame spacing, a small change in wire spacing will disturb the field lines and

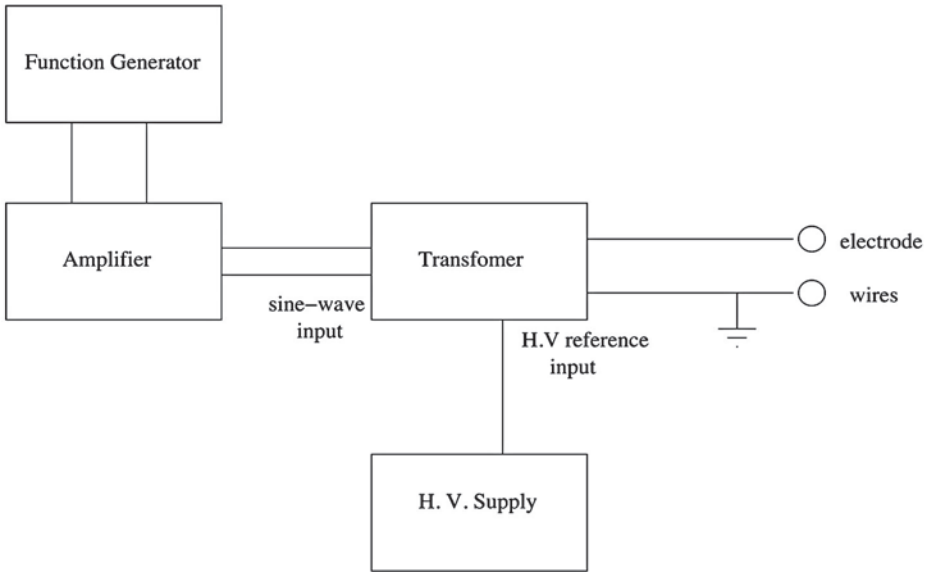

Figure C.5: Layout for tension measurement

can skew the drift time measurements. Care also must be taken not to make the wires too taut. Under conditions of high electric field, a slight attraction of the wires to either each other or the cathode plane will cause the wire to snap.

After the stringing of each frame the wires' tension and position were checked before the wires were permanently attached (glued down with epoxy and soldered) to the fame. The wire tensions were measured by grounding all the wires and the frame and placing an electrode, under high voltage, across the wire frame (Fig. C.5).

An AC high-voltage from a function generator was applied to the wires. The wire oscillates due to the alternating electrostatic force. The frequency of the function generator was tuned until the amplitude of the oscillations increased at resonance. The oscillations were observed visually for each wire and noted the resonance frequency, f. Since the length of wire is known the tension can be calculated using

$$T = (2Lf)^2\mu \tag{C.1}$$

L is the length of the wire in the active region and μ is the linear mass density of the wire.

The specifications of *field* and *signal* wires are given in Table C.1.

C.1.3 Wire Position Measurement

After measuring the frequencies (tensions), the next step was securing the wires onto the plane using an epoxy adhesive, Araldite 2011. A small drop ($\approx$ 5 mm) of the resin/hardener mixture

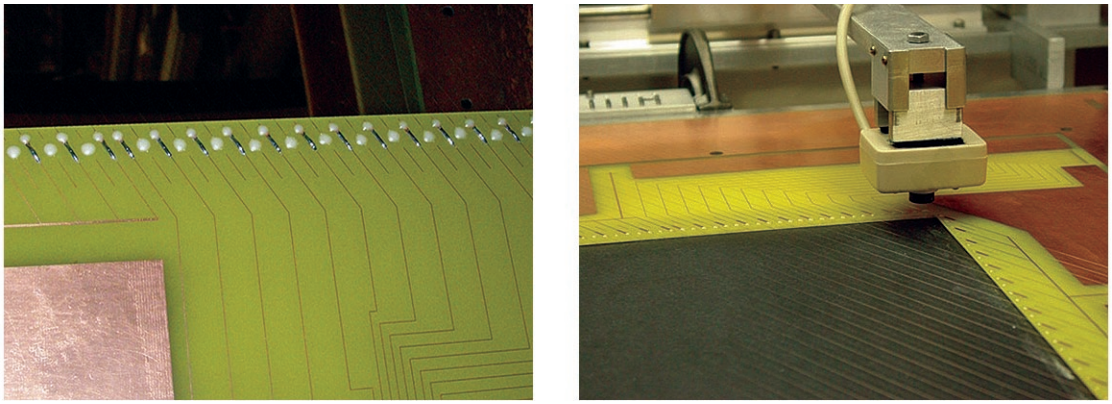

Figure C.6: Epoxy glue placed on the frame to secure the wires (left) and camera overlooking the frame to measure the wire spacing (right).

was placed on the wire between the edge of the active window and the copper contact pads. (Fig. C.6). It takes about a day for the glue mixture to completely harden. Before the epoxy hardens, the wire position is measured so that they can be corrected if necessary.

Measuring the position of the wires over about two meters long to a precision better than 75μm proved to be challenging. To measure the wire position without disturbing the wires an optical device, a CCD camera attached to a stepper motor, was used. The stepper motor was controlled by a computer through a serial interface. The camera was attached to a long arm and overlooked each wire displaying a magnified image on a monitor.(Fig. C.6). The stepper motor has a precision of 0.5μm. The resolution of the camera, however, cannot discern this and the overall accuracy of this measuring device was determined to be $\simeq$ 35μm. The allowed tolerance was $\pm$75μm.

C.2 Cathode-planes

The Cathode-planes provide high voltage to the chamber to help to shape the electric field. The film used to provide the high voltage was copper (1200 Å) coated DuPont Mylar 13μm (0.5 mil) from Sheldahl. High voltage cathode planes were produced by stretching copper-coated film across the central gap in the PCB. The film is coated on both sides with the conductor and serves simultaneously as the cathode for the wires on either side of the plane. The foil is glued to the board with the Araldite epoxy and stable electrical contact with the copper traces was created using conductive epoxy.

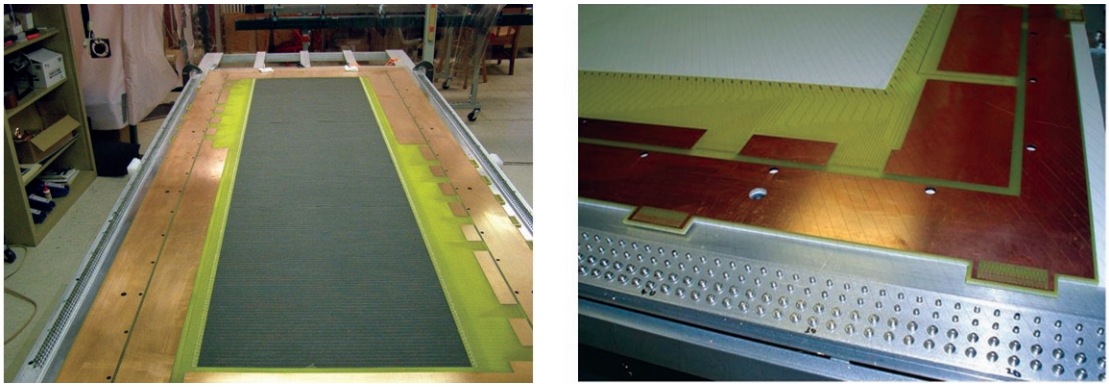

Figure C.7: Wire-plane (left) and wire-plane close-up (right) showing the wires and electrical connections on the circuit board.

C.3 Gas-planes

The gas-planes are made of a 1 mil aluminized kapton foil. Foil was stretched over the gas frames and glued down with epoxy. The procedure of stretching is similar to that of the cathode planes.

There are several factors, which determine the choice of filling gas of the chamber, such as low working voltage, high gain, good proportionality and high rate capability. In general, these conditions are met by using a gas mixture rather than a pure gas. For a minimum working voltage, noble gases are usually chosen since they require the lowest electric field intensities for avalanche formation.The gas mixture for a drift chamber is typically chosen to have a primary gas usually a noble gas responsible for the ionization and a secondary polyatomic gas to increase the gain [66]. The transport properties of the Argon-Ethane mixture (50% Argon and 50% ethane) in this chambers are very well-suited to the detection of charged-particle tracks in BigBite, hence during the E04-007 experiment, chambers were filled with Argon,-Ethane gas mixture bubbled through 0° ethyl alcohol. The chamber pressure was slightly above atmospheric pressure.

C.4 End-plates

The mechanical rigidity of the chamber is provided by two aluminium plates, one at the top and one at the bottom of the chamber, with matching the active area of the chamber. The thickness of these frames is approximately 1 cm. The gas sealing of the chambers was achieved by using viton o-rings of 1.8 mm diameters in groves of 1.25mm depth.

Table C.2: Multiwire Drift Chambers for BigBite Spectrometer

Properties	MWDC (1)	MWDC (2 & 3)
Sensitive area	35×140 cm^2	50×200 cm^2
Number of Anode Planes	6	6
Number of Cathode Planes	8	8
Anode-Anode wire spacing	10 mm	10 mm
Field-Field wire spacing	10 mm	10 mm
Anode-Field wire spacing	5 mm	5 mm
Anode-Cathode spacing	3.175 mm	3.175 mm
Number of Anode wires	848	1204
Number of Fild wires	848	1204
Anode wire material	25 μm gold-plated tungsten	25 μm gold-plated tungsten
Field wire material	90 μm Cu-Be	90 μm Cu-Be
Cathode material	12.7 μm Cu-coated mylar	12.7 μm Cu-coated mylar
Gas window material	25.4 μm aluminized kapton	25.4 μm aluminized kapton
Gas Mixture	Argon/ethane	Argon/ethane

Appendix D

Survey Results for BigBite and HRS

Jefferson Lab Alignment Group

Data Transmittal

TO: J.P. Chen, J. Gomez, J. LeRose		**DATE:** 12 Feb 2008
FROM: J. Dahlberg	**Checked:** kjt	**# :** A1156

DETAILS:

Data: 2b\HallA\Electronslit\060703a, Hadronslit\060703a
2b\HallA\Target\2008\080208a

Below are the results from the left and right spectrometer collimator surveys carried out on the 3rd of July, 2006, and the 8th of February, 2008. The coordinates are given in millimeters and degrees relative to the Ideal hall A target and beamline, with +Z along the beam, +X to the beam left, and +Y up. Measurements are to the upstream face of the collimators.

JULY 3RD 2006 SURVEY

LOCATION	Z	X	Y	YAW ANGLE	3D DIST
Left arm sieve slit	357.72	1109.13	-0.12	72.124	1165.39
Left arm 6Msr	335.89	1038.08	0.05	72.070	1091.08
Right arm sieve slit	994.57	-657.87	-0.15	-33.483	1192.46
Right arm 6Msr	933.01	-615.17	-0.18	-33.398	1117.56

FEBRUARY 8TH 2008 SURVEY

LOCATION	Z	X	Y	YAW ANGLE	3D DIST
Left arm sieve slit	948.05	677.59	2.05	35.554	1165.30
Left arm 6Msr	888.31	633.35	2.53	35.488	1090.98

Jefferson Lab Alignment Group

Data Transmittal

TO: J. P. Chen, J. LeRose, J. Segal, D. Higinbotham		**DATE:** 26 Jun 2008
FROM: J. Dahlberg	**Checked:** kt	**# :** A1170

DETAILS:

Data: Step2b\HallA\BigBite_Detector\080626A

Below are the results from the survey performed on the BigBite hadron detector package. The first set of coordinates (in millimeters) is based on the ideal Hall A target center and straight ahead beam. The second set is based on the nominal rotation angle of -48 degrees from the straight ahead beam and pitched 25 degrees. A +X is to the beam left, a +Z is downstream, and a +Y is up. The coordinate for each fiducial point is relative to the center of the survey target placed in each fiducial block. The survey target is 7.9 mm in height (standard center of tooling ball). The points on the detectors are to corner points on the detector frame. The perpendicular distance between the downstream faces of detector C1 and C2 is 764.03 mm. Note that the detector coordinates are derived from fiducial locations surveyed on March 31st 2008 (DT#1164). The detector package may not have been in the final running position at that time.

FID / DET POINT	Z	X	Y
HABBDTA	1747.6	-3387.1	-181.4
HABBDTB	2685.3	-2717.4	-182.8
HABBDTC	2157.0	-2454.6	921.0
HABBDTD	1668.8	-2806.4	917.2
HABBDTE	1213.6	-2641.4	1759.9
HABBDTF	2149.7	-1971.7	1758.5
C1_BOTR	1167.5	-2315.3	-434.6
C1_BOTL	1826.3	-1839.3	-434.5
C1_TOPL	1368.1	-1204.9	1225.6
C1_TOPR	708.9	-1681.1	1225.5
C2_BOTR	1590.1	-3007.0	-363.6
C2_TOPR	987.7	-2170.0	1825.4
C2_TOPL	1777.8	-1605.0	1826.6
C2_BOTL	2380.2	-2441.9	-362.2

FID / DET POINT	Z	X	Y	ROTATED -48° PITCHED 25°
HABBDTA	3264.5	-967.7	-1722.4	
HABBDTB	3381.4	177.3	-1778.4	
HABBDTC	3350.5	-39.5	-546.2	
HABBDTD	3289.8	-637.6	-522.0	
HABBDTE	3258.8	-865.6	422.2	
HABBDTF	3374.8	278.2	366.6	
C1_BOTR	2083.7	-681.6	-1451.2	
C1_BOTL	2162.7	126.5	-1487.9	
C1_TOPL	2159.1	210.5	345.5	
C1_TOPR	2080.0	-598.0	382.2	
C2_BOTR	2835.9	-830.4	-1723.6	
C2_TOPR	2831.9	-718.0	693.6	
C2_TOPL	2931.1	247.2	648.6	
C2_BOTL	2935.0	134.9	-1768.3	

Appendix E

Møller measurements Results

To determine the beam polarization Møller measurements were carried out on April 8, 2008 and April 11, 2008. The Møller measurements resulted in 67% polarization. The results are shown in Fig. E.1.

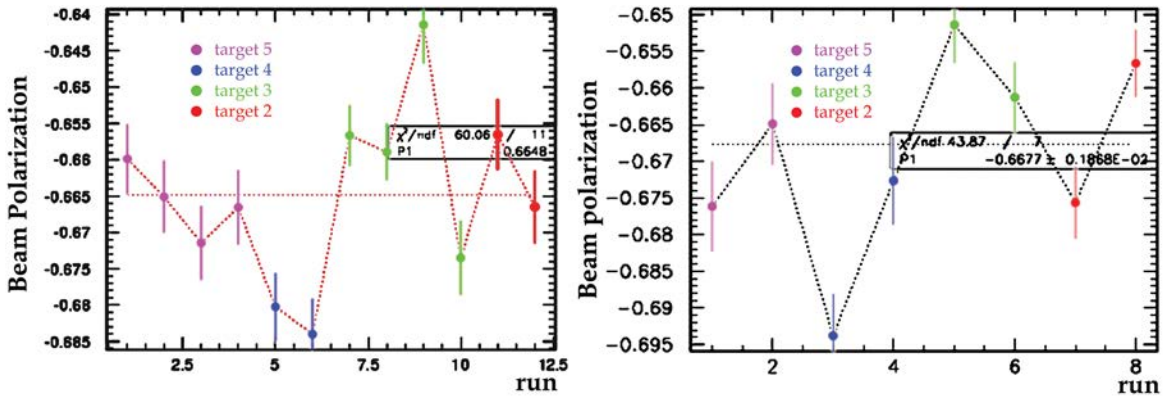

Figure E.1: The results for Møller measurements.

Bibliography

[1] H. Yukawa, Proc. Phys. Math. Soc. Japan **17**, 48 (1935).

[2] N. Kemmer, Proc. Camb. Phil. Soc. **34**, 354 (1938).

[3] C. M. G. Lattes, H. Muirhead, G. P. S. Occhialini, and C. F. Powell, Nature **159**, 694 (1947).

[4] W. K. H. Panofsky, J. N. Steinberger, and J. Steller, Phys. Rev. **78**, 802 (1950).

[5] M. Gell-Mann, Phys. Lett. **8**, 214 (1964).

[6] G. Zweig, CERN Report No. 8182/TH p. 401 (1964).

[7] M. Gell-mann and Y. Ne'eman, *The Eightfold Way* (Westview Press, 1964), ISBN 0-7382-0299-1.

[8] C. Amsler, M. Doser, M. Antonelli, D. Asner, K. Babu, H. Baer, H. Band, R. Barnett, J. Beringer, E. Bergren, et al., Phys. Lett. B **667**, 1 (2008), URL http://pdg.lbl.gov.

[9] D. Drechsel and L. Tiator, J. Phys. G **18**, 449 (1992).

[10] S. R. Amendoliac, B. Badelekc, G. Batignanic, G. A. Becke, F. Bedeschic, E. H. Bellamyg, E. Bertoluccic, D. Bettonic, H. Bilokone, G. Bolognae, et al., Phys. Lett. B **146**, 116 (1984).

[11] I. Sick, Phys. Lett. B **576**, 62 (2003).

[12] G. G. Simon, C. Schmitt, and V. H. Walther, Nucl. Phys. A **364**, 285 (1981).

[13] W. Greiner and J. Reinhardt, *Quantum Electrodynamics* (Springer, 2003), ISBN 3-540-44029-1.

[14] W. Greiner and A. Schäfer, *Quantum Chromodynamics* (Springer, 1995), ISBN 3-540-57103-5.

[15] N. M. Kroll and M. A. Ruderman, Phys. Rev. **93**, 233 (1954).

[16] G. F. Chew, M. L. Goldberger, F. E. Low, and Y. Nambu, Phys. Rev. **106**, 1345 (1957).

[17] Y. Nambu and E. Shrauner, Phys. Rev. **128**, 233 (1962).

[18] S. Fubini and G. Furlan, Ann. Phys. **48**, 322 (1968).

[19] P. de Baenst, Nucl. Phys. B **24**, 633 (1970).

[20] A. I. Vainshtein and V. I. Zakharov, Nucl. Phys. B **36**, 589 (1972).

[21] S. Scherer and J. H. Koch, Nucl. Phys. A **534**, 461 (1991).

[22] K. M. Watson, Phys. Rev. **95**, 228 (1954).

[23] E. Amaldi, B. Borgia, P. Pistilli, M. Balla, G. V. D. Giorgio, A. Giazotto, S. Serbassi, and G. Stoppini, Nuovo Cimento A **65**, 377 (1970).

[24] M. E. Peskin and D. V. Schroeder, *An Introduction to Quantum Field Theory* (Westview Press, 1995), ISBN 0-201-50397-2.

[25] A. Donnachie, G. Shaw, and G. H. Lyth, in *Electromagnetic Interactions of Hadrons vol.1*, edited by A. Donnachie and G. Shaw (Plenum Press, 1978), Nuclear Physics Monographs, chap. 5, pp. 221–256, ISBN 0-306-31052-X.

[26] S. L. Adler and F. Gillman, Phys. Rev. **152**, 1460 (1966).

[27] W. I. Weisenberger, in *Elementary Particle and Scattering theory vol.67*, edited by M. Chrétien and S. S. Schweber (Gordon and Breach Science Publishers, 1970), Brandeis University Summer Institute in Theoretical Physics 1967 Lectures, p. 245, ISBN 9780677134901.

[28] G. Furlan, N. Paver, and C. Verzegnassi, in *Photon-Hadron Interactions I* (Springer, 1972), vol. 62 of *Springer tracts in Modern Physics*, p. 118, ISBN 978-3-540-05757-4.

[29] G. Furlan, N. Paver, and C. Verzegnassi, Nuovo Cimento **20**, 295 (1974).

[30] J. Bardeen, L. N. Cooper, and J. R. Schrieffer, Phys. Rev. **108**, 1175 (1957).

[31] S. Weinberg, Physica A **96**, 327 (1979).

[32] V. Bernard, N. Kaiser, and U.-G. Meißner, Int. J. Mod. Phys. E **4**, 193 (1995).

[33] V. Bernard, N. Kaiser, and U.-G. Meißner, Z. Phys. C **70**, 483 (1996).

[34] V. Bernard, N. Kaiser, and U.-G. Meißner, Nucl. Phys. B **383**, 442 (1992).

[35] V. Bernard, N. Kaiser, and U.-G. Meißner, Phys. Rev. Lett. **74**, 3752 (1995).

[36] V. Bernard, N. Kaiser, and U.-G. Meißner, Nucl. Phys. A **607**, 379 (1996).

[37] V. Bernard, N. Kaiser, and U.-G. Meißner, Nucl. Phys. A **633**, 695 (1998).

[38] D. Drechsel, O. Hanstein, S. S. Kamalov, and L. Tiator, Nucl. Phys. A **645**, 145 (1999).

[39] S. S. Kamalov, G.-Y. Chen, S. N. Yang, D. Drechsel, and L. Tiator, Phys. Lett. B **522**, 27 (2001).

[40] F. A. Berends, A. Donnachie, and D. L. Weaver, Nucl. Phys. B **4**, 1 (1967).

[41] W. N. Cottingham and I. H. Dunbar, Z. Phys. C **2**, 41 (1979).

[42] C. T. Hung, S. N. Yang, and T.-S. H. Lee, J. Phys. G **20**, 1531 (1994).

[43] C. T. Hung, S. N. Yang, and T.-S. H. Lee, Phys. Rev. C **64**, 034309 (2001).

[44] T.-S. H. Lee and B. C. Pearce, Nucl. Phys. A **530**, 532 (1991).

[45] E. Mazzucato, P. Argan, G. Audit, A. Bloch, N. de Botton, N. d'Hose, J. L. Faure, M. L. Ghedira, C. Guerra, J. Martin, et al., Phys. Rev. Lett. **57**, 3144 (1986).

[46] R. Beck, F. Kalleicher, B. Schoch, J. Vogt, G. Koch, H. Ströher, V. Metag, J. C. McGeorge, J. D. Kellie, and S. J. Hall, Phys. Rev. Lett. **65**, 1841 (1990).

[47] A. M. Bernstein and B. R. Holstein, Comments Nucl. Part. Phys. **20**, 197 (1991).

[48] J. C. Bergstrom, Phys. Rev. C **44**, 1768 (1991).

[49] J. C. Bergstrom, J. M. Vogt, R. Igarashi, K. J. Keeter, E. L. Hallin, G. A. Retzlaff, D. M. Skopik, and E. C. Booth, Phys. Rev. C **53**, R1052 (1996).

[50] M. Fuchs, J. Ahrens, G. Anton, R. Averbeck, R. Beck, A. M. Bernstein, A. R. Gabler, F. Härter, P. D. Harty, S. Hlaváč, et al., Phys. Lett. B **368**, 20 (1996).

[51] V. Bernard, N. Kaiser, and U.-G. Meißner, Phys. Lett. B **378**, 337 (1996).

[52] A. M. Bernstein, E. Shuster, R. Beck, M. Fuchs, B. Krusche, H. Merkel, and H. Ströher, Phys. Rev. C **55**, 1509 (1997).

[53] T. P. Welch, P. H. Karen, J. H. Mitchell, B. E. Norum, H. P. Blok, H. B. van den Brink, C. W. de Jager, E. Jans, L. Lapikás, H. de Vries, et al., Phys. Rev. Lett. **69**, 2761 (1992).

[54] T. P. Welch, Ph.D. thesis, University of Virginia, Charlottesville, Virginia (1992).

[55] V. Bernard, N. Kaiser, T.-S. H. Lee, and U.-G. Meißner, Phys. Rev. Lett. **70**, 387 (1993).

[56] H. Merkel, P. Bartsch, D. Baumann, J. Bermuth, A. M. Bernstein, K. Bohinc, R. Böhm, N. Clawiter, S. Derber, M. Ding, et al., Phys. Rev. Lett. **88**, 012301 (2001).

[57] A. Schmidt, P. Achenbach, J. Ahrens, H. J. Arends, R. Beck, A. M. Bernstein, V. Hejny, M. Kotulla, B. Krusche, V. Kuhr, et al., Phys. Rev. Lett. **87**, 232501 (2001).

[58] M. O. Distler, A. M. Bernstein, K. I. Blomqvist, W. U. Boeglin, R. Böhm, R. Edelhoff, J. Friedrich, R. Geiges, M. Kahrau, M. Korn, et al., Phys. Rev. Lett. **80**, 2294 (1998).

[59] H. B. van den Brink, H. P. Blok, I. Bobeldijk, M. Bouwhuis, G. E. Dodge, M. N. Harakeh, W. H. A. Hesselink, D. G. Ireland, C. W. de Jager, E. Jans, et al., Phys. Rev. Lett. **74**, 3561 (1995).

[60] H. B. van den Brink, H. P. Blok, I. Bobeldijk, M. Bouwhuis, G. E. Dodge, C. W. de Jager, W. J. Kasdrop, T. J. Ketel, L. Lapikás, B. E. Norum, et al., Nucl. Phys. A **612**, 391 (1997).

[61] M. Weis, P. Bartsch, D. Baumann, J. Bermuth, A. M. Bernstein, K. Bohinc, R. Böhm, M. Ding, M. O. Distler, I. Ewald, et al., Eur. Phys. J. A **38**, 27 (2008).

[62] J. Alcorn et al., Nucl. Instr. and Meth. A **522**, 294 (2004).

[63] E. A. Chudakov, *JLab Hall A General Operations Manual*, The Jefferson Lab Hall A Collaboration (2008), in electronic format at, URL http://www.jlab.org/~gen/osp/osp_4.pdf.

[64] URL http://www.jlab.org/~rom/g0helicity.html.

[65] D. J. J. de Lange et al., Nucl. Instr. and Meth. A **406**, 182 (1998).

[66] W. R. Leo, *Techniques for Nuclear and Particle Physics Experiments* (Springer-Verlag, 1994), ISBN 0-387-57280-5.

[67] K. Chirapatpimol, Ph.D. thesis, University of Virginia, Charlottesville, Virginia (Expected 2011).

[68] R. Michaels, A. Camsonne, J. Segal, and D. Abbott, *Hall A 12 GeV DAQ Upgrade*, Hall A Technical Notes (2008), in electronic format at, URL http://hallaweb.jlab.org/equipment/daq/daq_12gev.pdf.

[69] E. A. J. M. Offerman, *ESPACE User's Guide*, The Jefferson Lab Hall A Collaboration (2002), in electronic format, URL http://hallaweb.jlab.org/espace/docs.html.

[70] N. Liyanage, *Optics Calibration of the Hall A High Resolution Spectrometers using the C Optimizer*, Hall A Technical Notes JLAB-TN-02-012 (2002), in electronic format, URL http://hallaweb.jlab.org/publications/Technotes/files/2002/02-012.pdf.

[71] H. Tanabe and K. Ohta, Phys. Rev. C **31**, 1876 (1985).

[72] S. N. Yang, J. Phys. G **11**, L205 (1985).